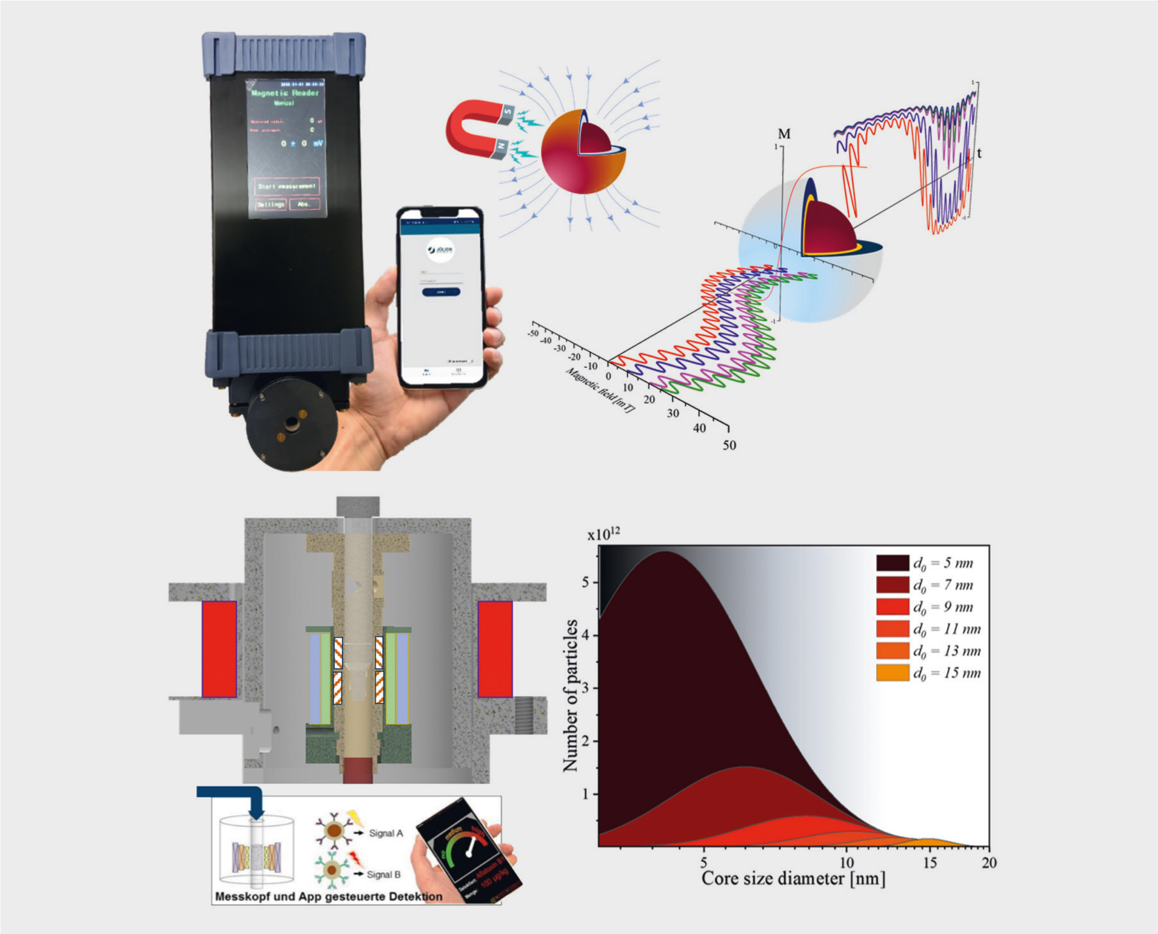

Frequency mixing magnetic detection for characterization and multiplex detection of superparamagnetic nanoparticles

Ali Mohammad Pourshahidi

Information
Band / Volume 100
ISBN 978-3-95806-727-1

Mitglied der Helmholtz-Gemeinschaft

JÜLICH
Forschungszentrum

Schriften des Forschungszentrums Jülich
Reihe Information / Information
Band / Volume 100

Forschungszentrum Jülich GmbH
Institut für Biologische Informationsprozesse (IBI)
Bioelektronik (IBI-3)

Frequency mixing magnetic detection for characterization and multiplex detection of superparamagnetic nanoparticles

Ali Mohammad Pourshahidi

Schriften des Forschungszentrums Jülich
Reihe Information / Information Band / Volume 100

ISSN 1866-1777 ISBN 978-3-95806-727-1

Bibliografische Information der Deutschen Nationalbibliothek.
Die Deutsche Nationalbibliothek verzeichnet diese Publikation in der
Deutschen Nationalbibliografie; detaillierte Bibliografische Daten
sind im Internet über http://dnb.d-nb.de abrufbar.

Herausgeber und Vertrieb: Forschungszentrum Jülich GmbH
Zentralbibliothek, Verlag
52425 Jülich
Tel.: +49 2461 61-5368
Fax: +49 2461 61-6103
zb-publikation@fz-juelich.de
www.fz-juelich.de/zb

Umschlaggestaltung: Grafische Medien, Forschungszentrum Jülich GmbH

Druck: Grafische Medien, Forschungszentrum Jülich GmbH

Copyright: Forschungszentrum Jülich 2023

Schriften des Forschungszentrums Jülich
Reihe Information / Information, Band / Volume 100

D 82 (Diss. RWTH Aachen University, 2023)

ISSN 1866-1777
ISBN 978-3-95806-727-1

Vollständig frei verfügbar über das Publikationsportal des Forschungszentrums Jülich (JuSER)
unter www.fz-juelich.de/zb/openaccess.

This is an Open Access publication distributed under the terms of the Creative Commons Attribution License 4.0,
which permits unrestricted use, distribution, and reproduction in any medium, provided the original work is properly cited.

Eidesstattliche Erklärung

Ich, Ali Mohammad Pourshahidi, erklärt hiermit, dass diese Dissertation und die darin dargelegten Inhalte die eigenen sind und selbstständig, als Ergebnis der eigenen originären Forschung, generiert wurden.

Hiermit erkläre ich an Eides statt

1. Diese Arbeit wurde vollständig oder größtenteils in der Phase als Doktorand dieser Fakultät und Universität angefertigt;

2. Sofern irgendein Bestandteil dieser Dissertation zuvor für einen akademischen Abschluss oder eine andere Qualifikation an dieser oder einer anderen Institution verwendet wurde, wurde dies klar angezeigt;

3. Wenn immer andere eigene- oder Veröffentlichungen Dritter herangezogen wurden, wurden diese klar benannt;

4. Wenn aus anderen eigenen- oder Veröffentlichungen Dritter zitiert wurde, wurde stets die Quelle hierfür angegeben. Diese Dissertation ist vollständig meine eigene Arbeit, mit der Ausnahme solcher Zitate;

5. Alle wesentlichen Quellen von Unterstützung wurden benannt;

6. Wenn immer ein Teil dieser Dissertation auf der Zusammenarbeit mit anderen basiert, wurde von mir klar gekennzeichnet, was von anderen und was von mir selbst erarbeitet wurde;

7. Teile dieser Arbeit wurden zuvor veröffentlicht, siehe: „ List of publications and contributions in conferences".

Date :

Zusammenfassung

Die Prinzipien der magnetischen Immunodetektion (MIA) gewinnen in modernen bioanalytischen Verfahren zunehmend an Bedeutung. Eine Auslesemethode, die zum Nachweis von superparamagnetischen Biomarkern eingesetzt wird, basiert auf den Prinzipien der Magnetpartikelspektroskopie. Die Frequenzmischungs-Magnetdetektion (FMMD) ist ein Messverfahren, das die Anregung magnetischer Nanopartikel (MNP) durch ein Zweifrequenz-Wechselmagnetfeld beinhaltet. Die MIA-Methoden, die FMMD als Nachweisprinzip verwenden, haben ein großes Potenzial für den Einsatz als Point-of-Care-Tests gezeigt. Andererseits wird im Bereich der Biosensorik häufig ein Multiplex-Nachweis gewünscht, d. h. der Nachweis von zwei oder mehr Analyten in einer einzigen Probe. Für Methoden, die magnetische Partikel als Marker verwenden, bedeutet dies die Fähigkeit, gleichzeitig verschiedene Arten von magnetischen Partikeln in einer Probe nachzuweisen.

In dieser Arbeit wird zunächst über die erforderliche FMMD-Instrumentierung und deren neueste Entwicklungen berichtet, einschließlich einer Strategie zur Minimierung der thermischen Verlustleistung und eines Offset-Moduls mit Permanentringmagneten, um die Auswirkungen von Temperaturschwankungen auf die Messsignale zu reduzieren. Darüber hinaus diskutieren wir die gemessene Phase des FMMD-Signals. Wir erläutern die Einflussfaktoren und ihre Auswirkungen anhand numerischer Simulationen der Signale und verifizieren die Auswirkungen durch experimentelle Messungen.

Darüber hinaus präsentieren wir eine Methode zum Nachweis und zur Extraktion des Anteils verschiedener Sorten von MNP in binären und ternären Mischungen anhand der Analyse der FMMD-Signale in Abhängigkeit vom statischen Magnetfeld. Die Mischungsproben wurden analysiert, indem die Linearkombination der reinen Referenzbestandteile bestimmt wurde, die den gemessenen Signalen der Mischungen am besten entsprach. Die Mischungsverhältnisse konnten mit einer Genauigkeit von besser als 14 % bestimmt werden.

Eine der wichtigsten Eigenschaften der MNP, die einen Einfluss auf die FMMD-Signale hat, ist ihre magnetische Kerngröße. Die FMMD-Technik kann zur Charakterisierung der MNP verwendet werden. Es hat sich jedoch gezeigt, dass die großen Partikel in der Probe den größten Teil des FMMD-Signals beitragen. Dies führt zu Mehrdeutigkeiten bei der Bestimmung der Kerngröße über die mathematischen Anpassung, da der Beitrag der kleinen Partikel von den starken Antwortsignalen der großen Partikel überdeckt werden. In dieser Arbeit wird erörtert, wie diese Mehrdeutigkeit durch die Modellierung der Signalintensität mit Hilfe des Langevin-Modells im thermodynamischen Gleichgewicht gelöst werden kann, das eine lognormale Kerngrößenverteilung enthält, die an experimentell gemessene FMMD-Daten von immobilisierten MNPs angepasst wird. Durch zusätzliche unabhängige Bestimmung der Gesamteisenmasse der Proben mittels optischer Emissionsspektrometrie mit induktiv gekoppeltem Plasma kann die Mehrdeutigkeit überwunden und die Parameter der Lognormal-Kerngrößenverteilung eindeutig bestimmt werden. Die Technik hat ein großes Potenzial, als Charakterisierungswerkzeug für die Qualitätskontrolle bei der MNP-Synthese und für Anwendungen zu dienen.

Abstract

Magnetic immunoassays (MIA) are gaining interest in modern bioanalytical methods. A readout method employed for detection of superparamagnetic biomarkers is based on the principles of magnetic particle spectroscopy. The method of Frequency Mixing Magnetic Detection (FMMD) involves the excitation of magnetic nanoparticles (MNPs) using a dual frequency alternating magnetic field. MIA methods using FMMD as detection principle have shown a high potential to be used in point-of-care testing. On the other hand, it is often desired in biosensing to perform multiplex detection, that is the measurement of two or more analytes within a single sample. For methods employing magnetic particle as markers, this means the ability to simultaneously detect different types of magnetic particle in one sample.

This thesis initially reports on the required FMMD instrumentation and its latest developments, including a duty-cycle power management strategy and a permanent ring magnet offset module to reduce the adverse effect of temperature variations on measured signals. We discuss the measured phase of the FMMD signal. We elaborate on the influencing factors and their effects using numerical simulation of the signals, and verify the effects through experimental measurements.

Moreover, we present a method for discerning the contributions of different MNPs in binary and ternary mixtures by an analysis of their static offset magnetic field-dependent FMMD signals. The mixture samples were analyzed by identifying the best linear combination of the measured reference signals of the pure constituents that best resembled the measured signals of the mixtures. The mixing ratios could be determined with an accuracy of better than 14%.

One of the important properties of MNP that has an influence on the FMMD signals is the size of their magnetic core. The FMMD technique can be used to characterize the MNP. However, it has been shown that the largest particles in the sample contribute most of the FMMD signal. This leads to ambiguities in core size determination from mathematical fitting, since the contribution of the small-sized particles is almost undetectable among the strong responses from the large ones. In this thesis, we discuss how to address this ambiguity by modelling the signal intensity using the Langevin model in thermodynamic equilibrium, which includes a lognormal core size distribution fitted to experimentally measured FMMD data of immobilized MNPs. With the help of an independent determination of the samples' total iron mass, for instance from inductively coupled plasma optical emission spectrometry, we are able to unambiguously identify the particles' lognormal core size distribution. The technique has great potential to serve as characterization tool for quality control in MNP synthesis and applications.

Table of Contents

Chapter 1

1. Introduction

Point-of-care monitoring devices came into light during the late 20th century and henceforth gained attention in both academic research and industry. They are used in the case of individual health and clinical testing [1–3], environmental monitoring [4,5], food safety [6,7], emergency response and law-enforcement testing [8,9]. For example, if natural disasters such as flooding destroy drinking water installations, technical relief organizations such as the German THW require quick and mobile testing for contamination of the drinking water sources [10]. In such disastrous events, efficient, swift and immediate action is required for proper crisis management. Hence, testing can be one of the most important decision-making tools.

Centralized lab-based testing is accurate and quantitative, but is also time-consuming, expensive and requires highly trained personnel [11] (for example, ELISA [12] and HPLC [13]). Point-of-care (POC) monitoring and testing devices are required that can be used in the field and provide fast results. This demand has increased the research interest in developing better POC devices. The detection of the analyte depends on biological and physiochemical interactions, yielding a detectable signal. Many POC platforms have been developed, allowing for qualitative and semi-quantitative detection. For example, strip-based lateral flow methods usually employ a porous matrix, and rely on an immunogenic reaction. They often use simple visualization or optical readout mechanisms to obtain qualitative results based on the presence or absence of the analyte. On the other hand, benchtop and hand-held analyzers employ more complex analytical principles of detection to provide quantitative results [14].

Another important trending aspect for POC testing is the ability of multiplex detection, which is the ability of detecting more than one biological target within a single sample. This is beneficial in both time and financial expenditure as well as reducing the needed sample amount. Different approaches have been taken, for example, lateral flow biosensors were used for multiple analyte detection through fluorescent and colorimetric methods for the detection of viruses [15], bacteria [16] and antibodies [17].

The general interest in magnetic nanoparticles (MNPs) in biomedical applications is increasing due to their unique magnetic properties and stability. They are employed for example as contrast agents in magnetic resonance imaging (MRI) [18,19] and magnetic particle imaging (MPI) [20–22]. They are also used for magnetic sorting, where they bind with specific targets, and a gradient field is utilized for separation and enrichment [23–26]. Moreover, extensive research has been conducted on the field of magnetic hyperthermia in which the MNPs are used as a therapeutic strategy for targeting cancerous cells and tumors [27–31]. In the area of biosensing, MNPs are utilized as magnetic markers [32–34]. Detection of these particles can be achieved through several different sensors and methods. For example Giant Magnetoresistance (GMR) sensors [33,35,36], Tunneling Magnetoresistance (TMR) sensors [37] and Fluxgate sensors [38]. Furthermore, techniques such as nuclear magnetic resonance (NMR) [39], susceptometry [40], relaxometry [41], and frequency mixing magnetic detection (FMMD) [42] which is the technique used in the context of this thesis, are employed for sensitive detection of MNP in samples.

The FMMD technique utilizes dual-frequency AC excitation magnetic fields to magnetically stimulate MNPs. The response of the MNPs to this dual excitation field is detected and analyzed. FMMD has proven to be very selective to superparamagnetic particles and thus it has been successfully used for the detection of a variety of biological targets. For example, recently the quantification of Aflatoxin B1 [43] and of different antibiotics in milk [44] has been shown, using a competitive magnetic immunoassay. Furthermore, by employing a noncompetitive sandwich immunoassay method, the detection of cholera toxin subunit B [45], Francisella tularensis [46], C-reactive protein [47], plant viruses [48] and influenza viruses [49,50] have been shown. FMMD-based approaches for multiplexing using frequency scanning [51] and sequential detection through spatial separation using modular 3D-printed filter columns [52] have been addressed.

In the context of this thesis, further developments on FMMD based multiplex detection approach of different MNP types is discussed. This is achieved through employing a static offset magnetic field.

Another topic discussed in this thesis is the characterization of MNPs with respect to their core size distribution. The significance of this matter is that after synthesis, proper characterization of MNPs is an essential requirement. Various techniques are utilized to characterize different aspects of the synthesized particles. The main contributing factor to the signal which is received from the MNPs comes from the crystalline magnetic core.

Determination of the core size and analysis of the morphology of the MNPs is routinely performed with transmission electron microscopy (TEM) imaging technique [53,54]. With this method, one can measure the core diameter (d_c) of a few hundred to a thousand particles to obtain a discrete core size distribution [53]. TEM requires costly instrumentation and a complex and destructive sample preparation technique while yielding only local information on the 2D projection of the particles [53,55]. In this thesis, we discuss the analysis method for the core size determination of ensembles of MNPs using FMMD measurements.

This thesis is comprised of 9 chapters. In chapter 2, brief reviews on the key topics are given. It starts with a general overview on the fundamentals of magnetism, a short review of MNPs synthesis and characterization methods, followed by the dynamic relaxation mechanism of MNPs. Moreover, the general assumption for the size distribution of MNP ensembles based on the lognormal distribution is presented. Lastly, the fundamental principles of magnetic particle spectroscopy (MPS) and FMMD technique are discussed.

In chapter 3, the instrumentation involved in FMMD technique is discussed. This includes a description of the magnetic reader device as the hand-held readout electronics, the measurement strategies and procedures. Moreover, the experimental setups involved in this thesis and further developments in the instrumentation are discussed.

To study the MNPs outside of the MIA chain, sample preparation strategies are important. In chapter 4, several sample preparation strategies and their protocols are addressed.

In chapter 5, the static offset magnetic field-dependent FMMD signal is introduced. The specific features of this signal are highlighted. Post-processing of the acquired FMMD signals is discussed, and a comparison of the different experimental setups for the measurement of MNP samples is performed. Finally, a brief analysis of FMMD signals for MNP samples in immobilized and liquid suspension states is presented, providing ground for further research.

In the FMMD technique, the phase of the mixing frequency harmonics plays an important role. This topic is addressed in chapter 6. The contributing factors to the measured phase are identified. Using both simulations and experimental verification, the impact of the phase of the excitation fields on the measured signals is elaborated.

In chapter 7, an experimental approach toward multiplex detection is presented. Here, the results of a set of binary mixtures of two different types of magnetic beads are presented. By means of determining the linear combination of the measured signals of the pure constituents that best resembles the measured signal of the mixture, the mixing ratio is extracted. The method is also applied for ternary mixtures of three different types of MNP.

Finally, the core size analysis of MNPs using FMMD technique is addressed in chapter 8. Here, an ambiguity which arises in the analysis procedure is addressed, and a method is presented for successfully resolving this issue.

Chapter 2

2. Background

2.1. Magnetism fundamentals

This chapter is based on the concepts from [56–58], otherwise mentioned specifically.

The theoretical concepts of magnetism are basically textbook material. However, to pave the road for a better understanding of the topics discussed in this thesis, a brief description of the necessary fundamental topics in magnetism is given in this section. The focus will be on the basic principles of magnetism, the declaration of the units, the symbolism which is used throughout this thesis, and a brief discussion on how materials can be classified based on their magnetic properties. Furthermore, the phenomenon known as Superparamagnetism is described.

2.1.1. Basics of magnetism

In magnetism, one deals with three important magnetic vectors, the magnetic induction **B**, the magnetic field **H** and the magnetization **M.** Adopting the SI system of units, the relationship of the three can be understood using the following equation

$$\boldsymbol{B} = \boldsymbol{\mu_0}(\boldsymbol{H} + \boldsymbol{M}) \,. \qquad \text{Eq.1}$$

Here, μ_0 denotes the permeability of the vacuum.

Considering the above relationship, we may say that a material exposed to the magnetic field **H,** acquires a magnetization **M**, which is representing the density of the total magnetic dipole moment per volume of a material. The tendency of how magnetizable a material can become under the influence of a magnetic field is known as magnetic susceptibility (χ_m), described as follows

$$\chi_m = \frac{\boldsymbol{M}}{\boldsymbol{H}}. \qquad \text{Eq.2}$$

The magnetic susceptibility is a dimensionless quantity.

The units of the respective quantities as per SI unit system are given in Table 1.

Table 1. Magnetic parameters in SI unit system.

Quantity	**SI Unit**
Magnetic moment (m or μ)	Am^2
Magnetization *M*	A/m
Magnetic field *H*	A/m
Magnetic induction, *B*	T
Magnetic susceptibility $\boldsymbol{\chi}$	Dimensionless

2.1.2. Magnetic interaction

The magnetization is originating from the interaction of the magnetic moments on atomic level. Within the materials, the magnetic moments show a dipole-dipole interaction. Typically the energy between the two dipoles is referred to as E_d and is calculated using

$$E_d = \frac{\mu_0}{4\pi r^3}\left[\boldsymbol{m}_1 \cdot \boldsymbol{m}_2 - \frac{3}{r^2}(\boldsymbol{m}_1 \cdot \boldsymbol{r})(\boldsymbol{m}_2 \cdot \boldsymbol{r})\right]. \qquad \text{Eq.3}$$

Here $\boldsymbol{m}_1$ and $\boldsymbol{m}_2$ are the two magnetic moments separated by a distance $\boldsymbol{r}$ schematically presented in Figure 1.

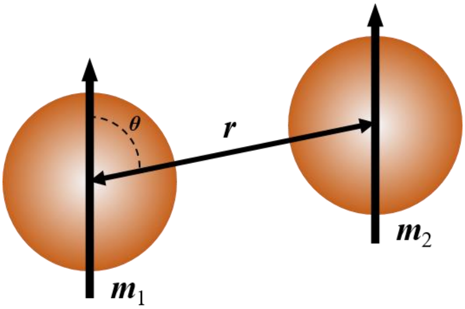

Figure 1. Dipolar interaction between two particles.

2.1.3. Magnetic materials

Materials can be classified according to their magnetic properties. In some materials, a weak magnetic interaction exists, and magnetic moments are independent, whereas in other solids, long-range magnetic order can be observed. The orientation of the magnetic moments and their magnitudes in such systems yield different properties. The main classes of magnetic systems are as follows:

- Diamagnetism
- Paramagnetism
- Ferromagnetism
- Antiferromagnetism
- Ferrimagnetism
- Superparamagnetism

In diamagnetic materials, atoms express no net magnetic moment, but a negative susceptibility is attained if exposed to the external magnetic field. In contrast, atoms of materials with paramagnetic properties have a net magnetic moment due to the presence of unpaired electrons. Since there is no magnetic interaction among the individual magnetic moments, their magnetization in absence of an external magnetic field is zero. However, when an external magnetic field is applied, a positive linear susceptibility is attained due to the slight alignment of the magnetic moments.

Ferromagnetic materials show spontaneous magnetization in absence of an external magnetic field. The atomic moments in these materials exhibit very strong interactions. The magnetic dipoles are aligned in a parallel configuration to each other in the so-called magnetic domain. Their classical magnetization behavior is illustrated in Figure 2. Upon application of an external magnetic field, the material gets magnetized until its saturation magnetization (M_s) is reached (i.e. the material cannot get further magnetized). Once the field is removed, the magnetization (M) will not return to zero but endures as a saturation remanence (M_r). On the other hand, by applying a magnetic field in opposite direction, eventually, a point called coercivity (H_c) is reached where the magnetization will be zero. Further increasing of the field will cause the magnetization to increase but in the opposite direction.

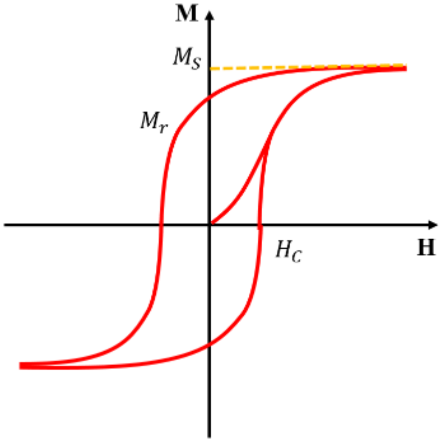

Figure 2. Hysteresis plot of ferromagnetic materials. The material is magnetized when exposed to the external magnetic field until it reaches the saturation magnetization (M_s). When the external field is removed the magnetization will remain (M_r). The magnetization is reduced when the material is subjected to an opposite external magnetic field. The magnetization reaches zero at the coercivity point (H_c). Further increase in the field results in magnetization of the material in the opposite direction.

As mentioned earlier, the exchange interaction plays a crucial role in defining the specific properties. Negative exchange interaction will result in the antiparallel alignment of the neighboring magnetic moments. This property is referred to as antiferromagnetic. A difference in the magnitude of the antiparallelly aligned moments will result in a net magnetization. This is referred to as Ferrimagnetism. Magnetite (Fe_3O_4), which is one of the prominent materials used as MNPs, is a typical ferrimagnet in its bulk form. It has an equal ratio of Fe^{2+}:Fe^{3+}. These ions are parallelly aligned on octahedral sites. However, the Fe^{3+} ions of this site are antiparallelly aligned to those on the tetrahedral side. Hence the net magnetization in this case is the consequence of the Fe^{2+} ions.

2.1.4. Superparamagnetism

Superparamagnetism (SP) is a unique form of magnetic phenomena that occurs in a specific size range of ferromagnetic or ferrimagnetic materials which is in the nanometer regime. Sufficiently small MNPs within this particular size range follow SP. In ferromagnetic materials, the domain wall formation is regulated by an interplay between the magnetostatic energy E_{ms} and domain wall formation energy E_{dw}. In a simple model under the assumption of spherical particles, the wall energy of two domain configuration is described by

$$E_{dw} = 4\pi r^2 \sqrt{A \cdot K} \qquad \text{Eq.4}$$

Where r is the radius of the spherical particle, A is referred to as the exchange constant and K is the uniaxial anisotropy constant. On the other hand, the magnetostatic energy is given as

$$E_{ms} = \frac{\mu_0 M_s^2 V}{12} = \frac{\pi \mu_0 M_s^2 r^3}{9} \qquad \text{Eq.5}$$

It is clear that E_{dw} is proportional to r^2 and E_{ms} is scaled by r^3. Depending on the material, below a critical radius r_{c}, the magnetostatic energy will be smaller than the domain wall energy and hence the single domain state would be preferred. The critical radius is determined through the comparison of two energies, described as follows

$$r_c = \frac{36\pi\sqrt{A \cdot K}}{\mu_0 M_s^2}. \qquad \text{Eq.6}$$

As an example, the material parameters reported in the literature for iron (Fe) and iron oxide (Fe_3O_4) are presented in Table 2. The calculated critical radius at which the preferred single domain state is obtained to be at 6 and 50 nm respectively. At this radius, the material is referred to as a single-domain nanoparticle.

Table 2. Fe and Fe_3O_4 material parameters.

Material	**$\mu_0 \cdot M_s$ [T]**	**A [pJ/m]**	**K [MJ/m^3]**	**r_c [nm]**
Fe	2.15	8.3	0.05	6
Fe_3O_4	0.6	12	0.013	50

The magnetic moment ($\mathbf{m}_{NP}$) of this single-domain particle is referred to as a superspin which may have large values in the order of ~1000 μ_B. In this case, the energy of the nanoparticle is described using

$$E_{NP} = -KV\left(\overline{\boldsymbol{k}} \cdot \overline{\boldsymbol{m}}_{NP}\right)^2 - \mu_0 M_s V\, \boldsymbol{H} \cdot \overline{\boldsymbol{m}}_{NP}\,. \qquad \text{Eq.7}$$

In the rotation-symmetric case depicted in Figure 3a using a prolate spheroid, the equation is modified to

$$E_{SW} = -KV sin^2\phi - \mu_0 M_s V \cos(\theta - \phi) \qquad \text{Eq.8}$$

The first term is the magneto-crystalline and shape anisotropy, and the second term describes the Zeeman energy.

An energy barrier of KV separates the energy's two minimum levels for $\phi = 0$ and 180° (π) at zero field, see Figure 3b. Upon application of a magnetic field H, the energy barrier changes. The field can be stated as a dimensionless parameter that can be used to describe the magnetization reversal in a magnetic field. The dimensionless parameter h is described as the following

$$h = \frac{\mu_0 M_s H}{2KV} \qquad \text{Eq.9}$$

When the energy barrier is larger comparing to the thermal energy (i.e. $KV >> k_B T$), the magnetic moment of the particle will not overcome the energy barrier and hence will be aligned on its easy axis, showing ferromagnetic or ferrimagnetic properties. On the other hand, if the energy barrier KV is either in the same order or smaller than the thermal energy ($KV \sim k_B T$), a statistical reversal of the moment between the two directions occurs. Hence, Superparamagnetism is defined by this behavior. In the absence of an external magnetic field, superparamagnetic nanoparticles show zero net magnetic moment. They operate similarly to paramagnets when an external magnetic field is applied, but their magnetic susceptibility is substantially higher.

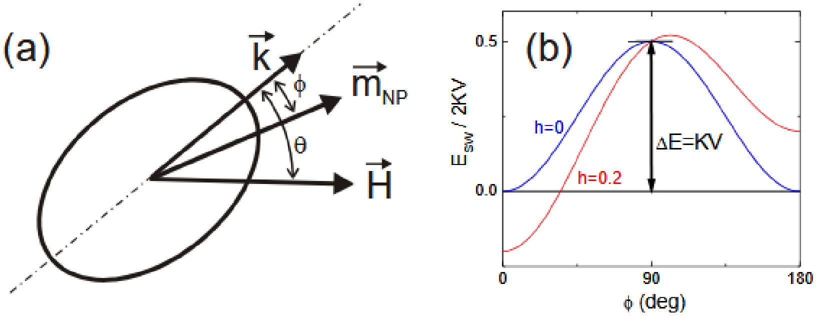

Figure 3. a) schematic of the rotation-symmetric system in prolate spheroid $\vec{k}$ represents the effective anisotropy, $\vec{m}_{np}$ the superspin and $\vec{H}$ the direction of the external field. b) The plot of $E_{SW}/2KV$ (Eq.8) as a function of the angle ϕ for dimensionless parameter h=0 and h=0.2. The energy barrier is shown as $\Delta E = KV$. This figure is taken from [59].

The magnetization behavior of the nanoparticles at the SP state is depicted in Figure 4, and is given by

$$M(H) = nm\,\mathcal{L}\left(\frac{\mu_0 Hm}{k_B T}\right). \qquad \text{Eq.10}$$

Here n is the density of the MNP and $\mathcal{L}$ is the Langevin function described as

$$\mathcal{L}(\xi) = coth\xi - \frac{1}{\xi} \qquad \text{Eq.11}$$

$$\xi = \left(\frac{\mu_0 Hm_p}{k_B T}\right) \qquad \text{Eq.12}$$

with the dimensionless parameter ξ which scales with the magnetic field. The magnetization curve shows two important features, which is being nonlinear and showing no hysteresis.

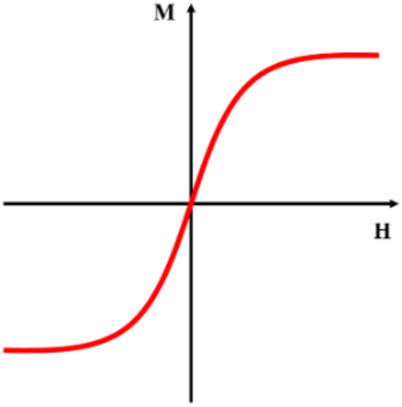

Figure 4. The nonlinear and non-hysteretic magnetization curve of superparamagnetic materials.

2.2. Magnetic nanoparticles

The most common classes of magnetic nanoparticles include metal oxide nanoparticles and metal alloy nanoparticles. As explained in the earlier section, magnetic nanoparticles present unique features which make them interesting for a variety of applications. In this section, we will look at some standard definitions with respect to magnetic nanoparticles as well as some of their applications in more detail. Moreover, different synthesis methods for producing particles and techniques for their characterization are addressed.

Magnetic nanoparticle (MNPs) is a common term that is frequently used to refer to such nanoparticles, however, in literature, they have been referred to using different nomenclatures, depending on the context, for example, superparamagnetic nanoparticles (SPNs), superparamagnetic iron oxide nanoparticles (SPIONs) for pure iron oxide particles and magnetic beads (MBs) mainly referring to multi-core particles. For simplicity and uniformity, we adopt the general acronym MNP throughout this thesis.

MNPs are typically described via a simple core-shell model [60]. Taking into account that reality is more complex, using this simple model, some key terminologies with respect to the structure of magnetic nanoparticles are established.

Figure 5 illustrates a simple core-shell model for a mono/single core particle. According to [61], the particle in this case can be separated into three regions, the crystalline magnetic core, the thin amorphous oxide layer (typically atomic layer), and the shell.

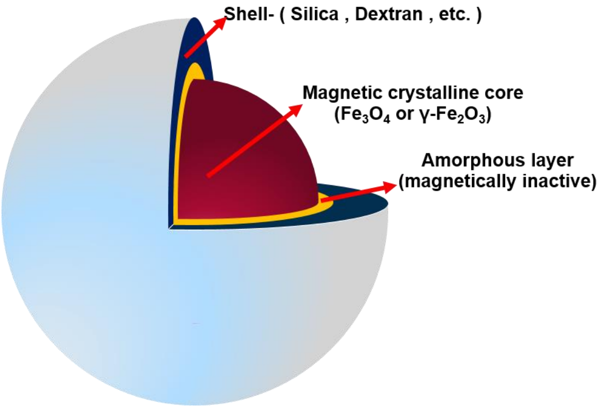

Figure 5. Core-shell model of a single core MNP.

The dimension of the particle is then characterized by the core diameter (d_c), which is ideally the diameter of the crystalline core, and the hydrodynamic diameter (d_h), which is the total diameter of the particle including the shell and further functional groups that are attached to the particle. Another common magnetic nanoparticle type is a multi-core particle, illustrated in Figure 6. As can be seen here, the particle is made up of many single cores of superparamagnetic nanoparticles, embedded in a non-magnetic matrix material.

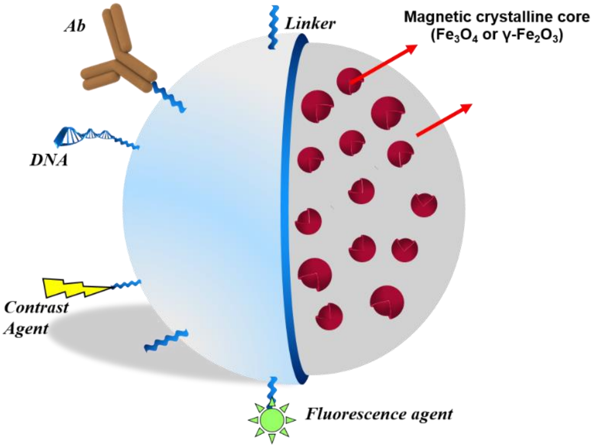

Figure 6. Graphical illustration of a multi-core particle.

The advantage of synthesizing such a particle type is that one can obtain a larger hydrodynamic diameter d_h and still retain the superparamagnetic characteristics of the MNPs. In addition, they have been shown to yield a larger magnetic response. In the introduction section, some of the applications of the MNPs were highlighted.

2.2.1. Synthesis

MNPs can be synthesized by incorporating various metallic materials such as iron, cobalt, and nickel, through different chemical methods. Our focus will be mainly on the techniques used to synthesize iron oxide nanoparticles in form of magnetite (Fe_3O_4) or maghemite (γ- Fe_2O_3). Each method has its own pros and cons. Here we will briefly discuss several common methods used to synthesize such MNPs (see also Figure 7).

Generally, synthesizing MNPs involves several processes. A typical requirement for many applications is the synthesis of MNPs with the desired size distribution. The synthesized MNPs are then coated for better stability and agglomeration prevention. Finally, the surface of the MNPs needs to be functionalized according to the needs the specific application [62]. Typical methods utilized for synthesizing MNPs are Co-precipitation, Thermal decomposition, Hydrothermal, and Polyol method.

Co-precipitation method incorporates the use of stoichiometric amounts of ferrous (Fe^{2+}) and ferric (Fe^{3+}) salts in an alkaline solution, typically ratio of 2:1 (Fe^{3+} /Fe^{2+}) [63,64]. To gain colloidal stability, water-soluble surface coating materials are needed, e.g. dextran, starch, or PEG, which also provide biocompatibility. The sequential reactions occurring through this type of synthesis start with the formation of monomers, followed by nucleation and a growth process. High-quality MNP synthesis critically depends on precise control of the reaction conditions such as pH, ionic strength, temperature, ratio, and type of the utilized salts. This method provides an easy approach for surface modification, ferrite formation, and conversion to maghemite while using cheap chemicals [65]. Typical MNP sizes that can be obtained through this method range from 5-43 nm [62,66,67]. However, it is known that this method has limited control over the size distribution and crystalline quality since the control of the size and growth highly depends on the kinetic factors [64,65,68]. On the other hand, based on further developments, some groups reported on the synthesis of magnetic nanoparticles with a narrow size distribution [66].

Thermal decomposition is a synthesis method based on the decomposition of metallic precursors such as iron-cupferronate and iron-oleate at high temperatures (T > 200°C). In this method, geometrical forms (e.g. sphere, cube, and tetrapod) and size of the particles can be tuned by controlling the reaction conditions such as heating rate, reaction time, solvent types, and surfactants used [62,64]. Thus, the process can yield homogeneous size distribution with high crystallinity grade. On the other hand, one has to consider that this method involves the use of toxic organic solvents, the reaction occurs at high temperatures, and additionally, it requires phase transfer [65]. However, using this method, MNPs in the size range of 3-50 nm can be synthesized. Reports of large-scale production of homogeneous monodispersed particles [69,70] of small diameters with a deviation of less than 10% [64,71] have since been published.

The **Hydrothermal method** involves heating and pressurizing an aqueous solution in a specific closed reaction tank to produce a high-temperature, high-pressure reaction environment [72]. This approach is utilized to synthesize MNPs through liquid-solid-solution phase transfer [62,72]. Through control of temperature and the molar ratio of the involved reagents, it is possible to tune the nanocrystal diameters in the range of 9 to 16 nm with narrow size distribution [73].

Polyol method has been used widely for the synthesis of nano- and micro-particles with defined geometries [74,75]. For the synthesis of MNPs, different polyol types (e.g. ethyle glycol (EG), diethylene glycol (DEG), and triethylene glycol (TREG)) can be used as a reducing agents. In a study, it was shown that the use of TREG can lead to the synthesis of non-agglomerated magnetite particles [76], which is very important in manufacturing MNPs. Furthermore, through this approach, the production of well-defined MNPs in the size range of 3-10 nm with narrow distribution is possible [62]. The governing factors to control and tune the particle properties involve the type of ferrous salts and the ion concentration, the reaction temperature, and the type of polyol used [77]. The advantage that this method presents is the in-situ coating of MNPs by hydrophilic polyol ligands which allows the particles to be dispersed in aqueous media and the high crystallinity of the synthesized particles due to the involvement of high temperatures [63].

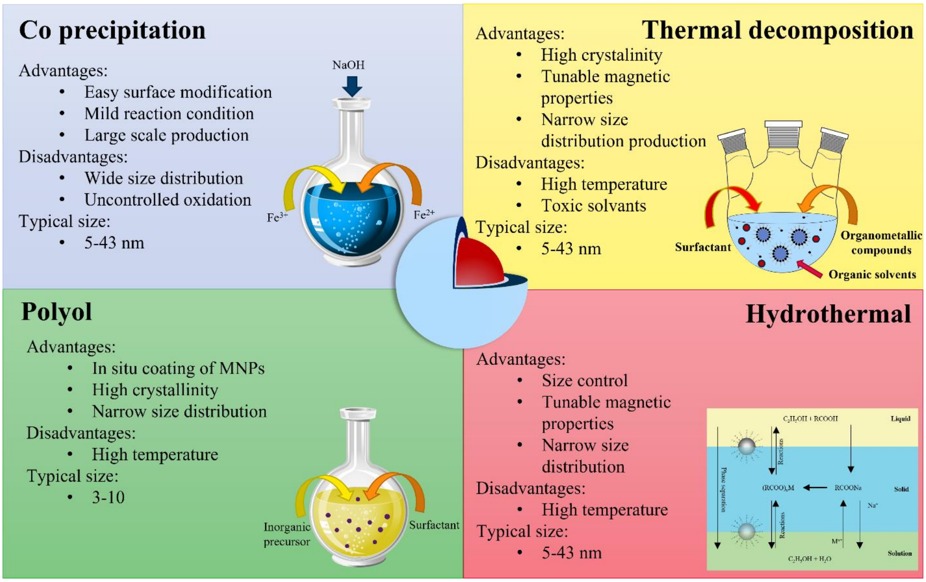
Co precipitation

Advantages:
- Easy surface modification
- Mild reaction condition
- Large scale production

Disadvantages:
- Wide size distribution
- Uncontrolled oxidation

Typical size:
- 5-43 nm

Thermal decomposition

Advantages:
- High crystalinity
- Tunable magnetic properties
- Narrow size distribution production

Disadvantages:
- High temperature
- Toxic solvants

Typical size:
- 5-43 nm

Polyol

Advantages:
- In situ coating of MNPs
- High crystallinity
- Narrow size distribution

Disadvantages:
- High temperature

Typical size:
- 3-10

Hydrothermal

Advantages:
- Size control
- Tunable magnetic properties
- Narrow size distribution

Disadvantages:
- High temperature

Typical size:
- 5-43 nm

Figure 7. Advantages and disadvantages of different MNP synthesis techniques.

2.2.2. Characterization methods

MNPs are used in a variety of applications. Nevertheless, depending on the application, different aspects of the MNP are required [78]. Thus, for assessment of the synthesized product, it is necessary to evaluate them through physio-chemical characterization methods. In this section, the different characterization methods that are typically used to evaluate the synthesized MNPs will be briefly addressed. However, the focus will be on the characterization techniques used for the determination of MNP size distribution and their magnetic properties, which are relevant to the topic of this dissertation.

Through various characterization processes, different properties of the MNPs are evaluated. These processes can be classified into a) physical characterization methods, b) chemical characterization methods and c) magnetic methods [53]. Typical physical properties which are of interest are morphology, size distribution, and structural composition. The properties obtained through chemical characterization are the chemical composition, concentration, and iron content. The magnetic methods are employed to evaluate the magnetic properties of the synthesized MNPs.

For all the applications involving MNPs, it is important to know their concentration as well as their iron content. UV-vis spectroscopy method can measure the concentration using a reference sample with known concentration. To determine the iron content in a more precise manner at lower concentrations, usually inductively coupled plasma atomic emission spectroscopy (ICP-OES) or alternatively inductively coupled plasma mass spectroscopy (ICP-MS) are used [79]. Raman spectroscopy (RS) can be employed for the chemical characterization of ferrite particles and differentiation between oxide states (i.e. hematite or magnetite) [80]. The identification of surface moieties is possible through Fourier transform-infrared spectroscopy (FT-IR) by measuring the vibrational energy of the bonds [81–83].

With respect to the characterization of the physical properties, transmission electron microscopy (TEM) is one of the common methods used to investigate the morphology, internal structure, and size of the MNPs [53]. Often cryogenic temperatures (cryo-TEM) are used to retain the structure of the aqueous media [84]. Although performing a TEM analysis is useful for a detailed investigation of the nanostructural geometry of MNPs, the method also suffers from several drawbacks. The major drawback apart from the cost is the small sample size. In order to obtain statistically relevant results, at least 300 particles should be examined. Additionally, samples need to be measured in a dry state involving a sophisticated sample preparation [54,55,85]. High-resolution TEM (HRTEM) can also be used to investigate the compositional nature of the crystal structure and of the shell [29,86]. The hydrodynamic size of the particles suspended in a solution can be determined through dynamic light scattering (DLS) which is an easy and noninvasive method. Such measurement can also be used to investigate the colloidal stability of the particles in different media [87]. X-ray diffraction (XRD) can be utilized to investigate the crystal structure, lattice spacing, and size of the crystalline core [88].

Characterization of the magnetic properties is essential to determine the response of the synthesized particles within a magnetic field. For example, the magnetization curve (M(H)) needs to be investigated to evaluate if the MNPs are superparamagnetic. For this, the magnetization (M) of the synthesized particles in presence of an external applied field (H) has to be investigated. These measurements can be performed using a vibrating sample magnetometer (VSM) [53,89] in the typical magnetic field range between -1 to +1 T. This method has the advantage that it does not require superconductors, SQUID, or cryogenic cooling. The typical sensitivity of VSM machine is in the range of 10^{-8} Am^2 [90]. For more precise measurements, SQUID magnetometers can be used [85] which allow for the measurement of magnetic moments as low as 10^{-11} Am^2 [91].

As stated earlier, one of the critical features of the MNPs which is highly important to many applications relying on the magnetic properties of the MNPs is the size of the synthesized particles. However, different attributes may be associated with the term “size” when discussing the MNPs. Thus, careful, and appropriate terminology needs to be used. For example, one can report the core size of the MNPs, but the core of the particle itself can be separated into the crystalline part of the core and the amorphous oxide layer [92]. In the case of superparamagnetic properties, only the crystalline part of the core contributes.

To summarize, the list of mentioned characterization techniques have been listed in Table 3.

Table 3. Summary of different characterization methods employed for determining different MNP properties.

Characterization Method	MNP Properties
UV-Vis spectroscopy	Iron content
ICP-OES / ICP-MS	Iron content
RS	Oxide state
TEM / HRTEM	Morphology
	Internal structure
	Core size analysis
DLS	Hydrodynamic size determination
	colloidal stability assessment
FT-IR	Surface moieties
VSM	Magnetization (M)
	Saturation magnetization (M_s)
	Remanence
	Size distribution
SQUID magnetometry	Magnetization (M)
	Saturation magnetization (M_s)
	Remanence
	Size distribution
XRD	Crystal structure
	Lattice spacing
	Size of the crystalline core

2.3. Magnetic nanoparticles’ relaxation dynamics

To understand the dynamics giving rise to the magnetic properties of the MNPs, one has to understand the involved physical phenomena. One important topic in the physics of MNPs is the dynamic relaxation process of the particles. In the case of the MNPs, the relaxation process has been described by two mechanisms, Brownian and Néel relaxations. This section aims to provide the theoretical background behind these two mechanisms. The relaxation process occurs as the decay of an excited state. In the case of the MNPs, the excited state refers to the alignment of the internal magnetic moment with respect to the external excitation field. One can understand these mechanisms by considering two cases. Initially, we consider the geometrical aspects of the MNPs, and another case is by considering the spatial state of the MNPs. The two important geometrical factors that play a role are the core size and the shell size of the MNPs. However, in reality, we have an interplay of different factors such as the intrinsic properties of the particles and the viscosity of the ambient medium. The relaxation mechanism which involves and depends on the core size of the MNPs is the Néel relaxation mechanism, which also incorporates additional intrinsic properties of the material such as the anisotropy constant. On the other hand, the mechanism which involves and depends on the hydrodynamic size of the MNPs is the Brownian relaxation mechanism, in which the viscosity of the media also plays a role. The second case to consider is the spatial state of the MNPs. If the MNPs are freely suspended in a liquid medium, the alignment to the external field may take place by physical rotation (Brownian relaxation, Figure 8) whereas if the MNPs are bound to a matrix and are unable to physically move, the process of alignment and relaxation occurs internally (Néel relaxation, Figure 9).

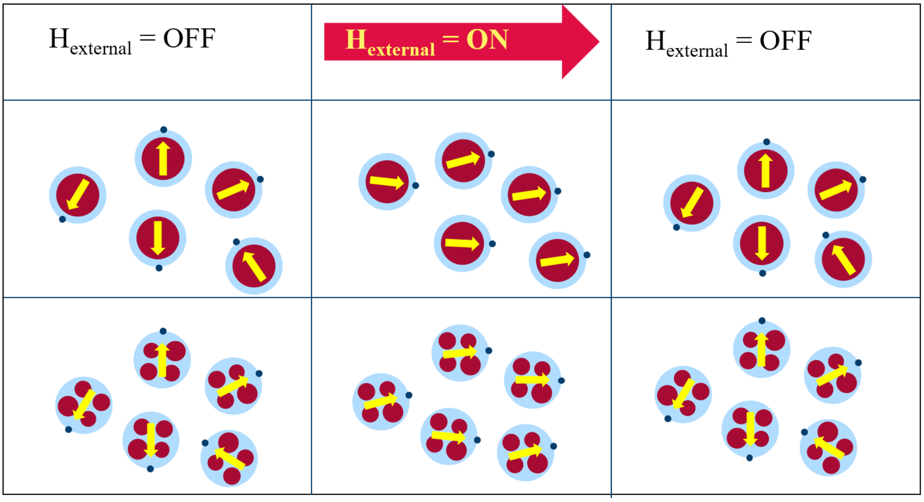

Figure 8. Conceptual illustration of the Brownian relaxation for mono core (upper row) and the multi-core (bottom row) MNPs. The leftmost column represents the initial state of the relaxed particles, the dark blue circle is placed for better visualization of the physical orientation of the particle. The middle column represents the state where the external magnetic field is presently causing the alignment of the magnetic moments by the physical rotation of the particles. The right-most column represents the relaxation mechanism where the particle moments relax by physical rotation to their initial preferred state.

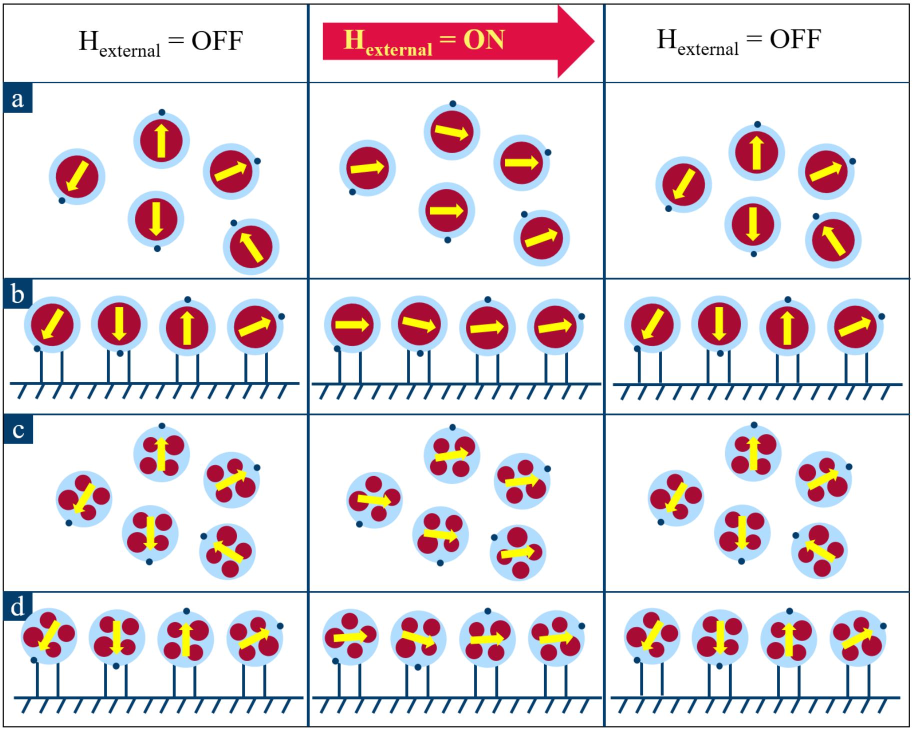

Figure 9. Conceptual illustration of the Néel relaxation mechanism for mono-core MNPs in suspension (row a) and immobilized (row b), and of multi-core MNPs in suspension (row c) and immobilized (row d). The leftmost column represents the initial state of the relaxed particles, and the dark blue circle is placed for better visualization of the physical orientation of the particle. The middle column represents the state where the external magnetic field is presently causing the alignment of the magnetic moments through internal flipping. The right-most column represents the relaxation mechanism where the particle moments flips internally to the initial preferred state.

2.3.1. Néel relaxation

The cores of MNPs are assumed to have a spherical shape with a diameter of d_c, thus the core volume V_c is given as

$$V_c = \frac{\pi d_c^3}{6} \qquad \text{Eq.13}$$

As described earlier, the Néel relaxation mechanism describes the relaxation of the internal magnetic moment of the MNP. This occurs either due to spatial fixation of the particle or if the overall size of the entity is too large. The Néel relaxation takes place during a characteristic relaxation time scale τ_N which is determined by

$$\tau_N = \frac{\sqrt{\pi}}{2} \tau_{N0} \frac{\exp(\Gamma)}{\sqrt{\Gamma}} \qquad \text{Eq.14}$$

Here, τ_{N0} describes the intrinsic relaxation time which depends on the material. The parameter Γ describes the ratio of the anisotropy energy of the internal crystalline magnetization, which separates the stable orientation of the magnetization, to the thermal energy given in form of thermal fluctuations. It can be described as

$$\Gamma = \frac{K_a V_c}{k_B T} \qquad \text{Eq.15}$$

where K_a denotes the anisotropy constant.

2.3.2. *Brownian relaxation*

The Brownian relaxation is characterized by the hydrodynamic volume V_h of the MNP and the viscosity of the surrounding media η. The Brownian relaxation time τ_B is given by

$$\tau_B = \frac{3\eta V_h}{k_B T} \qquad \text{Eq.16}$$

where V_h in the case of the spherical particles is given as

$$V_h = \frac{\pi d_h^3}{6}. \qquad \text{Eq.17}$$

2.3.3. *Effective relaxation time*

In reality, both of these mechanisms compete with each other, and the faster mechanism dominates the effective relaxation time τ_{eff} which is described as

$$\tau_{eff} = \frac{\tau_B \tau_N}{\tau_B + \tau_N} \qquad \text{Eq.18}$$

Figure 10 shows the dependence of the relaxation time vs. the particle size simulated for a mono-core particle model with a core size range from 10 to 30 nm in the case of Néel relaxation time, and a similar range for hydrodynamic diameter in the case of Brownian relaxation time. The dashed red line shows the Brownian relaxation time and the blue dashed line shows the Néel relaxation time for such a system. The effective relaxation time has been illustrated as a solid black line. The horizontal axis represents the particle size d_c in the case of τ_N, and d_h in the case of τ_B, which is matched by the color of each curve. One can see from the effective relaxation time graph that in the lower regime of hydrodynamic diameters, the Néel relaxation mechanism dominates the effective relaxation time and for the upper range of diameters, the Brownian relaxation dominates the effective relaxation time. Moreover, in the case of bound particles, the effective relaxation time is forced to follow the Néel relaxation curvature.

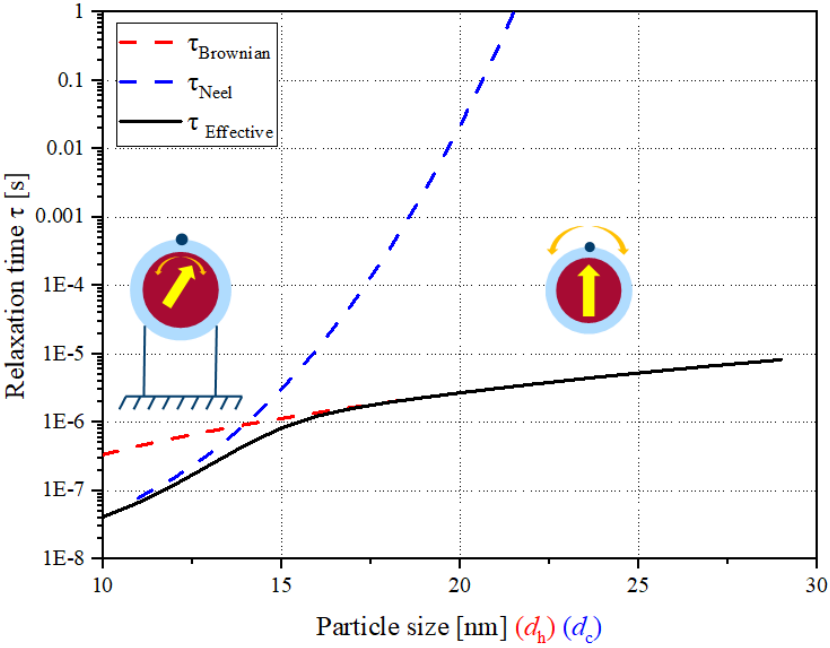

Figure 10. Illustration of Néel, Brownian and effective relaxation time dependence on the particle's core and hydrodynamic size, for MNPs at room temperature.

2.4. Size distribution of magnetic particles

In section (2.2.2) we discussed the characterization of the synthesized MNPs through various techniques. Among different characteristics, the determination of the size distribution plays an important role. We discussed that several techniques such as VSM, DLS, and TEM are employed to perform such characterizations. Furthermore, the two main size classifications of MNP, namely hydrodynamic size and core size, were discussed. In this section, we will describe the model which is used to describe the size distribution of MNPs, so that it can be used in further chapters (4 and 9), where FMMD signals are simulated based on such size distribution and later, where an inverse model is described to determine the core size distribution of the particles from FMMD measurements.

We have seen that the ensemble of non-interacting MNPs can be modeled using the Langevin function described by Eqs. (11) and (12). By assuming spherical geometry for the particles, the core size-dependent magnetic moment m_p of the particle is given by

$$m_p = \frac{M_s \pi d_c^3}{6}. \qquad \text{Eq.19}$$

Based on such assumption, the most adequate distribution that has been widely reported and used in literature is the log-normal distribution [93–96] described as

$$f_L(d_c, d_0, \sigma) = \frac{1}{\sqrt{2\pi} \cdot d_c \cdot \sigma} \cdot \exp\left(-\frac{ln^2\left(\frac{d_c}{d_0}\right)}{2\sigma^2}\right). \qquad \text{Eq.20}$$

As seen, the main variables of this function are the median of the distribution, d_0, and the dimensionless parameter σ representing the spread or width of the distribution. The relevant upper limit for the core diameter in the case of superparamagnetic MNPs (magnetite) is about 30 nm. The parameter σ, however, describes the width of the distribution. Figure 11 shows the log-normal distributions having a $d_0 = 10$ nm for σ varying from 0.05 to 0.2. The larger the sigma, the wider the distribution, thus involving many different core sizes, and smaller σ means a narrower distribution. Moreover, one can see that by increasing the parameter σ, the peak of the distribution denoted as ($d_{\max}$) shifts to lower core sizes. This is highlighted using color-coded lines on the distribution plot, and also is plotted in the inset showing the dependency of $d_{\max}$ on σ.

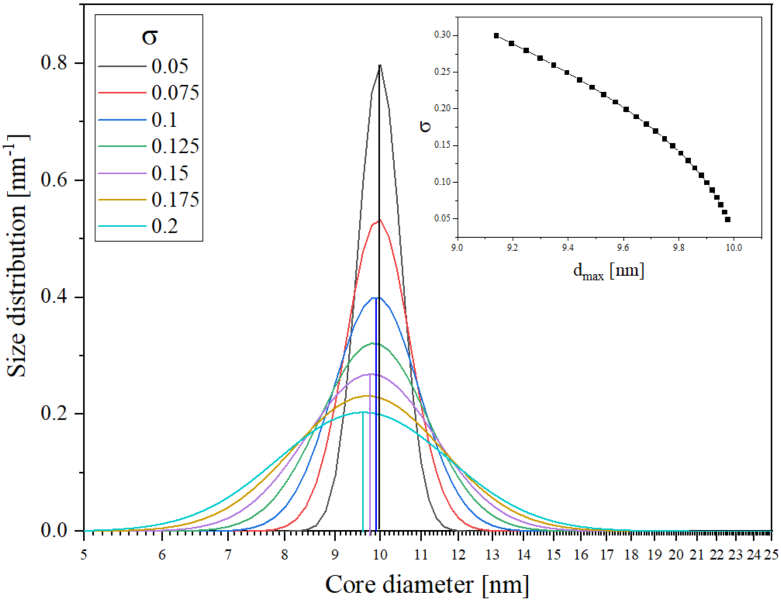

Figure 11. Lognormal distribution for variation of distribution width σ

Often in practice, the polydispersity index (PDI) is reported. Both σ and PDI are convertible to each other using the following formulas

$$PDI = \exp(\sigma^2) - 1 \qquad \text{Eq.21}$$

and

$$\sigma = \sqrt{\ln(PDI + 1)}.$$

The total magnetic moment is the sum of the moments of individual particles, each of which is given by a Langevin equation, with individual particle's saturation moments *M*$_s$. The summation of the magnetic moments of all the individual particles will yield the total magnetic moment of the ensemble

$$m_{total} = \sum_i M_{s,i} \cdot \mathcal{L}(\frac{M_{s,i}\,\pi \cdot d_c^3}{6k_BT}\ \mu_0 H). \qquad \text{Eq.22}$$

An integral over the distribution can be used to calculate the total magnetic moment of a particle ensemble with a lognormal distribution. Therefore, the following formalism is obtained:

$$m_{total} = N_p \int_0^\infty dd_c \cdot f_L\,(d_c, d_0, \sigma) \cdot m_p(d_c) \cdot \mathcal{L}\,(\frac{M_s \pi d_c^3}{6\,k_BT}\ \mu_0 H). \qquad \text{Eq.23}$$

2.5. Magnetic particle spectroscopy

The main principle of detection utilized in this dissertation is the FMMD technique. However, the path to a better understanding of this technology and its advantage is to start the discussion from the bases of magnetic particle spectroscopy (MPS). MPS, belonging to susceptometric measurement techniques, has been used widely to assess, evaluate and characterize magnetic nanoparticles for MPI [97] and also in magnetic biosensing applications [97–104]. In this section, the principle of the MPS measurement technique is addressed. In MPS the magnetic nanoparticles are exposed to an alternating magnetic field of a single frequency of a form:

$$B(t) = B_0 + B_1 \cdot \sin(2\pi \cdot f_1 t) \qquad \text{Eq.24}$$

where B_0 is the magnitude of a static magnetic offset field, and B_1 is the amplitude of the alternating excitation field with frequency f_1. The excitation field amplitude in MPS is typically ~20 mT, partially exposing the nonlinearity of the magnetization curve of the MNPs. Figure 12 adapted from [97] provides a schematic explanation of this technique. The particle response is measured using a pickup coil. Hence, the analysis of the measured signal in the frequency domain through FFT higher multiple harmonics of the fundamental frequency f_1 such as $3 \cdot f_1$, $5 \cdot f_1$, $7 \cdot f_1$, … is revealed. Note that the even harmonics will appear only under the presence of a static offset field B_0 since the magnetization curve $M(H)$ of the MNP is a point-symmetric function.

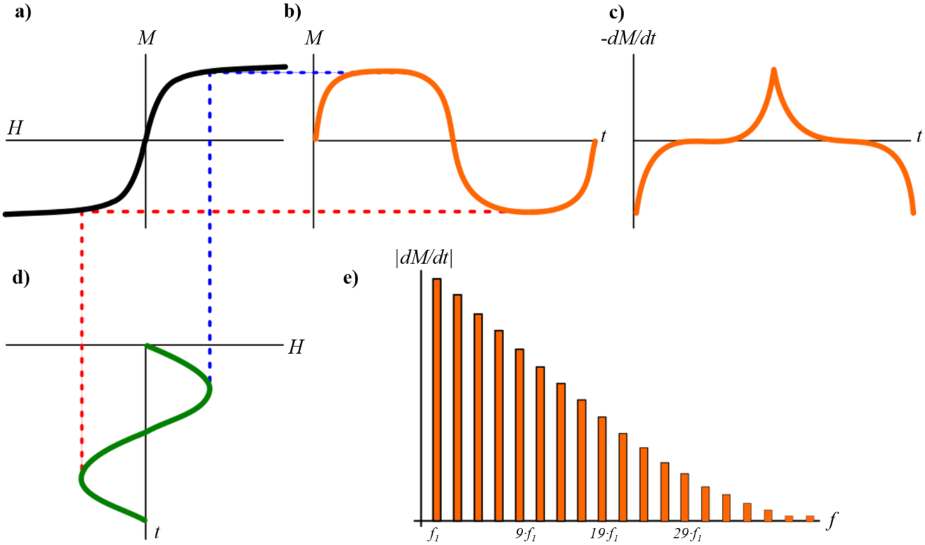

Figure 12. Graphical illustration explaining the principle of magnetic particle spectroscopy (MPS)

However, when using this technique, one has to overcome the high background fluctuation due to the mechanical and thermal instability of the coils, as well as the magnetic moment contribution from the sample matrix and/or container. The background can amount to a significant portion of the overall signal.

When MNPs are involved, the nonlinear magnetization of the superparamagnetic particles is compared to the diamagnetic or paramagnetic magnetization of the background signal.

Hence highly sensitive detection requires large fields to generate strong harmonic signals. On the other hand, according to Faraday law, a higher frequency is required for the induction of larger voltages in the detection coils. In this case, one must provide a large field strength at a high frequency which is not easily achievable simultaneously since the power consumption is proportional to the current and the frequency. This is where the FMMD technique becomes useful because it combines a high field amplitude at low frequency with a component at high frequency, thus providing ground for measuring amplitudes of mixing frequency signals and avoiding high noise at fundamental frequencies.

2.6. Frequency mixing magnetic detection

Frequency mixing magnetic detection (FMMD) relies on nonlinear magnetic susceptibility, thus it makes this method very specific for the detection of MNPs as their magnetization shows nonlinear, non-hysteretic characteristics. Furthermore, it allows for the quantification of MNPs.

The principle of FMMD can be further understood through the illustration in Figure 13. In FMMD, the sample is exposed to a dual-frequency magnetic excitation field, see Figure 13a. One of these frequencies is in the range of 60 to 150 Hz, is referred to as low-frequency (f_2), and has a magnitude (B_2) large enough to drive the magnetization of the MNPs to their nonlinear region, therefore this particular field is sometimes referred to as the driving field. The other frequency component of the excitation magnetic field ranges from 1 kHz to 100 kHz denoted as high-frequency (f_1). The high-frequency field has a magnitude (B_1) smaller than the low frequency and is used to probe the magnetization state of the particles. The applied frequency highly depends on the application and on design factors. Additionally, a static offset magnetic field (B_0) can also be applied.

The total excitation magnetic field reads

$$B(t) = B_0 + B_1 \sin(2\pi f_1 t) + B_2 \sin(2\pi f_2 t). \qquad \text{Eq.25}$$

The MNPs used as sample are resembled by their magnetization curve in Figure 13b. Upon incident excitation field, they respond with a time-varying magnetization illustrated in Figure 13c.

Let us consider the case where $B_0 = 0$, i.e. absence of the static offset magnetic field. The magnetization response of the excited MNPs is distorted and shows strong variation near zero level with flattened extremums. The Fourier transform of this distorted response yields a spectrum that exhibits the fundamental excitation frequencies f_1 and f_2 and additionally the odd multiple harmonics at $f_1, 3{\cdot}f_1, 5{\cdot}f_1 \ldots, f_2, 3{\cdot}f_2, 5{\cdot}f_2$, which are multiples of the excitation fields. Additionally, we obtain mixing frequencies which are the intermodulation products generated at the nonlinear magnetization curve at the sum and difference frequencies such as $f_1 \pm 2\cdot f_2, f_1 \pm 4\cdot f_2, f_1 \pm 6\cdot f_2, \ldots$. The even mixing terms $f_1 \pm f_2, f_1 \pm 3\cdot f_2, f_1 \pm 5\cdot f_2, \ldots$ are forbidden by symmetry. Hence, the response signal at the mixing frequencies is used to deduce information about the MNPs. An illustration of the frequency spectrum for the positive mixing harmonics up to the 4th term is schematically depicted in Figure 13d. In the case of a non-vanishing static magnetic field, the symmetry is broken, and thus both even and odd components are obtainable. This is shown in the figure using different colors.

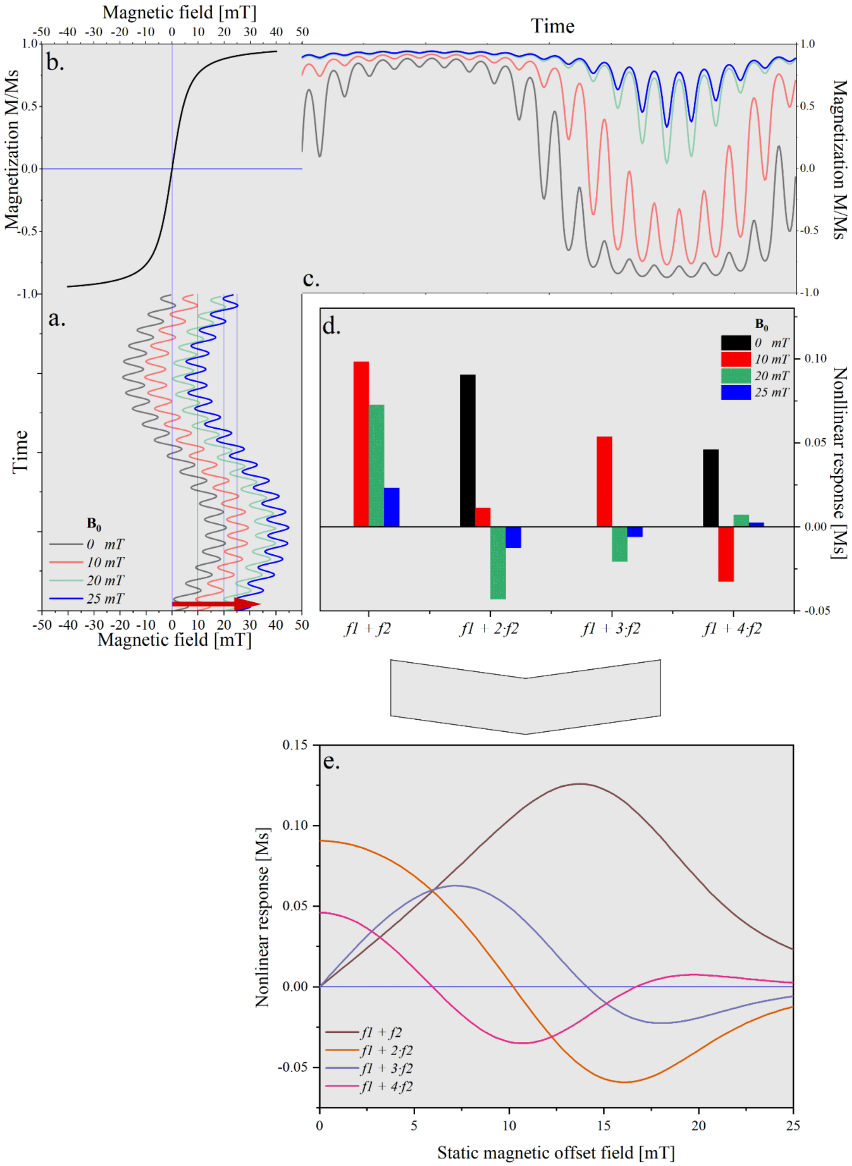

Figure 13. Two frequency magnetic excitation fields with frequencies f_1 and f_2 (a) are applied to the ensemble of superparamagnetic magnetic nanoparticles (b). The response of the particles is obtained from their nonlinear magnetization containing even and odd frequency mixing harmonics (c). In the absence of a static magnetic offset field, only odd harmonics appear. Even harmonics emerge upon introducing a static magnetic offset field B_0 (d). The nonlinear response traces show specific features upon variation of the static magnetic offset field, such as maxima, minima, and zero crossings (e).

Through variation of the static offset magnetic field, the nonlinear frequency mixing harmonic response of the magnetic nanoparticles exhibit characteristic points (maxima, minima, and zero-crossings), henceforth called features.

Traditionally, Taylor expansion is used to mathematically model these relationships [42].

One may utilize the Taylor expansion of the Langevin function Eq. 11 relating to the magnetization curve of MNPs to mathematically describe these propinquities.

The Taylor expansion of the Langevin function at a point ξ may be written as

$$\mathcal{L}(\xi) = \sum_{n=0}^{\infty} \frac{\mathcal{L}^{(n)}(\xi_0)}{n!}\,(\xi - \xi_0)^n \qquad \text{Eq.26}$$

$$\begin{aligned} \mathcal{L}(\xi) = \mathcal{L}(\xi_0) + \frac{d\,\mathcal{L}(\xi_0)}{d\xi} \cdot (\xi - \xi_0) + \frac{d^2\,\mathcal{L}(\xi_0)}{2\,d\xi^2} \cdot (\xi - \xi_0)^2 \\ + \frac{d^3\,\mathcal{L}(\xi_0)}{6\,d\xi^3} \cdot (\xi - \xi_0)^3 + \frac{d^4\,\mathcal{L}(\xi_0)}{24\,d\xi^4} \cdot (\xi - \xi_0)^4 + \cdots \end{aligned} \qquad \text{Eq.27}$$

with the derivatives

$$\frac{\mathrm{d}\,\mathcal{L}(\xi)}{\mathrm{d}\xi} = 1 - \coth^2 \xi + \frac{1}{\xi^2} \qquad \text{Eq.28}$$

$$\frac{\mathrm{d}^2\,\mathcal{L}(\xi)}{\mathrm{d}\xi^2} = -2 \coth \xi \,(\,1 - \coth^2 \xi\,) - \frac{2}{\xi^3} \qquad \text{Eq.29}$$

$$\frac{\mathrm{d}^3\,\mathcal{L}(\xi)}{\mathrm{d}\xi^3} = -2 \coth \xi \,(\,1 - \coth^2 \xi\,) + 4 \coth^2 \xi \,(\,1 - \coth^2 \xi\,) + \frac{6}{\xi^4} \qquad \text{Eq.30}$$

$$\frac{\mathrm{d}^4\,\mathcal{L}(\xi)}{\mathrm{d}\xi^4} = 16 \coth \xi \,(\,1 - \coth^2 \xi\,)^2 - 8 \coth^3 \xi \,(\,1 - \coth^2 \xi\,) - \frac{24}{\xi^5} \qquad \text{Eq.31}$$

$$\begin{aligned} \frac{\mathrm{d}^5\,\mathcal{L}(\xi)}{\mathrm{d}\xi^5} &= 16(\,1 - \coth^2 \xi\,)^3 - 88 \coth^2 \xi \,(\,1 - \coth^2 \xi\,)^2 \\ &\quad + 16 \coth^4 \xi \,(\,1 - \coth^2 \xi\,) - \frac{120}{\xi^6} \end{aligned} \qquad \text{Eq.32}$$

As per our previously declared excitation magnetic field consisting of two frequencies with ($f_1 > f_2$), the sum and difference frequency terms are then generated through the combination of the Langevin function together with the excitation field formula.

The power terms of the Taylor expansion $(\xi - \xi_0)^2$, $(\xi - \xi_0)^3$, $(\xi - \xi_0)^4$ and $(\xi - \xi_0)^5$ will contain the sum frequencies ($f_1 + f_2$), ($f_1 + 2f_2$), ($f_1 + 3f_2$) and ($f_1 + 4f_2$)

$$[B_1\, sin(2\pi f_1 t) + B_2\, sin(2\pi f_2 t)]^2 = \cdots - B_1 B_2\, cos[2\pi(f_1 + f_2)t] + \cdots \qquad \text{Eq.33}$$

$$[B_1\, sin(2\pi f_1 t) + B_2\, sin(2\pi f_2 t)]^3 = \cdots + \frac{3}{4} B_1 B_2^2\, cos[2\pi(f_1 + 2f_2)t] + \cdots \qquad \text{Eq.34}$$

$$[B_1 \sin(2\pi f_1 t) + B_2 \sin(2\pi f_2 t)]^4 = \cdots + \frac{1}{2} B_1 B_2^3 \cos[2\pi(f_1 + 3f_2)t] + \cdots \qquad \text{Eq.35}$$

$$[B_1 \sin(2\pi f_1 t) + B_2 \sin(2\pi f_2 t)]^5 = \cdots + \frac{5}{16} B_1 B_2^4 \cos[2\pi(f_1 + 4f_2)t] + \cdots \qquad \text{Eq.36}$$

This model is valid in the case of small excitation amplitudes.

Considering a single core MNP with saturation magnetic moment m_p, its nonlinear response can be modeled for sufficiently small magnetic fields. In the case of small excitation amplitudes, the frequency mixing harmonics do follow the derivatives of the Langevin function obtained through the Taylor approximation. For larger excitation fields, the nonlinear magnetic response of the MNP to the dual-frequency excitation field is

$$m_{NL} = \frac{M_s \pi d_c^3}{6} \cdot \mathcal{L}\left[\frac{M_s \pi d_c^3}{6k_B T}\,[B_0 + B_1 sin(2\pi f_1 t_i) + B_2 sin(2\pi f_2 t_i)]\right] \qquad \text{Eq.37}$$

Hence, the mixing harmonics of the FMMD signal can be demodulated through the multiplication of the m_{NL} by the respective sine or cosine of the mixing frequency. If f_1 is set to be an integer multiple of f_2, then $f_1 + n\cdot f_2$ is also a mixing frequency that is an integer multiple of f_2. As a result, the demodulation can be carried out numerically as a sum over a complete period of the low-frequency f_2, which also includes a full period of the high-frequency f_1 and a full period of the mixing frequency $f_1 + nf_2$. The calculation of the average response for even mixing components is performed using

$$\begin{aligned} m_{f1+n\cdot f2}(d_c) = {} & \frac{M_s \pi d_c^3}{6} \\ & \cdot \frac{2}{k}\sum_{i=0}^{k} cos[2\pi(f_1 + n\cdot f_2)t_i] \cdot \mathcal{L}\left[\frac{M_s \pi d_c^3}{6k_B T}\,[B_0 + B_1 sin(2\pi f_1 t_i)\right. \\ & \left. + B_2 sin(2\pi f_2 t_i)]\right] \end{aligned} \qquad \text{Eq.38}$$

with n being an odd integer number (1, 3, 5 …). Similarly, the calculation of the average response for odd mixing components is done with the equation

$$\begin{aligned} m_{f1+m\cdot f2}(d_c) = {} & \frac{M_s \pi d_c^3}{6} \\ & \cdot \frac{2}{k}\sum_{i=0}^{k} sin[2\pi(f_1 + m\cdot f_2)t_i] \cdot \mathcal{L}\left[\frac{M_s \pi d_c^3}{6k_B T}\,[B_0 + B_1 sin(2\pi f_1 t_i)\right. \\ & \left. + B_2 sin(2\pi f_2 t_i)]\right] \end{aligned} \qquad \text{Eq.39}$$

Chapter 3

3. Instrumentation

A specific readout electronics is used to experimentally realize the FMMD technique. In this realization, various modules can be used for different purposes, for example, a handheld module can be used for magnetic immunodetection as a point-of-care monitoring device, and a module enabling the application of static offset magnetic field can be used for the characterization of magnetic nanoparticles [105] and for multiplex detection of different magnetic bead types [106]. The electronic readout system for FMMD is referred to as the magnetic reader.

In this chapter, the instrumentation used throughout this work is going to be discussed. Initially, in the first section of this chapter, a general description of the magnetic reader and the measurement head will be given, which has also been reported in [107]. However, for sake of completeness and better understanding, some of the previously reported materials will be explained, and further development on the topic will be discussed when appropriate. Moreover, complete system characterization for excitation fields and phase characterization of the system and associated details will be addressed.

In the next section, a standard magnetic reader is discussed. Later in section (3.4) an additional offset magnetic field module (EMOM) will be introduced, and the issue of extensive heating of the electromagnet at higher fields will be addressed. Furthermore, the implementation of a method for overcoming this issue through pulsing the current is discussed, and further characterization and optimization of the system will be presented in detail.

In the final section of this chapter (3.5), another variant of an offset magnetic field measurement head will be discussed, incorporating a pair of permanent magnets as the source of the static offset field.

3.1. Standard magnetic reader system

The frequency mixing magnetic detection technique utilizes an induction coil-based sensor denoted as the measurement head (MH), and specific excitation and readout electronics. The system is denoted as a Magnetic reader.

3.1.1. Readout electronics

The magnetic reader instrument can be separated into two main parts, the electronic readout, and the measurement head. The methodology of the construction of the magnetic reader has been published in [42]. The readout electronics of the system is comprised of several modules, the microcontroller *AVR ATSAM3X8EA* controlling the various modules of the device, the excitation chain, measurement chain, and several auxiliary modules (i.e. Touch-Display Nextion NX4827K043, SD card storage, ESP32 wireless communication module, and barcode reader). The excitation section incorporates the two frequency synthesizers for synthesis of low and high frequency signals followed by the amplification section for generating the excitation coil currents. Furthermore, the analogue demodulation or the measurement readout circuitry consists of amplifiers and filter for signal conditioning, reference signal synthesizer and multipliers.

A general block diagram of this system is illustrated in Figure 14.

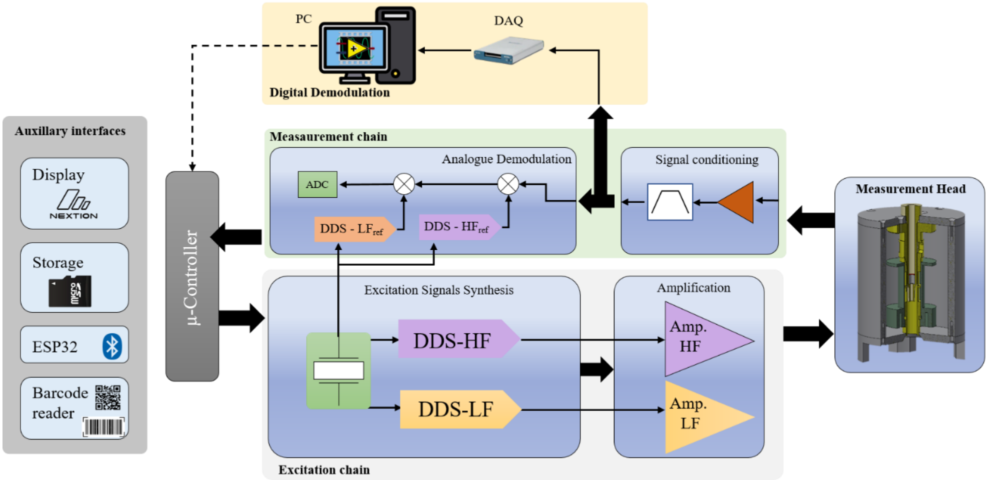

Figure 14. The general block diagram of the magnetic reader section, demodulation schemes, and the auxiliary modules.

The low and high-frequency together with the reference signals are synthesized through so-called Direct Digital Synthesis (DDS) chips of type Analog Devices AD9834 using a common 50 MHz quartz crystal ensuring the synchronicity. The DDS method is fully digitally controlled and is also called a "Numerically Controlled Oscillator" [108]. The amplitude of the generated excitation signals can be set via a 12-bit DAC of type Analog Devices AD5620 controlled by the microcontroller. The amplitudes of the generated reference signals for demodulation can remain constant, they are not adjustable.

The synthesized single-sided excitation signal generated by the DDS is then further amplified and is converted to current using Texas Instruments BUF634 power amplifiers to drive the coils. BUF634 has an output current limit of 250 mA. The output signal of the DDS is initially amplified through Texas Instruments TL072 amplifier and then is split into two non-inverted and inverted branches. With this bipolar configuration, the coil voltage and thus the current can be doubled compared to a single-sided configuration where the coil is grounded at one side. Each branch is then fed into its power amplifier and finally, at the output of the power amplifiers, we will have the excitation signals ready to be connected to the coils.

3.1.2. Measurement head

The measurement head which is the actual sensing entity of the setup is comprised of the low-frequency driving and the high-frequency excitation coils, and the differentially wound detection coil, as illustrated in Figure 15.

Depending on the application, the geometry and coil specifications may differ. In this section, the standard conventional measurement head will be discussed. In this work, we have mainly used this configuration, a conventional measurement head model which has been designed and used in earlier works [45,51,107].

The measurement head

In a conventional design of the measurement head for FMMD technology, one may use the single-entry measurement head. In this measurement head design as seen in Figure 15, the high and low-frequency excitation coils are wound on top of each other. The differentially wound detection coil is placed in the middle of the excitation coils as illustrated. It is important to know that the detection coil is wound without any discontinuity between the differential compartments. The balancing is then done by rotating the excitation coils and fine-tuning their position to ensure a centralized and balanced exposure of the detection and reference coils for their best performance. The winding numbers for the excitation and detection coils used in the experiments are listed in Table 4 (otherwise mentioned). Of the three coils, the winding of the differential detection coil plays the most crucial role. The two compartments should ideally be identical, just with opposite winding direction.

Table 4. Winding numbers and physical wire dimensions of the excitation and detection coils

Coil	Winding	Diameter [mm]
High frequency	448	0.18
Low frequency	2500	0.20
Differential detection	260 each	0.15

The coils are enclosed by a cylindrical aluminum housing of 5 mm thickness shielding the sensing units from electromagnetic fields at radio frequencies. The sample to be detected is then inserted from the top opening. The sample height should be adjusted in such a way that it resides in the detection compartment.

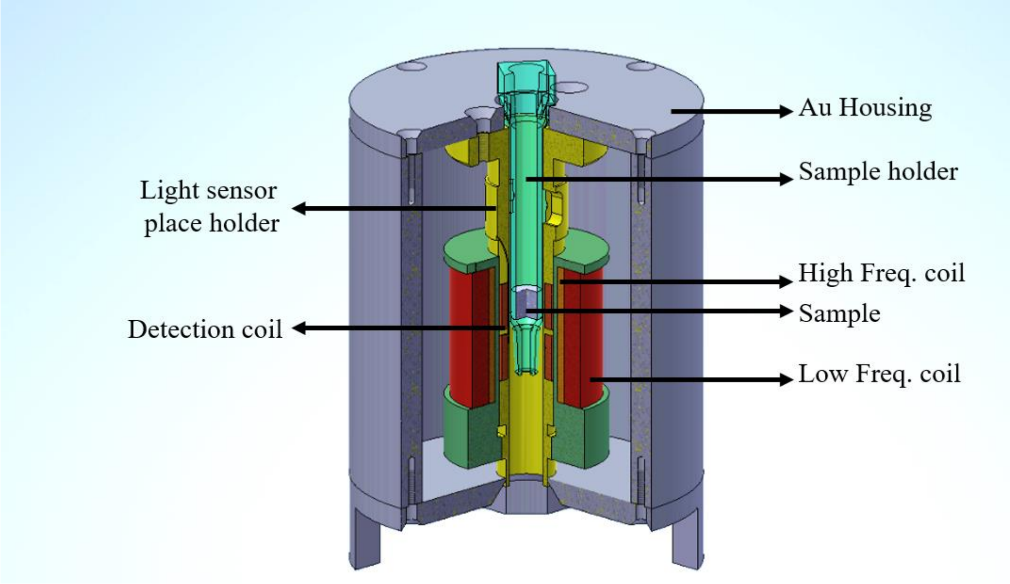

Figure 15. 3D assembly model of the measurement head

Moreover, the measurement head also houses a digital thermometer of type DS18B20 for monitoring the temperature of the head, as well as a photo-micro sensor of type EE-SX 1070 as a light barrier to enable monitoring of sample insertion and removal. Furthermore, the measurement head is equipped with a passive low pass filter with a cutoff frequency of 482 kHz to reduce the influence of high-frequency noise. The measurement head is connected to the magnetic reader via a 9-pole nonmagnetic D-sub connector.

3.1.3. Measurement chain

The detection coil signal coming from the measurement head is amplified and conditioned in a two-stage amplification circuit. The initial stage is using a low noise amplifier with a fixed gain, and in the second stage, the signal is high-pass filtered and amplified with a variable gain. Passing the amplification stage, the signal is ready to be demodulated. The demodulation can be carried out by either one of the two principles, *a) Analogue demodulation* and *b) Digital demodulation*.

The analog demodulation is based on a two-stage lock-in detection, the detection signal after pre-amplification is initially multiplied by the high-frequency reference signal extracting the intermediate frequency component, and subsequently multiplied by the reference signal at the specific mixing frequency to be demodulated. The phase of the reference signals can be set to extract the amplitude of the particles' response signal at the frequency of interest. The demodulated signal is then further processed and converted to a DC value using the specific filters and ADC (Analogue-to-digital converter). The magnetic reader benefits from a number of auxiliary interfacing modules such as a display, barcode reader, SD card, and ESP32, enhancing the user practicality and experience.

In contrast to the analog demodulation scheme, digital demodulation requires a measurement card and a PC. In the case of digital demodulation, the detection signal is digitized using a National Instrument data acquisition measurement card (NI USB DAQ) right after the pre-amplification stage. The signal is then processed using an in-house developed LabVIEW-based program on a PC. The frequency mixing harmonics of interest are extracted from the signal's FFT spectrum using a single-tone extractor software which is based on sinc() function approximation. The amplitude and the phase of each specified harmonics are extracted by that. Moreover, the complex components of the frequency mixing harmonics are also calculated (further explained in the signal processing section). The extracted information is displayed and recorded for further data processing. The communication between the PC and the microcontroller of the magnetic reader occurs through a serial communication protocol.

3.2. Characterization of the Magnetic reader

The various modules of every newly manufactured magnetic reader are required to be characterized and tested. Initially, the amplifier with variable gain in the excitation chain needs to be tuned so that the excitation signal at the highest amplification is not saturated or deformed. Moreover, the excitation magnetic fields generated using the high and low-frequency coils need to be characterized for different amplification factors. Furthermore, characterization of the phase of the excitation field also plays a major role, however, this is discussed separately in Chapter 5, since initially, the phase of the FMMD signal needs to be elaborated.

3.2.1. Characterization of the measurement head

The measurement head used in this work was characterized through the measurement of serial Ohmic resistance and inductance. The electrical parameters were measured using LC-meter HM8018 from HAMEG, the values are listed in Table 5.

Table 5. Measured parameters from the electrical characterization of the coils

Coil	Serial resistance [Ω]	Inductance [mH]
Detection	17.76	0.820
High frequency	16.24	1.53
Low frequency	91.7	58.6

3.2.2. Characterization of the excitation fields

To characterize the excitation module of the magnetic reader, the excitation signals are monitored at different test points available on the circuit board. The signals are monitored after three stages,

a) Synthesis,
b) Amplification,
c) Generated magnetic field.

The first two stages are monitored and evaluated using an oscilloscope. To monitor and evaluate the generated magnetic field, one needs to use a magnetic field measurement device (e.g.: a Hall sensor or an induction coil), and precision measurement devices such as a lock-in amplifier.

The excitation signals (LF typically at f_2 = 62.957 Hz, and HF at f_1 = 40.95 kHz) after generation and the amplified signal with the highest amplification factor are presented in appendix (1). As expressed earlier, it is of high importance that the amplified excitation current is free from any deformation. It should be purely sinusoidal. An example of a deformed signal is presented in appendix (2). Such deformation may occur for instance if one of the amplifiers is overloaded. The generated alternating magnetic field of the low frequency (B_2) coil was measured using a Hall sensor A1324 from Allegro Microsystems LLC, embedded in a 3D-printed holder that positions the sensor in the sample compartment of the measurement head.

It is important to note that due to the heating of the measurement head by the coil currents, a drift of the excitation field can be observed. Therefore, the measurements were commenced after a wait time until the temperature of the measurement head was stable at 45 °C, leading to a stable reading of the excitation field at the Hall sensor. The variation of the magnetic field through different amplification factors can be seen in Figure 16. Here the measured magnetic field of the low-frequency coil is plotted as solid red squares against the amplitude of excitation voltage. A good linear dependency is verified by obtaining an R^2 factor of 0.99 from the fit. Moreover, in the same figure, one can also see the high-frequency magnetic field variation through different amplification factors plotted as solid black squares against the excitation voltages, also showing a linear dependency with R^2 of 0.99. The mentioned Hall sensor has an intrinsic low pass filter by design, limiting its measurement range to magnetic fields below 10 kHz, therefore the high-frequency excitation field was measured through an indirect method using an induction coil, as explained in [107]. The calculation formulas are given in the appendix (3).

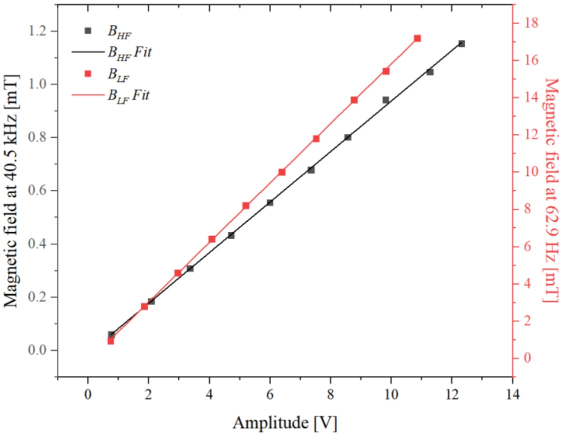

Figure 16. Variation of the measured excitation magnetic field against the applied excitation voltage. Solid red squares represent the measured magnetic field of the low-frequency coil at 62.9 Hz. The linear fit to the measured points is presented as a red solid line. The magnetic field of the high-frequency coil at 40.5 kHz is plotted as solid black squares with respective linear fit as a solid black line.

Balancing the excitation coils

The balancing procedure is performed in order to achieve as good as possible an equal and homogenous exposure of the detection and reference coil to the excitation magnetic fields. The largest induced component in the detection coil is the high-frequency component. Through this procedure, the excitation coil formers are rotated through the internal thread until the measured high-frequency excitation signal is at its minimum. For the main setup used in this thesis, a balanced detection voltage of 1.2 V was achieved at the highest amplitude of the high-frequency excitation field. The induced voltage will reduce when a lower high-frequency excitation amplitude is used.

Characterization of the demodulation chain

Initially, the gain factors of the amplifiers in the analog demodulation chain need to be adjusted so that the amplified detection signal is not deformed and lies within the limits of the input of the next stage. This is also important for digital demodulation since the pre-amplified output voltage needs to be within the input range of the measurement card.

The analysis of the influence of the reference signal phases on the demodulated signal was done by scanning the phases of the high-frequency reference and the low-frequency reference DDS while measuring a sample with a decent magnetic response for a complete range of phases, ranging from 0° to 360°, corresponding to DDS phase register values from 0 to 4095 bits. The final effective value can be calculated by subtracting the background signal measured for the absence of MNPs from the signal obtained while the sample is present. The 3D plot of the measured signals can be seen in Figure 17. In a) the red spheres represent the background signal and the blue spheres represent the signal increase when the sample is present. The offset of the amplitude is due to the ADC level. The effective signal change being the result of background subtraction is presented in

Figure 17 b. From this graph, one can extract the combination of high- and low-frequency reference phases which results in a maximum demodulated amplitude response.

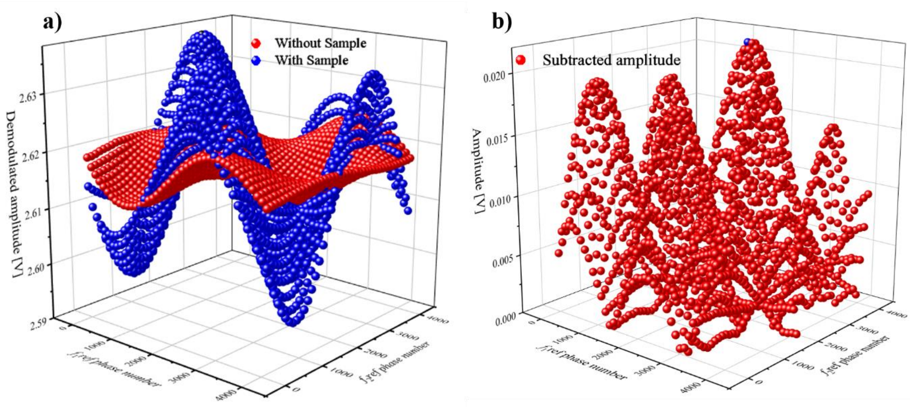

Figure 17. a) Demodulated amplitude for the signal with and without sample plotted against different combinations of the $f_{1\text{-}ref}$ and $f_{2\text{-}ref}$ phase number. b) The background subtracted amplitude shows the effective signal change due to the presence of the sample plotted against the two demodulation reference phase numbers.

3.3. Measurement procedure

As explained in the earlier sections, there are two different demodulation techniques available for obtaining the FMMD harmonics, analog, and digital demodulation. Here we will discuss the measurement procedures and the information obtained when different demodulation techniques are employed.

3.3.1. Analog demodulation

With analog demodulation, the amplitude of one single mixing harmonic at a time is measured. By default, it is set for demodulation of the mixing component ($f_1 \pm 2 \cdot f_2$), however, it is possible to demodulate any other harmonics by changing the reference demodulating frequency. This demodulation method is the method often used when portability of the magnetic reader is required, for example, in measurements of magnetic immunoassays (MIA) in the field for POC applications. Thus, either the built-in display of the magnetic reader with auxiliary modules can be used, or a wireless measurement can be conducted through the built-in ESP32 and an Android-based smart device.

The initial display-guided mode was developed and reported in [107]. To perform a measurement in this mode, an instructed measurement protocol is implemented where the user is guided throughout the measurement. As presented in Figure 18, upon commencement of the procedure, the user is asked to provide concentration calculation parameters (normally taken from the calibration curve) and sample ID. Then the user is asked to insert the sample into the measurement head. The measurement of the sample will be conducted for a pre-defined number of measurement points (typically 10 points). The user is prompted to remove the sample for measurement of the background signal. Finally, the effective signal change is reported as the mean value and the standard deviation and saved in an SD-card storage of the device.

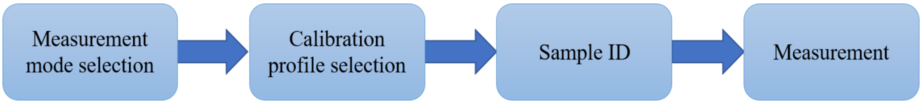

Figure 18. Measurement steps using analog demodulation

Wireless measurement mode

The MagReader control app was designed within the scope of this work in a Master thesis [109] to be used as an interface tool to the Magnetic Reader for controlling the settings and performing measurements. Using this application, the user performs a measurement using a smartphone or tablet, saves the measurements locally or creates a personal account on a storage web server (Firebase server) to upload the measured data.

The wireless measurement mode is possible with the built-in ESP32-CAM module which enables communication between the microcontroller of the magnetic reader and a smart device via Bluetooth interface. Here, direct physical interaction with the magnetic reader can be omitted. Furthermore, using a smart device for conducting the measurements brings out the advantage of cloud storage, linkage to GPS position, camera usage for reading calibration data from a QR code, optional photo documentation and easy note-taking.

The micro-controller of the Magnetic Reader is connected with the ESP32 via Serial Peripheral Interface (SPI) to enable the data exchange. The power to the board is provided via the available pin set on magnetic readers PCB providing 5 V V_{cc} and GND connection. The schematic of the connection is illustrated in the appendix (4). Serial communication is controlled by the Universal Asynchronous Receiver Transmitter (UART), an integrated function block of the micro-controller. The receive line (RX) of one module and the transmit line (TX) of the other module must be connected to enable the UART modules to communicate with each other.

The workflow of the measurement procedure is presented in Figure 19.

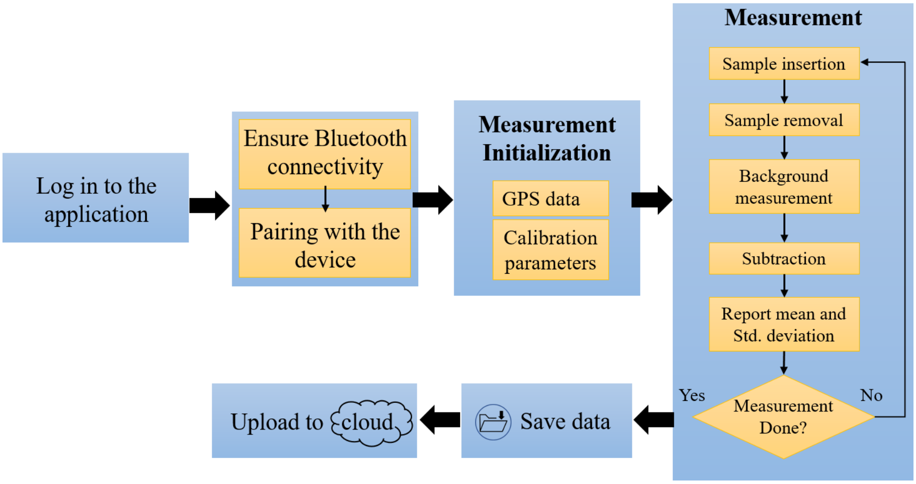

Figure 19. The measurement procedure workflow for measuring with the MagReader control app.

After successful login to the application and ensuring Bluetooth connectivity with the device, the initialization of the measurement is done by obtaining the GPS data from Google maps at the location where the test is being performed and importing the calibration parameters by scanning a QR code using the smart device’s camera. Then the measurement is commenced. The user is guided through the pop-up notifications of the application when to insert and remove the sample. Following this, the measurement results are displayed, can be saved locally, and later uploaded to cloud-based storage. Screen shots of the measurement steps are shown in Figure 20 and Figure 21.

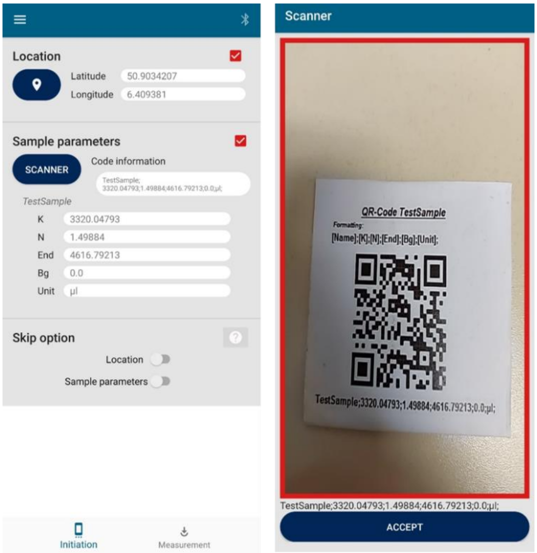

Location ☑

Latitude 50.9034207

Longitude 6.409381

Sample parameters ☑

Code information: TestSample; 3320.04793;1.49884;4616.79213;0.0;µl;

TestSample

K 3320.04793

N 1.49884

End 4616.79213

Bg 0.0

Unit µl

Skip option

Location ○

Sample parameters ○

QR-Code TestSample

Formatting:

[Name];[K];[N];[End];[Bg];[Unit];

TestSample;3320.04793;1.49884;4616.79213;0.0;µl;

TestSample;3320.04793;1.49884;4616.79213;0.0;µl;

Figure 20. Initialization window, where the GPS data and the calibration parameters of a sample can be imported.

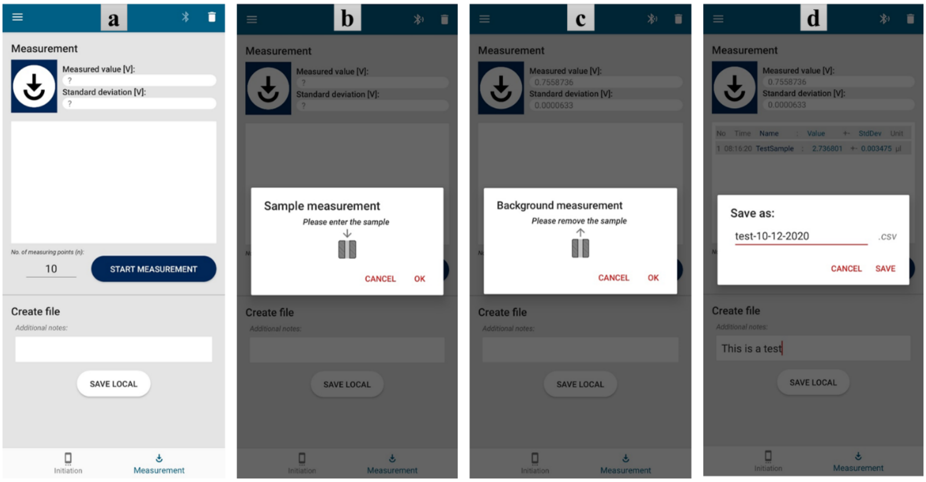

a

Measurement

Measured value [V]: ?

Standard deviation [V]: ?

No. of measuring points (n): 10

Create file

Additional notes:

b

Measurement

Measured value [V]: ?

Standard deviation [V]: ?

Sample measurement

Please enter the sample

c

Measurement

Measured value [V]: 0.7558736

Standard deviation [V]: 0.0000633

Background measurement

Please remove the sample

d

Measurement

Measured value [V]: 0.7558736

Standard deviation [V]: 0.0000633

No	Time	Name	:	Value	+-	StdDev	Unit
1	08:16:20	TestSample	:	2.736801	+-	0.003475	µl

Save as: test-10-12-2020 .csv

Create file

Additional notes: This is a test

Figure 21. Measurement of the sample. a) shows the measurement window. (b and c) The user is guided through the actions to be performed through the process. d) When the measurement is done, the values are saved locally.

3.3.2. Measurement procedure with digital demodulation

In the case of digital demodulation, as shown in Figure 14, the preamplifier detection signal is digitized using a National Instruments NI USB-6251 DAQ card which supports up to 16 channels with a resolution of 16 bits and a maximum data rate of 1 million samples per second (1 Msps). The measurement is done through LabVIEW-based measurement software on a PC.

The method is based on the description given in [107]. In this method, the LabVIEW program commences the measurement, and a fixed number of data points are recorded using the DAQ card. Subsequently, a Fast Fourier transform (FFT) is carried out for each data set. This enables the measurement of many frequency mixing harmonics simultaneously.

The schematic of the signal and trigger connections used in this work is depicted in Figure 22. The measurement signal after the pre-amplification stage is fed into the analog input of the DAQ card. The DDS chips used for generating the excitation and reference signals in the magnetic reader can be programmed to also generate a TTL signal. This signal can be used as a trigger source for measurements. As explained in [107] and in an earlier section, the choice of the selection of excitation frequencies has been in a manner where the frequency f_1 is selected to be an integer multiple of the driving frequency f_2, thus the TTL signal of the driving frequency is sufficient to trigger the measurement card to commence the measurements. In the earlier work, the TTL output of the low-frequency synthesizing DDS was used. However, in this work, we used the TTL of another DDS but with the same frequency. This is important because, in this work, an experimental investigation of the impact of excitation phases on the measured phases of the FMMD signals is performed. Hence, it is essential that an independent trigger signal with individually adjustable phase, but with the same time base and the same frequency as the driver signal is used.

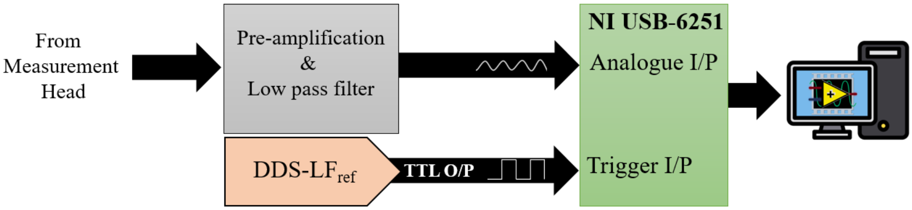

Figure 22. Connection block diagram showing the connection to the DAQ card. The detection signal after the signal conditioning stage is provided to the analog input of the DAQ card and the trigger source is obtained from the TTL signal of the built-in DDS chip.

The measurement software extracts the amplitude and phase of the desired harmonics from the FFT spectrum. The complex signal can thus be calculated. To obtain a proper measurement result, several more steps need to be taken in the post-processing of the measured signals. However, to understand why such steps are required, we need to look at the artifacts that emerge in the measurements.

Figure 23 shows the FFT spectrum of the digitized background signal (i.e. no sample is inserted) for the region of interest which is in our case approximately f_1 ± 500 Hz (40 kHz – 41.1 kHz) where the harmonics up to the 8th mixing term can be observed. The fundamental frequency exhibiting the largest amplitude can be seen at 40.5 kHz. Spurious harmonics at intervals of the low frequency (f_2) can also be seen in the figure. The appearance of these mixing terms is mainly due to the total harmonic distortion of the synthesized excitation signals using the DDS chip.

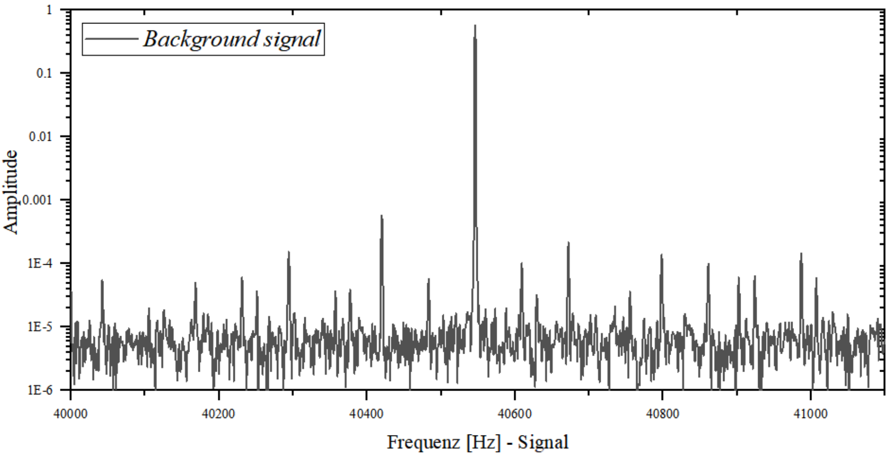

Figure 23. FFT spectrum of the measurement region between 40 to 41.1 kHz

Figure 24 shows the frequency spectrum of the low-frequency excitation signal from 60 Hz to 41.1 kHz obtained after synthesis. In this case, the fundamental low frequency is observable at 63 Hz. Additionally, the harmonics generated as multiples of the fundamental frequency can also be observed. The total harmonic distortion (THD) was calculated according to [110] using

$$THD = \frac{\sqrt{V_2^2 + V_3^2 + V_4^2 + V_5^2 + V_6^2}}{V_1} \qquad \text{Eq.40}$$

where V_1 is the rms amplitude of the fundamental frequency and V_2 to V_6 are the rms amplitudes of the second to sixth harmonics. The THD calculation yields a distortion of 0.04%, however, despite that, one can see a continuous reoccurrence of the integer multiple harmonics of the fundamental frequency even in the relatively high-frequency range where the FMMD measurement occurs.

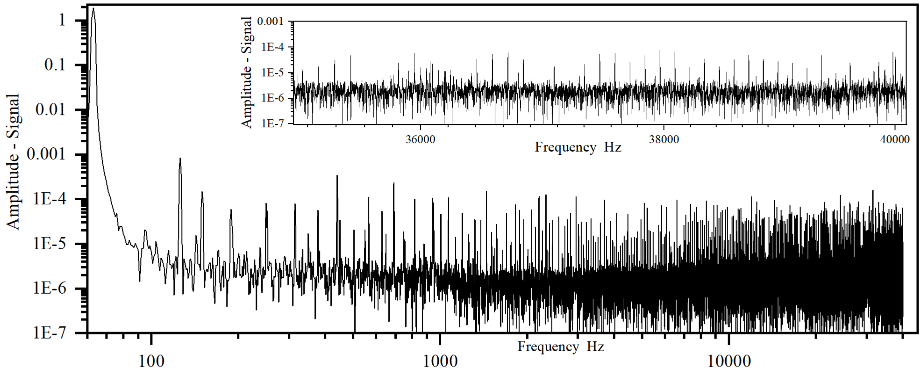

Figure 24. Frequency spectrum of the synthesized low-frequency excitation signal after synthesis

Investigation of signals from 3 situations: a) synthesized f_2 signal, b) detection coil signal with induced f_2 signal only, and c) detection coil signal with both f_1 and f_2 induced is presented in Figure 25.

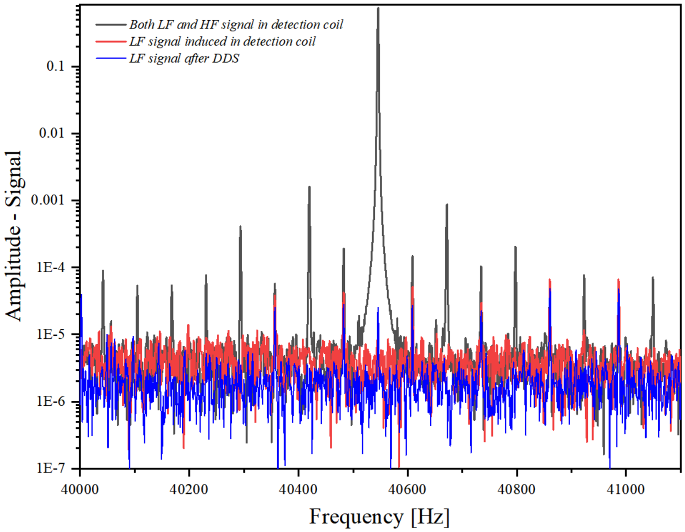

Figure 25. Overlap of the frequency spectrum of the measurement region between 40 to 41.1 kHz for the synthesized f_2 signal depicted in blue, the detection coil signal with induced f_2 signal only depicted in red, and the detection coil signal with both f_1 and f_2 depicted in black.

In this figure, the f_2 signal recorded from the test point after the synthesis stage is depicted by a blue line. We can see the peaks occurring at integer multiples of f_2. The induced low-frequency B_2 signal in the detection coil when the high-frequency B_1 field is off is depicted as red solid line. In this situation, we also observe the reoccurrence of the f_2 integer multiple peaks. The situation gets more dramatic when both B_1 and B_2 fields are turned on, plotted as solid black line. In addition to the expected large fundamental f_1 peak, one can clearly observe the intensified harmonics at both sides of that peak. Here the question arises of how their amplitudes vary in time. If the amplitudes of the peaks present a low time variance, they can be treated as additive background signal and can easily be subtracted from the measurement. However, the situation will get more complex if the peaks exhibit a large variation in time.

The peaks appearing without a sample in the measurement head are referred to as the background signal. To assess the variability of these background signals, a long-time measurement was conducted by recording the background signals at mixing frequencies ($f_1 \pm n \cdot f_2$), with ($n \in \mathbf{Z}$) for long measurement times of 5 hours, and even 24 hours. The results of the time traces for the background signal are presented in Figure 26. Firstly, the amplitude asymmetry between the positive and negative harmonics is clearly notable. Moreover, we observe an initial variation of ~200 µV for both $f_1 \pm 2 \cdot f_2$ signals, and in the case of $f_1 \pm 4 \cdot f_2$, an initial variation of ~30µV for the first 50 min is observed. The signal is then stabilizing and henceforth remains stable. The initial variation reduces for higher harmonics. Moreover, the temperature development inside the measurement head is depicted by the red curve, showing the progression of temperature, starting from 34 °C and stabilizing around 43.5 °C. The major contribution to the initial variation is the temperature drift. Since assessment of the temperature behavior is out of the scope of this work, details will not be discussed. However, a clear correlation between temperature and measurement signal is observable. Thus, it is of utmost importance that measurements be conducted only when the temperature is stabilized. Analyzing the variation after stabilization of the measurement signals of 8 different measurement harmonics yields a variation of ~5.14 ±0.9 µV. The mean and standard deviation of each background signal are listed in Table 6 obtained from the region after a stable temperature has been reached, where the deviation is approximately < ± 1°C.

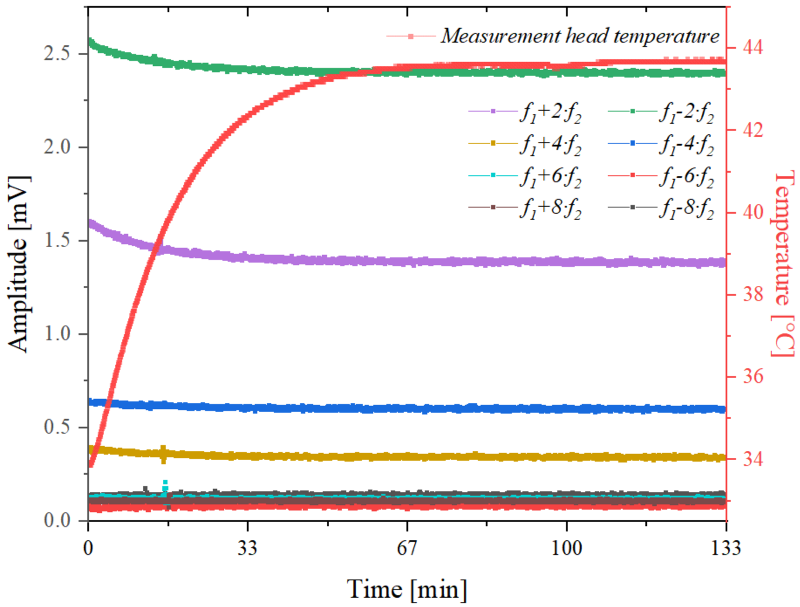

Figure 26. Time trace measurement of the background signals for 8 odd mixing frequency harmonics ($f_1 - 8 \cdot f_2$ to $f_1 + 8 \cdot f_2$) and the temperature development inside the measurement head plotted in red.

The analysis results suggest that we can treat the peaks as added background signals and calculate the final effective signal changes due to the presence of the MNPs through subtraction.

Table 6. Mean amplitude and standard deviation of the background signals of 8 odd mixing frequency signals.

Mixing harmonic	**Amplitude mean** [mV]	**Standard deviation** [mV]
$f_1+2 \cdot f_2$	1.39	0.006
$f_1 - 2 \cdot f_2$	2.4	0.005
$f_1+4 \cdot f_2$	0.34	0.004
$f_1 - 4 \cdot f_2$	0.59	0.005
$f_1+6 \cdot f_2$	0.11	0.004
$f_1 - 6 \cdot f_2$	0.08	0.005
$f_1+8 \cdot f_2$	0.10	0.003
$f_1 - 8 \cdot f_2$	0.13	0.005

When the sample is inserted inside the measurement head, as per theory the mixing frequency harmonics are generated due to the nonlinear magnetization of the MNPs. The frequency spectra of the measurement region for the background signal and for the signal with sample (Synomag D 70 nm) are presented in Figure 27a. The spectrum of the signal with sample is shown in red and the background in black. The asymmetry is not easily visible at the logarithmic scale, but by looking at the linear scale given in the smaller graph on the top right corner of Figure 27a, the asymmetry is clearly notable. Additionally, if the subtraction of the background signal is done using the amplitude information only as presented in Figure 27b, it is observed that the issue of asymmetry still prevails.

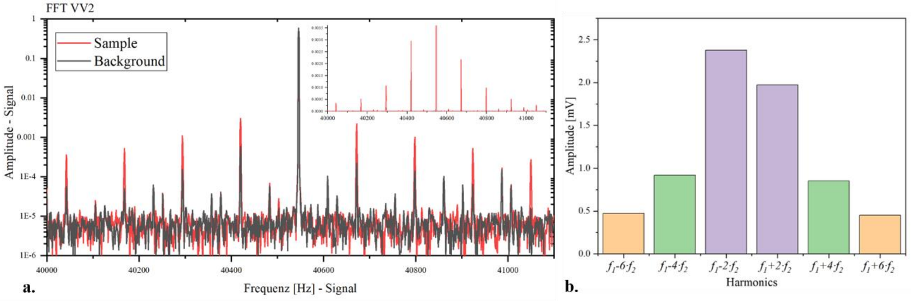

Figure 27. a) Frequency spectrum of the background signal in black, and signal with sample in red, b) amplitude of the odd mixing harmonics after background subtraction.

For further analysis, and to explain the background subtraction method used, we look at the measured signals in the complex domain. Figure 28a shows the complex plane plot of the measurement signal $f_1 \pm 2 \cdot f_2$ for background and sample measurements. The background signal is depicted as black solid squares, and the measurement signal with the sample is indicated using a solid red circle. The background value of the $f_1 + 2 \cdot f_2$ is in the first quadrant and the background value for the $f_1 - 2 \cdot f_2$ is located on the negative imaginary axis between the second and third quadrants. The black vector shows the direction of the signal progression. We can see that when the sample is inserted, the measurement value for $f_1 + 2 \cdot f_2$ is conducted in the third quadrant and its counterpart in the second. The occurrence of measurement points in different quadrants yields the final calculation error when only amplitudes are used. However, when the subtraction is done initially in the complex domain, recalculation of the amplitudes leads to much closer symmetrical values of frequency mixing pairs $f_1 \pm 2 \cdot f_2$, see Figure 28b. The subtracted measurement points are depicted as solid blue triangles and shown as blue vectors from the origin of the plot.

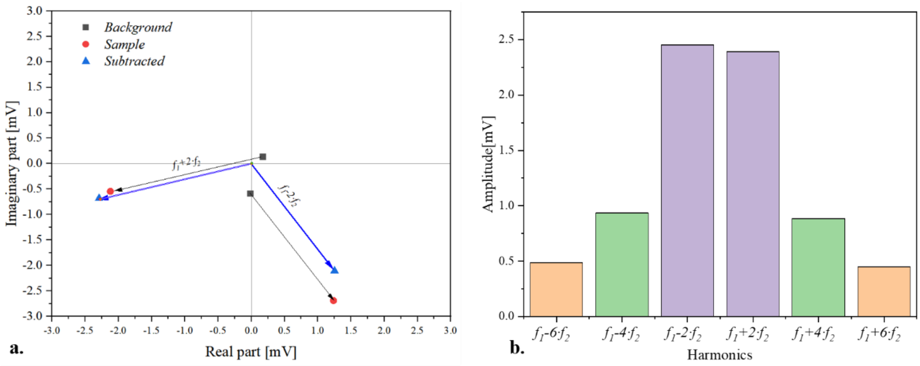

Figure 28. a) Complex plane plot of the measured background signal (black square) and signal with sample (red circle) for mixing frequency harmonic $f_1 \pm 2{\cdot}f_2$, the subtraction of background signal is done in the complex domain and the result is plotted as blue triangle. b) bar chart representation of the amplitude of the odd mixing frequency signals after subtraction in complex domain.

Subtraction of the background from the sample measurements for each measured harmonic was calculated through simple subtraction

$$Real_{Subtracted} = Real_{Sample} - Real_{Background} \qquad \text{Eq.41}$$

$$Imaginary_{Subtracted} = Imaginary_{Sample} - Imaginary_{Background} \qquad \text{Eq.42}$$

The re-calculation of amplitudes yields a very close value with less than 10% deviation in total. Details of the deviations are given in Table 7. It can also be noted that for higher harmonics, the deviation increases which can be contributed to the smaller amplitudes and lower SNR.

Table 7. Deviations of the symmetrical odd frequency mixing harmonics after subtraction in the complex domain

Mixing harmonics	Deviation %
$f_1 \pm 2{\cdot}f_2$	3
$f_1 \pm 4{\cdot}f_2$	6
$f_1 \pm 6{\cdot}f_2$	7

The presented results emphasize the importance of considering the phase information when processing the measured data. The topic of phases in the FMMD technology can be subdivided into two main classes: a) The phase of the excitation signals and their impact on the measurement signal and b) the phase of the demodulation chain. For investigation and explanation of this subject, measurements and simulations of the offset-dependent signals are required. However, further prior information on instrumentation is required to provide a better understanding. Thus, this topic is discussed in chapter 5.

3.4. Offset electromagnet module

3.4.1. General description

The appearance of the odd mixing frequencies as mentioned earlier in (2.6) can only occur in conjunction with a non-vanishing static magnetic offset field. A measurement setup with the capability of providing a static offset magnetic field is used to obtain the static offset field-dependent FMMD signals. This is done through a device developed and reported in [106,107]. In this section, we will briefly introduce the setup and elaborate on the further developments in the context of this work. The setup is comprised of the Magnetic reader (see section 3.1) and a measurement head which is enclosed with an electromagnet unit driven by a programmable current source HP 6032 from Hewlett Packard to generate the static offset magnetic field. The simplified block diagram of the experimental setup together with a cross-sectional sketch of the measurement head is shown in Figure 29.

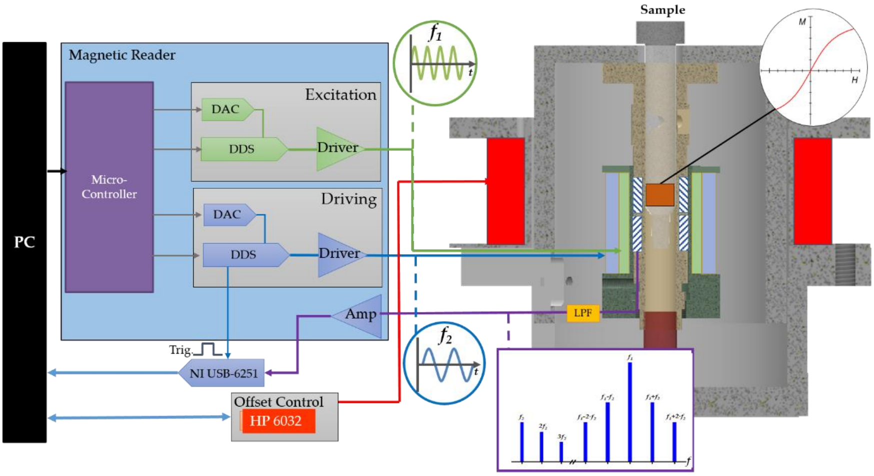

Figure 29. Schematic overview of the magnetic frequency mixing detection setup with static offset magnetic field. A PC was used for controlling the magnetic reader and measurement. The magnetic reader consisted of a microcontroller, two direct digital synthesis (DDS) chips, and a digital-to-analog convertor (DAC), filters, and drivers supplying the excitation and driver coils. A sectional image of the measurement head is shown with excitation (green), driving coil (blue), and static offset coil (red). The static offset coil was controlled by an HP 6032 power supply. The output of the detection coil, which contained the information about the mixing frequencies was connected via a low pass filter (LPF) to a preamplifier (Amp), which was built into the reader, and then to a National Instrument measurement card USB-6251 for a triggered measurement.

The offset-generating electromagnet is wound around an aluminum bobbin with an inner diameter of 64 mm and a height of 25 mm. The coil is made from 320 windings in 14 layers using copper wire with a nominal diameter of 1 mm, resulting in a resistance of 1.8 Ω. Characterization of the coil yields a coil factor of 4.8 µT/mA with very good linearity.

In Ref. [107], a water-cooling strategy was used to make sure that the coil operated safely without overheating. A silicone tube with an outer diameter of 5 mm and wall thickness of 1 mm was wound around the coil and connected to a water cooling set “Alphacool NexXxoS Cool Answer 240 LT/ST” from Alphacool International GmbH (Braunschweig, Germany). The temperatures of the coil body, tubing and reservoir are monitored constantly using digital temperature sensors of type DS18B20 from Maxim Integrated, San Jose, California. The setup is equipped with an automated sample insertion and removal mechanism which brings the sample into the optimal measurement position and removes it for background measurement. The mechanism involves an in-house fabricated rod made of Polyvinyl chloride (PVC) coupled to a servo motor controlled by an Arduino board. The rod is lowered for sample insertion and is raised to lift the sample for removal. The picture of this setup is presented in Figure 30.

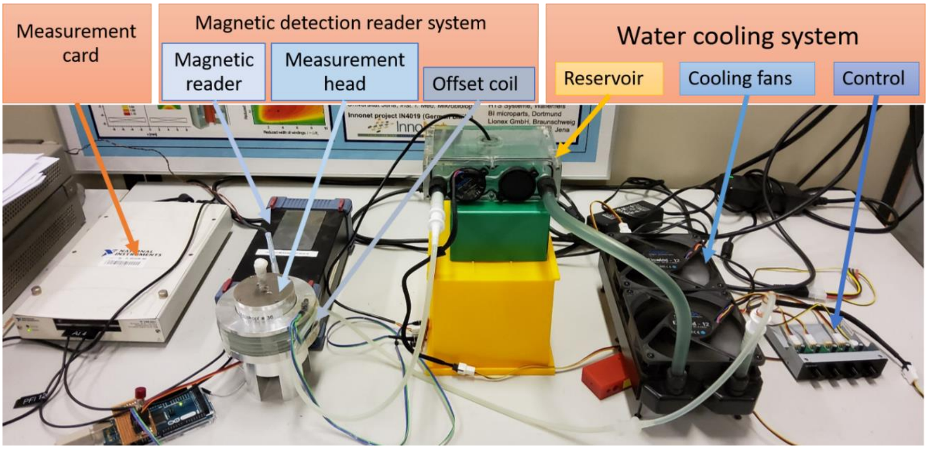

Figure 30. Photograph of the electromagnet based offset module setup. The offset coil is placed around the standard FMMD measurement head, and water cooling is done using a commercial PC water cooling system. Different components of the setup are labeled accordingly.

3.4.2. Electromagnet thermal limitation

One major drawback of this system is that while increasing the static offset field, the temperature is also increased due to the resistive heating of the coil. It is well known that increased temperatures will change the measurement signals [111]. In the initial measurement protocol, it was always accounted for temperature stabilization. Hence the sample was measured for a duration long enough so that a stable signal was obtained. Of course, this procedure leads to long measurement times. The time progression of the measurement head temperature and offset coil body temperature is depicted in Figure 31. The increase of static offset magnetic field is given in blue and the corresponding temperature development is shown in black and red. The static offset magnetic field was varied from 0 to 24 mT in 51 steps. The temperature of the coil was initially ~ 27 °C, and the measurement head temperature warmed up to ~ 43 °C. Based on the measurements, we achieve an offset magnetic field of ~25 mT at the expense of increasing the measurement head's temperature up to 75 °C.

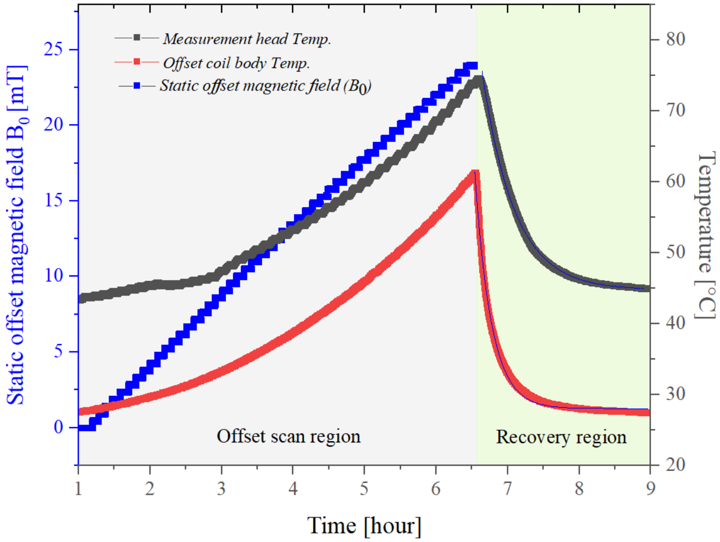

Figure 31. Time trace of the applied static offset magnetic field (blue) and the progression of the temperature in the measurement head (black) and offset coil body (red)

Furthermore, it is important to note that when the measurement is finished, a recovery time is required until the system is back to its initial temperature before the next measurement can be started. The recovery time for the temperatures was estimated by fitting an exponential decay curve to the recovery region of the temperature graph, yielding a full recovery time of ~75 min until the measurement head temperature is stabilized to its initial value. Considering the offset scan time and recovery time, the total measurement time for an offset field scan is at least 7.5 hours.

In the scope of this work, a new strategy was implemented to reduce the temperature effects caused by the heating of the electromagnet. This is done through the so-called power management, where the supply to the offset coil is delivered in a pulsed fashion with a specific duty cycle. Figure 32 shows a schematic example of how this method works while measuring the sample. In the upper row, the sample position is depicted where initially the sample is out and the background signal is being measured. The lower row shows the status of the static offset magnetic field B_0. It is set in the management program so that the same number of steps is used to apply the field for measuring the background and sample. Once the background measurement is done, the sample is inserted. The next magnetic field is applied when the sample is out, and the new background is being measured.

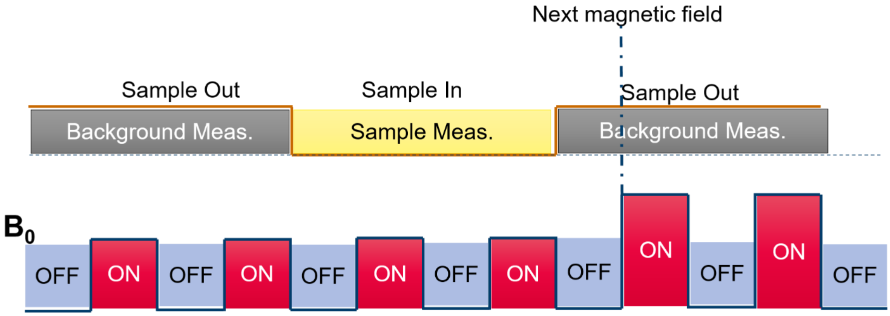

Figure 32. Pulsed offset field application explained schematically. The static offset magnetic field B_0 is pulsed with a specific duty cycle during which the background signal and the signal with sample is being measured.

Pulsing of the field resembles a square wave, where the high state means that the field is on, and the low state means the field is off. We can use the duty cycle to describe the active time of the static offset magnetic field. To determine the duty cycle where the temperature effects are minimized, the following experimental procedure was applied. To measure the temperature at the sample position, a temperature sensor of type 18B20 was embedded into a sample holder column such that it resides at the same position where later the real sample is positioned. An offset scan was done for the field range of interest with 70%, 50%, and 30% duty cycles. The results are plotted in Figure 33a. The sample was inserted and removed to mimic the actual measurement procedure. Thus, the upper envelope shows the temperature inside the measurement head at the measurement position, and the lower envelope of the measured graphs shows the temperature that the sample experiences when it is out of the measurement position. The 70%, 50%, and 30 % measurements are plotted as black, red, and blue solid lines, respectably. The initial temperature is denoted as T_i and the finally achieved temperature at the end of the measurement is denoted as T_f. The temperature difference $\Delta T = T_f - T_i$ was calculated for all three duty cycles. The 70% duty cycle produces a ΔT of 12.2 °C which is already less than in the mode where the coil runs continually. The minimum ΔT among the selected duty cycles was achieved with a 30% duty cycle with a ΔT of 5.29 °C. Hence, this duty cycle is adopted for all the static offset-dependent FMMD measurements done using the electromagnet offset module throughout this work.

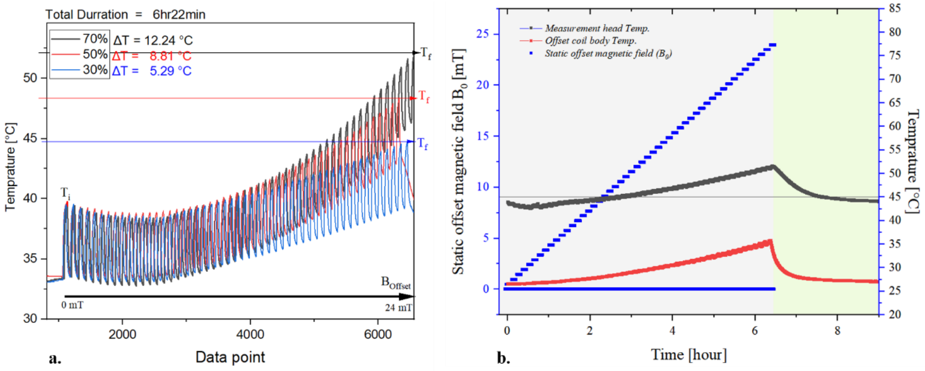

Figure 33. a) Temperature measurement in pulsed offset mode with 70% (black), 50% (red) and 30% (blue) duty cycle. b) Time trace of the pulsed applied static offset magnetic field (blue) and the progression of the temperature in the measurement head (black) and offset coil body (red)

Figure 33b shows the time trace of measurement head and coil body temperature in a pulsed mode in black and red color, respectively, and the applied offset field in blue. Since the applied offset field is pulsed, a blue line at zero level can be seen representing the off times of the pulse. In comparison to the measurement results provided in Figure 31, we can see that the highest temperature at the applied offset field of 24 mT is ~52 °C. This means a reduction of 23 °C. Additionally this reduced temperature reduces the recovery duration when the system goes back to the initial stabilized temperature of ~ 45 ± 1 °C.

The investigation involving the impact of this temperature reduction on the static offset magnetic field-dependent FMMD signals will be discussed further in chapter 7.

3.5. Portable permanent offset magnet design

In the previous section, an experimental setup for measuring the static offset-dependent FMMD signals based on electromagnet was introduced. However, due to the need for an external power source, such a setup is only suitable for laboratory conditions, and it lacks portability. Moreover, as discussed above, the setup exhibits some variation of the temperature due to the heating of the electromagnet, even in the pulsed mode with a 30% duty cycle. In this section, the design and characterization of a measurement head is discussed where the static offset field is applied through permanent ring-shaped magnets. Such a setup, although bulkier than traditional FMMD systems, reduces power consumption and can be made portable. The contents of this section have been partly published in [112].

3.5.1. Measurement head design

In this section, the design of a permanent magnet offset module (PMOM) measurement head is described. It utilizes the same configuration of the excitation and detection coils as described in section (3.1.2). Figure 34a shows the excitation coils placed and adjusted around the detection coil compartment for this particular system. A temperature sensor of type DS18B20 is utilized to control the internal temperature of the measurement head, and a light barrier sensor is used to react upon sample insertion. Furthermore, in this new design, we have embedded a Hall sensor of type Allegro A1324 to measure and monitor the static offset magnetic field change. The sample is inserted into the measurement head from above, and a light sensor is used to monitor the insertion and removal of the sample.

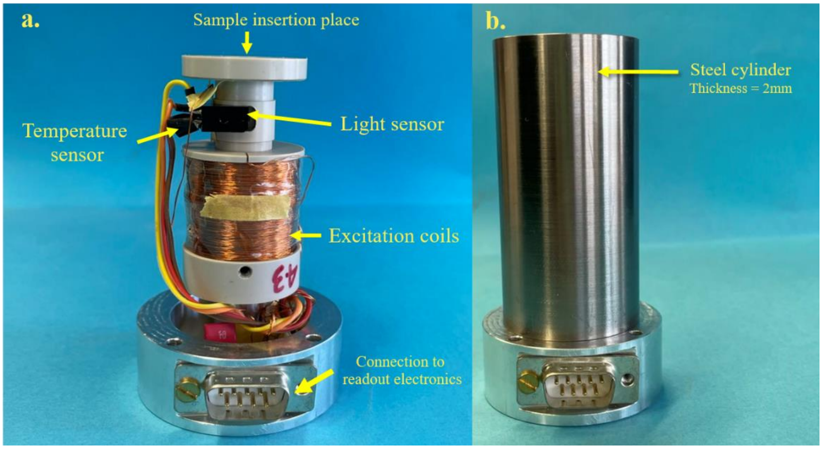

Figure 34. a) Measurement head without housing, AC excitation coils, light, and temperature sensor, b) Hollow steel cylinder placed around the measurement head, employed for attenuation and homogenization of the static offset magnet field.

Two ring-shaped ferrite permanent magnets with an internal diameter of 60 mm, an outer diameter of 100 mm, and a thickness of 20 mm purchased from Webcraft GmbH (Gottmadingen, Germany), are used to create the static offset magnetic field. Both ring magnets are inserted into larger internally threaded aluminum ring-shaped supports. The supports are then fastened onto the outer thread of the measurement heads housing, allowing their rotation to adjust the spacing between the two ring magnets. The supports are fastened such that their bottoms face one another, preventing the magnets from making direct contact. The attractive force between the two magnets holds the magnets inside their aluminium supports so that they don’t have to be glued or affixed otherwise. The static offset magnetic field can be increased or decreased by moving the magnets closer or farther apart from one another. To attenuate and homogenize the offset magnetic field, a hollow steel cylinder with an internal diameter of 35 mm and a wall thickness of 1.5 mm is inserted between the coil systems and the outside permanent magnets shown in Figure 34b. The thickness of the steel cylinder also determines the magnitude of the static magnetic field at its inside. The thicker the steel, the weaker the magnetic field. Thus, the choice of thickness determines the minimum and maximum magnetic field, in which range the static magnetic field can be adjusted. The design parameters have been optimized for manufacturing in [107]. Figure 35 depicts the measurement head's schematic design.

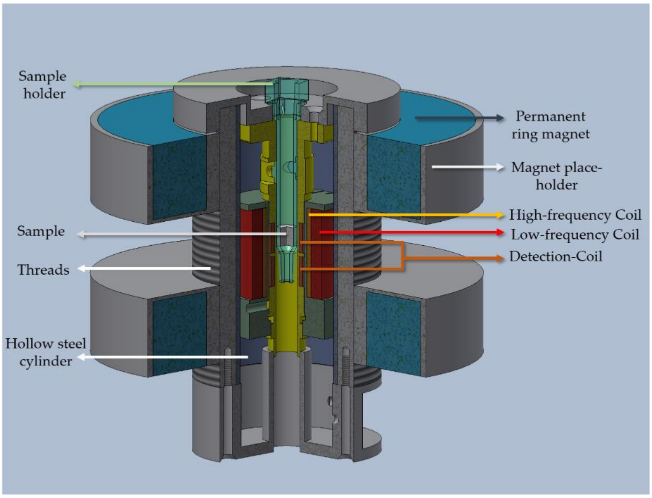

Figure 35. The schematic designee of the permanent magnet measurement head.

Characterization of the experimental setup was done through a set of experiments, also serving as further assessment for checking the practicality of the design. Initially, the characterization of the permanent ring magnets at different spacings is presented, and later, the characterization of the excitation signals and temperature dependency is given.

3.5.2. Characterization of static offset and AC excitation fields

The in-house assembled Hall sensor (A1324) used earlier for the characterization of the EMOM setup was used to measure the magnetic field generated through adjustment of the ring magnets at different positions. Figure 36 a and b show the ring magnets adjusted to their largest and their smallest distance. The magnets were adjusted with the help of labels affixed to the magnets, as seen in Figure 36c on the top of the measurement head. The Hall sensor was inserted in the measurement head, and the ring magnets were adjusted symmetrically through rotation around the threaded body of the housing. Figure 37 shows the measured magnetic field in 28 steps with a step width of 1 mm. The black squares represent the measurements taken while the magnets are moving towards each other, and the red squares show the measured data when the magnets move away from each other. From this, we obtain the dynamic range of applicable static offset magnetic fields, starting from 2 mT (at level 0) when the magnets are 29.6 mm apart from each other, until 26.5 mT (at level 27) at the closest possible position of the two magnets, just 2.6 mm apart from each other (determined by twice the thickness of the aluminium support holding each magnet). Additionally, as can be seen in the graph, we observe a weak hysteresis between levels 0 to 15 due to the presence of the steel cylinder, which has ferromagnetic properties and therefore exhibits hysteresis. This cylinder is needed as it is used for the attenuation and homogenization of the magnetic field. Thus, one has to keep in mind that for reaching a particular field value, the direction of the movement is important. Therefore, one should always adjust the measurement distance by approaching it from the same side. In our experiments, we measured the static magnetic field after each change of the magnet distances before inserting the sample.

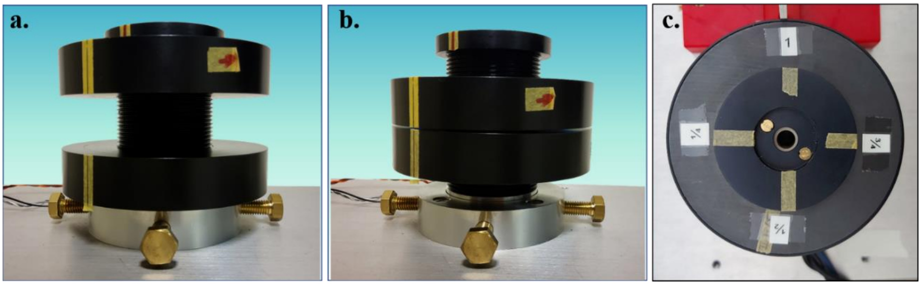

Figure 36. The PMOM measurement head a) the ring magnets placed far apart from each other, generating the smallest offset field, b) the ring magnets are moved to the closest position, yielding the largest magnetic field, c) markers placed for positioning the ring magnets through rotation.

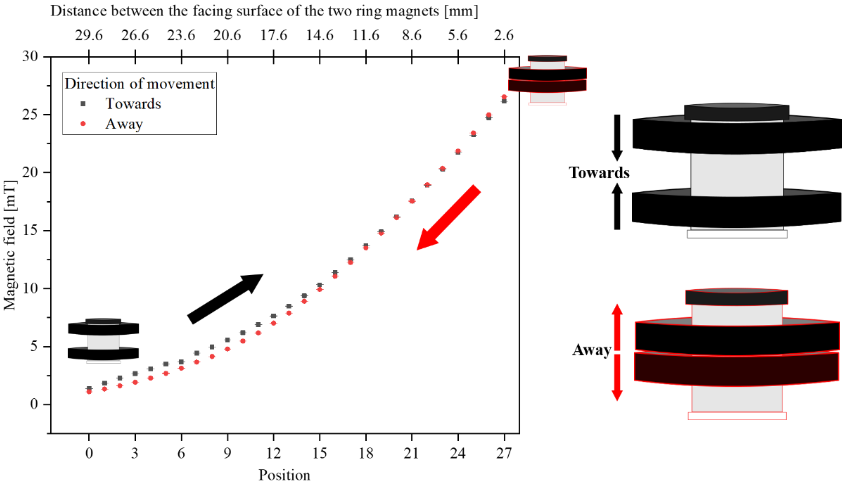

Figure 37. Dynamic applicable static magnetic field through PMOM, the magnetic fields were measured in 28 steps by moving the two permanent ring magnets towards each other (black squares), increasing the magnetic field, and then pulling them away from each other, decreasing the field (red squares).

The sinusoidal excitation magnetic fields generated by the electromagnets inside the measurement head were also measured. The low-frequency excitation coil is set to yield a magnetic field of 16.5 mT with a frequency of 63 Hz and the high-frequency excitation coil produces a magnetic field of 1.2 mT with a frequency of 40.5 kHz which is comparable with the EMOM setup.

The temperature development inside the measurement head was measured using the built-in temperature sensor and is depicted in Figure 38. The presented results were obtained during the measurement where the static offset field was varied to the maximum level. The figure highlights the initial warmup phase and the measurement phase shown in gray and green background color, respectively. In this setup, the temperature stabilizes around 35±1 °C. This value is lower than the EMOM setup’s stabilization value. However, as it can be seen in Figure 36, the metallic body of this measurement head is larger, which helps in reducing the overall temperature of the measurement head. Furthermore, in the measurement phase of the temperature recordings, we can see that the temperature fluctuates around 35 °C and stays within the same boundary throughout the measurement. The fluctuations are due to the insertion and removal of the sample which has a temperature less than that of the measurement head, thus affecting the readings of the temperature sensor.

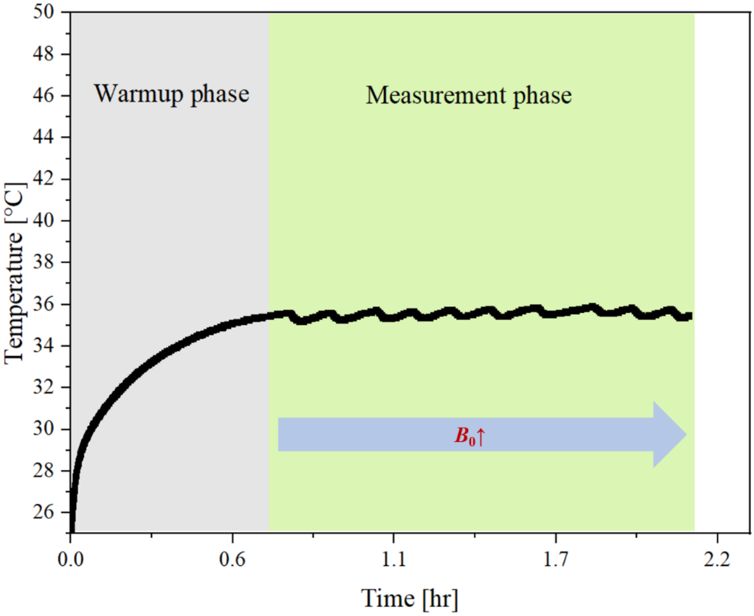

Figure 38. Trace of the temperature developments inside the PMOM setup. The gray area shows the warmup phase, and the green area highlights the measurement phase. During the measurement phase, the static offset magnetic field is changed, indicated by the pale blue arrow.

3.6. Determination of the calibration factor for each measurement harmonic

For quantitative measurement of MNP samples, the determination of the calibration factor of the magnetic reader is essential. In this section, the process for calibration of the magnetic reader system is presented.

The calibration can be done by using a well-defined synthetic magnetic moment which can be produced by means of an induction coil henceforth named as “test coil”. The magnetic moment of the test coil m_{coil} can be calculated as follows.

$$m_{coil} = N \cdot I \cdot A_{coil} \qquad \text{Eq.43}$$

where N is the number of windings, I is the current and A_{coil} is the area of the test coil.

A test coil of 5 windings using a copper wire with a nominal wire diameter of 0.2 mm was wound around a 3D printed coil former with a designated internal winding diameter of 5 mm. According to Eq.43, the test coil with an effective area of 21.2 mm^2 generates a magnetic moment of $1.061 \cdot 10^{-10}$ Am^2. To experimentally generate this magnetic moment, the test coil was supplied by AC current using a shunt of 10 kΩ connected to the output of lock-in amplifier SR 830 from Stanford Research generating an output voltage of 1V$_{\text{RMS}}$. Hence the generated magnetic moment is

$$m_{coil} = 5 \cdot \frac{1V_{RMS}}{1050\,\Omega} \cdot 21.2\,mm^2$$

$$= 1.011 \cdot 10^{-7}\,Am^2\,.$$

The test coil is placed inside the measurement head in such a way that it resides inside the detection compartment at the sample position. The trigger signal of one of the DDS chips (in this case DDS3) was supplied to the reference input of the lock-in amplifier so that a triggered frequency sweep can be performed. While both of the excitation coils are turned off, a frequency sweep is performed to supply the test coil with appropriate frequencies equivalent to the frequency mixing harmonics of interest. The readout of the detection coil is measured through the digital demodulation scheme. The background noise at each frequency is then subtracted from the measured values. Thus a calibration factor is determined for each frequency mixing harmonic in units of nAm^2/V$_{\text{RMS}}$. It is important to consider the conversion factor from V$_{\text{peak}}$ to V$_{\text{RMS}}$ in data analysis since the FMMD measurements using the digital demodulations are in Volts peak, whereas the Lock-in SR 830 displays rms voltages. The list of the frequencies and their corresponding calibration factors are presented in Table 8.

Table 8. List of frequency mixing harmonics of interest, and measured calibration factors at these frequencies.

Mixing harmonics	$f_1 - 4 \cdot f_2$	$f_1 - 3 \cdot f_2$	$f_1 - 2 \cdot f_2$	$f_1 - f_2$	f_1	$f_1 + f_2$	$f_1 + 2 \cdot f_2$	$f_1 + 3 \cdot f_2$	$f_1 + 4 \cdot f_2$
Frequency [kHz]	40.24	40.31	40.37	40.43	40.50	40.56	40.62	40.68	40.75
Calibration factor [nAm^2/V$_{\text{RMS}}$]	3822	3836	3850	3866	3880	3895	3911	3926	3941

Chapter 4

4. Sample preparation techniques

The preparation of samples plays a crucial role in every measurement technique. Various methods can be employed to prepare MNP samples for FMMD measurements. However, it is important to realize what property needs to be measured. Moreover, it is important to consider the media or the matrix where the MNPs will be suspended in or immobilized onto. For example, if we want to study the Brownian relaxation of MNPs (considering appropriate MNP size), we require a suspension. If the Néel relaxation is to be investigated, immobilization of the particles becomes necessary.

In standard magnetic immunoassays, which is one of the most important applications of the FMMD technique, often a porous polyethylene matrix is utilized, where the capturing agents are immobilized onto. By means of a sandwich or competitive immunoassay technique, the MNP markers that are indirectly bound to the matrix are detected. On the other hand, when MNPs themselves are investigated, e.g. for further characterizing their properties, for particle optimization, quality control, and for the development of new measurement techniques, the establishment of a simple and proper sample preparation technique plays an important role.

In this section, we will address different sample preparation techniques used with FMMD technology to investigate MNPs.

4.1. Liquid suspension

The simplest method of sample preparation is to produce a liquid suspension of MNP. Liquid suspension samples are used if one desires to study the MNP behavior in solution with respect to their hydrodynamic size, to investigate the effects of viscosity, to evaluate the magnetic response, or to compare the two relaxation mechanisms, Brownian vs Néel. However, one has to initially consider the stability of the MNPs in a solution, whether they are water-soluble or if organic solvents are required. The MNPs used in this dissertation are all commercially available water-soluble particles. Thus they may be suspended either in distilled water or in PBS solution.

The liquid suspension of MNP can be prepared by simply diluting a desired volume of MNP from the stock solution with distilled water in an Eppendorf conical tube, and later transferring it to a glass test tube for measurement.

4.2. Immobilization onto PE filter

Polyethylene (PE) filters have been used frequently across the publications involving the FMMD technique employed for MIA detection. The Hydrophobic (HP) PE filters used for experiments within this dissertation have been procured from Senova Gesellschaft für Biowissenschaften und Technik mbH Weimar, Germany. The filters are part of ABICAP® test kits, they are 3D immunofiltration columns, having dimensions of ∅5 mm × 5 mm, and have pores of approximately 50 µm inner diameter.

Figure 40 a) shows an example picture of such a filter. The filter is held in a plastic column. The geometry of the column allows for flow-through sample preparation.

To prepare the filter for sample preparation, several initial steps need to be taken to prime and equilibrate them. The equilibration process is graphically depicted in Figure 39. Initially, the selected number of filters for every batch must be packed within the columns. The column-filter unit is then placed in a container filled with ethanol (the level of ethanol needs to be slightly above the filter level). The container is then placed inside a desiccator which applies a slight evacuation of several mbar (does not need to be accurate) until the ethanol enters the columns and flushes into the pores of the PE filter. This incubation is continued for 30 minutes, after which the columns are removed, initially washed with ethanol-water solution (1:1), once for equilibration, and then twice with pure distilled water. The filters are then ready to be used for the next stages of the sample preparation, or they can be stored in a distilled water container for later use.

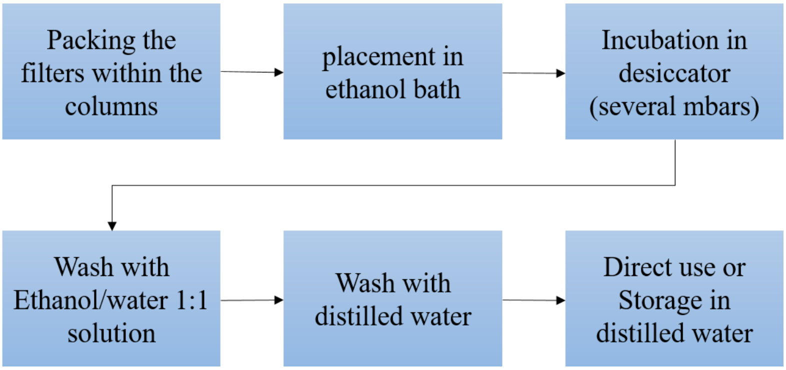

Figure 39. The process of priming the PE filters.

Another route for performing the equilibration process is batch preparation where only the bare filters without the plexiglass columns are primed. The filters are first incubated in an ethanol container (Eppendorf or Falcon tube) for 30 min with help of a laboratory shaker and then washed using the same washing solutions as stated earlier, but by incubating them in each washing solution for 10 minutes using the shaker.

To prepare the standalone MNP samples using PE filters, one has to consider that if the flow-through preparation technique is used, the immobilization of the MNPs on the filters depends on the nonspecific binding by electrostatic and hydrophobic interaction. Thus, the concentration of the MNPs immobilized on the PE will not be that of the original dilution, and it will lack reproducibility of sample preparation.

In the following, we will address two methods of preparation. In the case of using the flow-through preparation technique, an indirect method needs to be employed to determine the concentration of the MNPs remaining in the filter. In the case of the second method, the aim is to immobilize practically all of the MNPs in the dilution on to the filters.

Flow-through immobilization on the PE filters

The flow-through immobilization on the PE filter is done by initially preparing the desired MNP dilution. The MNP dilution is then pipetted into the column. The dilution flows through the porous PE filter and the MNP bind to the filter. The fluid drains from the bottom of the column. In the final phase, the filter is washed by pipetting 500 µL distilled water through the column. The steps of this preparation method are graphically shown in Figure 40.

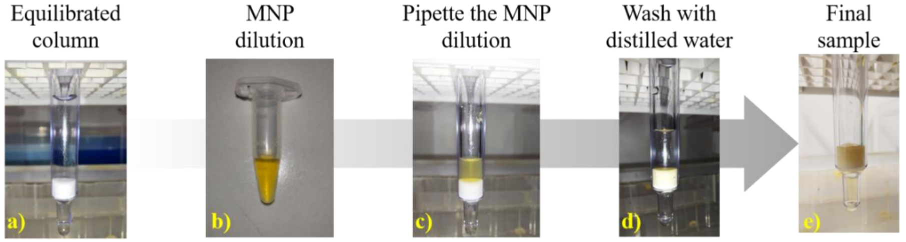

Figure 40. The flow-through sample preparation process for immobilizing the MNPs on a PE filter. a) Equilibrated filter, b) MNP dilution is prepared in an Eppendorf tube, c) the dilution is pipetted into the column where it flows through the pores of the PE filter, d) The filter is washed with 500 µL of distilled water to remove the unbound particles, and e) shows the final product.

Immobilization through evaporation

In this process, we try to immobilize the complete amount of MNPs in the dilution onto the PE filter to reduce the concentration loss. The general concept of the idea is that the filter is placed inside the dilution and then the fluid is evaporated so that the particles have to bind to the matrix. However, to avoid binding the MNPs to the glass surface, initially, the test tubes that are used for this process need to be processed. For preparing the test tubes, we use the siliconizing agent Sigmacote from Sigma-Aldrich®. This agent will create a thin layer on the surface of the glass tubes which prevents the binding. Within this preparation method, we have also used a heated copper block presented in Figure 41b. The block has a cylindrical hole with an inner diameter of 8.15 mm and a depth of 30.57 mm for inserting the sample. The steps for preparation through this method are given as follows.

- Glass test tube preparation: wash it with 300 µL of Sigmacote (by just pouring it in and out).
- MNP dilution is prepared by diluting the desired amount of MNP from the stock solution with distilled water inside the test tube.

- Place the equilibrated PE filter inside the test tube.
- Heat up the copper block to 70° C using a laboratory heater, e.g. IKA3380000.
- To speed up the evaporation process, incubate the sample and copper block in a desiccator.

A visual comparison between the filters prepared with and without Sigmacote coating of the glass tube is presented in Figure 42. One can see the MNP agglomerate on the inner surface of the uncoated glass tube, Figure 42(b), whereas the glass surface remains clean in the case of the coated glass tube, Figure 42(a). Quantitative evaluation will be addressed in the assessment section.

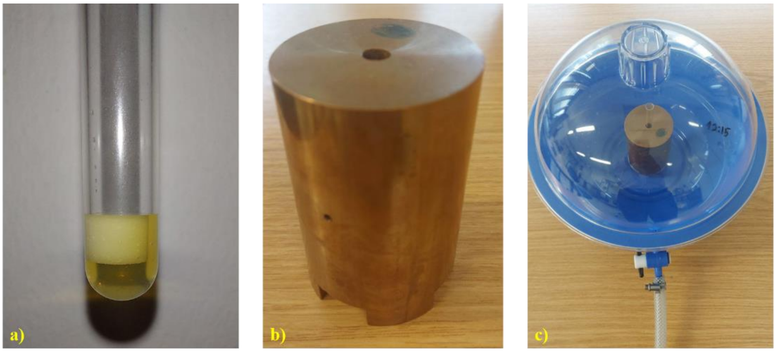

Figure 41. a) The PE filter inserted in the MNP dilution in a glass test tube b) Copper block used for heating the sample c) incubation of the sample and copper block in the desiccator.

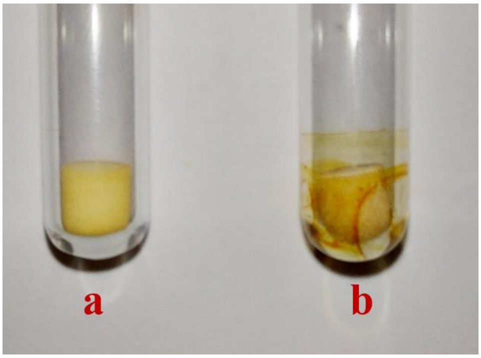

Figure 42. Comparison between the two samples which were prepared through evaporation-mediated technique. In a) the glass tube was pre-treated with Sigmacote® and in b) the Glass tube was used without pre-treatment.

4.3. Immobilization by epoxy embedding

Alternative to the PE filter immobilization procedure that was discussed earlier, immobilization of MNP by epoxy embedding was also explored. As a result of this sample preparation method, one can obtain a rigid solidified epoxy block with embedded MNP. Long-term storage of this preparation method makes it attractive as an example for preparing calibration phantom probes. In this preparation technique, we used two-component transparent epoxy resin (TOOLCRAFT brand).

For the preparation of such samples, a special container was designed and manufactured through 3D printing technology. The 3D model of the sample holder column is presented in Figure 43. The top of the holder is designed to provide an edge similar to the ABICAP columns which is used to position the sample in the detection compartment of the measurement head. The sample is to be prepared inside the sample compartment since the sample preparation includes mixing of epoxy and MNP. The holder needs to be placed upside down during the preparation process, as seen in the figure. The sample compartment is designed to match the dimensions of the PE filter. An extra height of 2 mm is provided to avoid overflow of the mixture and provide room for stirring.

The size of the sample is chosen to be ∅5 mm × 5 mm to match the size of standard PE filters. The procedure for the preparation of the samples is as follows. Preparation starts by dropping 2 drops of epoxy A into the container. In the next step, 10 µL from the stock solution is added. For a better mixture, 2 µL of surfactant Tween is added, and finally, 2 drops of hardener component epoxy B is added. The mixture needs to be mechanically mixed with the tip of a 10-100 µL pipette. After mixing, the pipette tip is carefully removed, and the mixture is left for the curing process. One has to note that the addition of surfactant will increase the curing time.

The expected drawback of this method is that due to the stickiness of the resin and the requirement of mechanical mixing, the prepared samples will suffer from inaccuracy in the determination of the actual embedded concentration, as it is inevitable to lose some particles with the residual resin remaining at the stirrer.

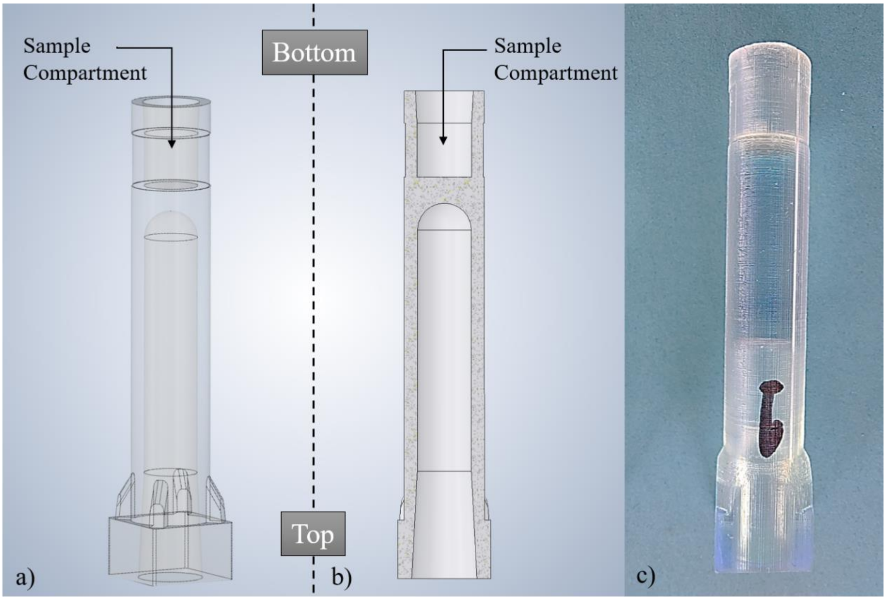

Figure 43. The epoxy-embedded sample holders. The columns are placed upside down in the pictures intentionally to show the orientation in which they are used during the sample preparation process, a) transparent 3D model of the column, b) the cross-sectional view of the model showing the sample compartment, and c) photo of the final 3D printed product.

4.4. Assessment and evaluation of different preparation techniques

To evaluate different sample preparation methods, one has to examine different aspects. The most important aspect of the sample preparation is reproducibility which is directly connected to the concentration in each of the samples. For this purpose, we used 10 µL of Synomag-D 70 nm magnetic beads to prepare the following samples. In liquid samples, 10 µL of MNP stock solution was diluted in 140 µL distilled water. To keep the same conditions, dilutions with the same concentration as the liquid samples were pipetted into the columns, followed by a washing step to remove the unbound particles. For every preparation technique, triplicate samples were prepared. The assessment was done by measuring the amplitude of the mixing frequency $f_1+2\cdot f_2$ in absence of a static offset magnetic field (B_0). The figure of merit in this case will be the standard deviation of FMMD measurements among the samples. The mean and standard deviation of the measured triplicate samples for Liquid suspension, Filter flow through and Filter evaporation preparations are shown in Figure 44 in form of a bar chart. The orange bar which belongs to the Flow through preparation technique shows a very large standard deviation. This is due to the unspecific binding issue. In MIA techniques, a specific capturing agent is initially immobilized on the filters to bind with the magnetic beads and to provide control over the binding.

The purple block shows the measurement of MNPs suspended in distilled water. We can see a much smaller deviation among the triplicates. The deviation may have been caused due to the pipetting error. The green bar in the middle shows the evaporation-based immobilization technique. By considering the deviation among the triplicate samples in the immobilized samples, we can see that filter-evaporation shows a considerable improvement compared to the flow-through immobilization technique. The flow-through preparation technique is used in immunoassay samples where a capturing agent is prepared. When immobilizing MNPs without a specific binding agent, particles will unspecifically bind to the filter.

When comparing the amplitude response of the immobilized to that of liquid suspension, an amplitude reduction of ~ 35% is observed between the liquid-suspended MNPs and the immobilized samples. The major cause of this reduction can be contributed to the involved particle dynamics. In the immobilized samples, the Néel relaxation mechanism dominates the effective relaxation time, and in the liquid suspension samples, both Brownian and Néel relaxation mechanisms occur and compete.

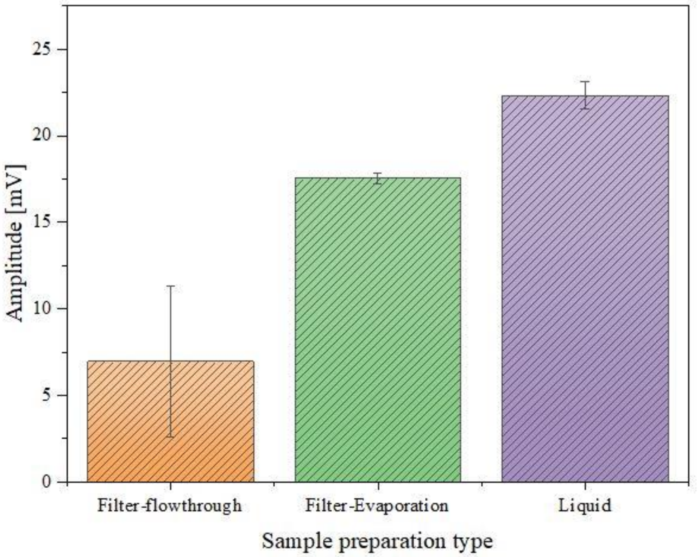

Figure 44. Mean and standard deviation of the prepared samples using different strategies.

In the preparation technique involving the embedding of the MNPs in an epoxy resin, as explained earlier, a mechanical stirring of the MNP and two epoxy components are required to obtain a homogenous sample. Thus, due to the stickiness of the resin, some of the intended concentration may be lost during the mixing process due to sticking to the tip and the body of the stirring tool.

Figure 45 shows the measurement of the triplicate epoxy samples. The MNP type used in this preparation is Nanomag-D spio with d_H =20 nm. Here we can see that in the lower range of particle concentrations, we can achieve better reproducibility which is indicated by the lower standard deviation among the prepared probes.

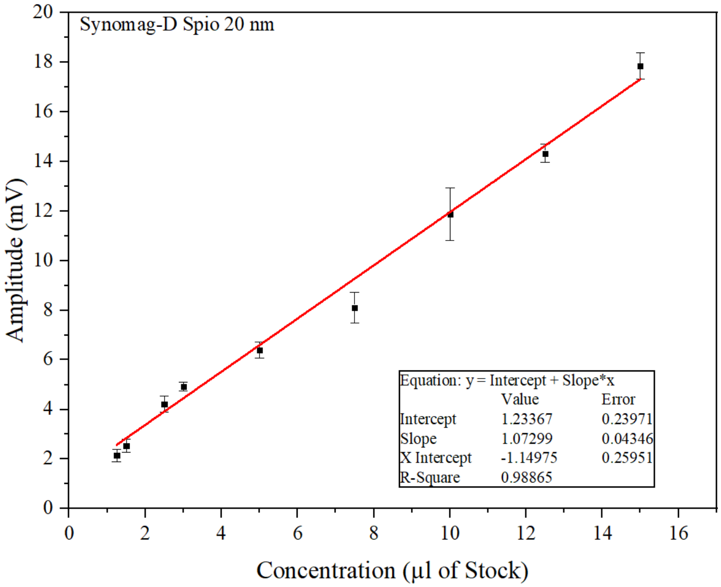

Figure 45. Mean and standard deviation of triplicate samples in different concentrations of MNPs immobilized in epoxy.

Among the different preparation techniques explored, judging from the reproducibility perspective, we see that both the liquid and evaporation-mediated immobilized samples are suitable candidates for our experiments that require immobilization and liquid suspension. However, the epoxy embedding technique requires a lot of experience and care and is a very user-dependent process. Despite that, due to the properties of the epoxy, one can make homogeneous samples, and also samples involving lumps of MNPs (see Figure 46) to further study their behavior.

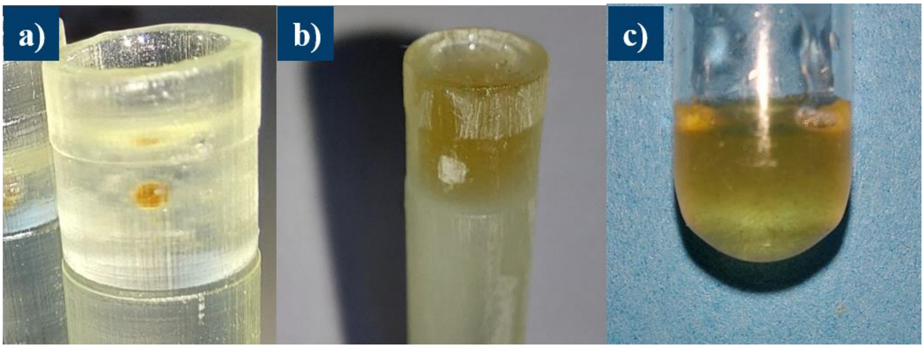

Figure 46. Sample preparation through embedding MNPs in epoxy. a) Centralized lump of MNP in epoxy, b & C) homogenous mixture in 3D printed column and glass tube.

Chapter 5

5. Static magnetic offset-dependent FMMD signal

In this chapter, the static offset magnetic field-dependent FMMD signal is discussed. Here, a simulation of the offset-dependent FMMD signals under the assumption of a lognormal magnetic core size distribution of MNPs is presented and discussed. Moreover, the measurements of different types of commercially available MNPs are analyzed.

Simulation of the offset-dependent FMMD signals in form of absolute amplitude assuming mono-core MNPs has been discussed in [107]. In a more realistic case, as mentioned in section (2.4), the ensemble of magnetic nanoparticles has been shown to follow a lognormal distribution. Using equations 38 and 39, one can calculate the magnetic response of the MNPs for even and odd mixing terms by choosing a lognormal distribution of core sizes d_c (d_0, σ) according to equation 20. We approach the assessment by initially observing the effect of varying d_0 parameter with a constant narrow σ, and then we analyze the situation where the distribution width parameter is varied for a constant d_0. Figure 47 shows the calculated lognormal distributions with varying d_0 from 6 to 24 nm in increments of 2 nm with a constant narrow distribution width ($\sigma = 0.05$). Respectively, Figure 48 shows the simulation of the first 4 mixing harmonics ($f_1 + f_2$, $f_1 + 2 \cdot f_2$, $f_1 + 3 \cdot f_2$ and $f_1 + 4 \cdot f_2$), assuming a million of lognormally distributed particles. The respective median core size diameters are color-coded in the figure. The simulations were performed with the settings of $B_1 = 1.29$ mT and $B_2 = 16.4$ mT for the excitation fields, which are the values used in the experimental setup as well.

The MNPs with larger cores exhibit a larger magnetic moment. It is also visible from the trend shown in the figure that the simulated signal from the distribution with larger d_0 yields a stronger nonlinear magnetic moment amplitude as expected.

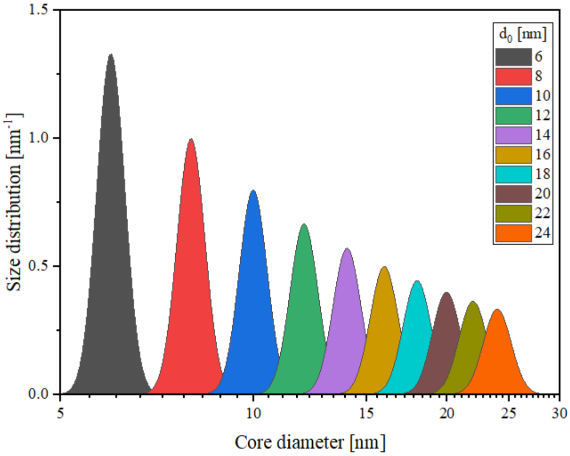

Figure 47. Lognormal distribution of core sizes with different median core diameters d_0 and constant σ of 0.05.

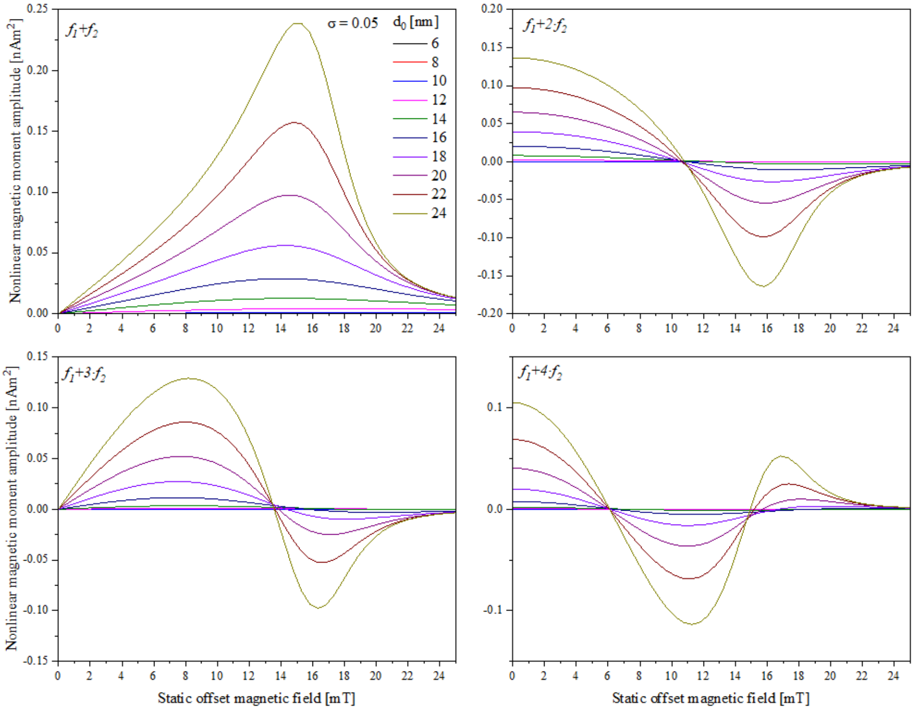

Figure 48. Simulated static offset magnetic field dependent FMMD signals of the first four even and odd mixing terms under the assumption of the lognormal distribution of magnetic core sizes for different distribution medians d_0 between (6 to 24 nm) and having a narrow constant distribution width σ of 0.05.

The static offset-dependent FMMD shows unique distinctive features such as extrema and zero crossings. The features are clearly visible in Figure 48. In our approach, we limit our measurements to the first four mixing signals, but it is also possible to measure and analyze the higher mixing harmonics as well. We can see that the mixing signal f_1+f_2

which is the first mixing term exhibits a feature in form of a maximum. The mixing term $f_1+2\cdot f_2$ yields two distinctive features as a zero crossing followed by a minimum. The third mixing term $f_1+3\cdot f_2$ initially expresses a maximum, then a zero crossing, and then a minimum. The fourth mixing harmonic $f_1+4\cdot f_2$ shows two zero crossings and two extrema. The first zero-crossing occurs in a lower limit of the static offset magnetic field, it is then followed by the occurrence of a minimum and then the second zero-crossing. At a larger static offset magnetic field, the final extremum feature occurs in a form of a maximum.

Other than the amplitude variation, closer inspection reveals that the position at which the features occur does also change upon variation of d_0. The simulated features were extracted, they are shown in Figure 49. In a), variation of the zero crossings have been plotted for different core diameters, and in b), the position of the extrema are plotted against the core diameter variation. The shown simulated range of the static offset magnetic field in this case is between 5 and 30 mT. The feature locations for some of the harmonics reside out of the selected range, meaning a larger static field is required to identify them. If we divide the core diameter axis into the lower (< 20 nm) and higher (>20 nm) field regions, we can see that drastic shifts in the location of the features occur in a lower core size diameter regime. For the larger offset field regime, the variation is minimal.

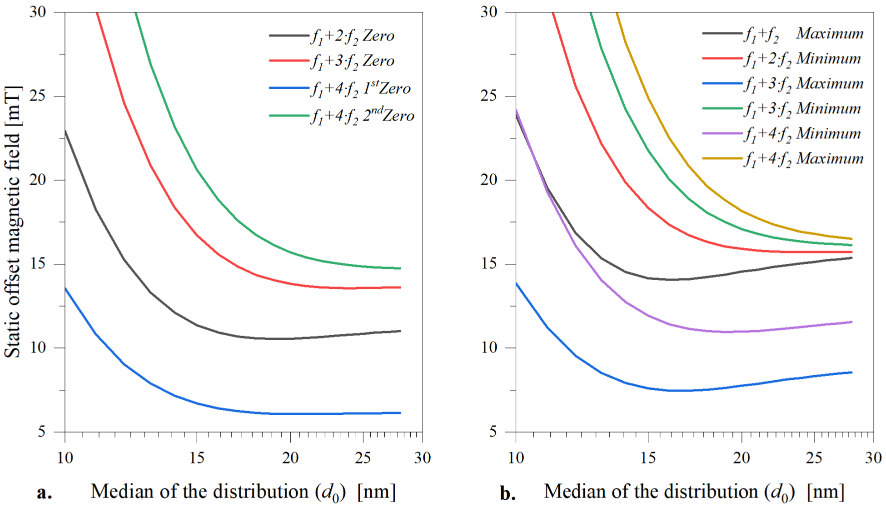

Figure 49. Location of offset static offset magnetic field dependent FMMD signal features for variation of the median (d_0) of the lognormal core size distribution with a fixed σ of 0.05. a) shows the location of zero crossings b)shows the location of extremums

Although the general trend observed here is the shifting of the features to the lower static offset magnetic field location, however, this is not completely true for the maximum of the f_1+f_2 and $f_1+3\cdot f_2$ shown in Figure 49b as black and blue curves, and for the minimum of the $f_1+4\cdot f_2$ which is shown as purple curve. They express local minima at 16.0 nm, 16.9 nm and 19.0 nm, respectively, after which the increasing trend is more pronounced in f_1+f_2 and $f_1+3\cdot f_2$.

The next effect to be studied here is the effect of variation of the distribution width σ on the FMMD signals. For this, static offset magnetic field dependent FMMD signals were simulated with a constant d_0, but with varying σ. Here the d_0 of the distribution was set to 15 nm and the parameter σ was varied from 0.05 to 0.20. The results are presented in Figure 50. In section (2.4), Figure 11, we saw that by variation of the sigma the maximum of the distribution shifts. Furthermore, we observed that upon increasing the distribution width, one also incorporates wider core-sizes. In Figure 50, we can see that as the distribution width increases, the magnitude of the nonlinear moment response also increases, and this is due incorporation of the larger core sizes.

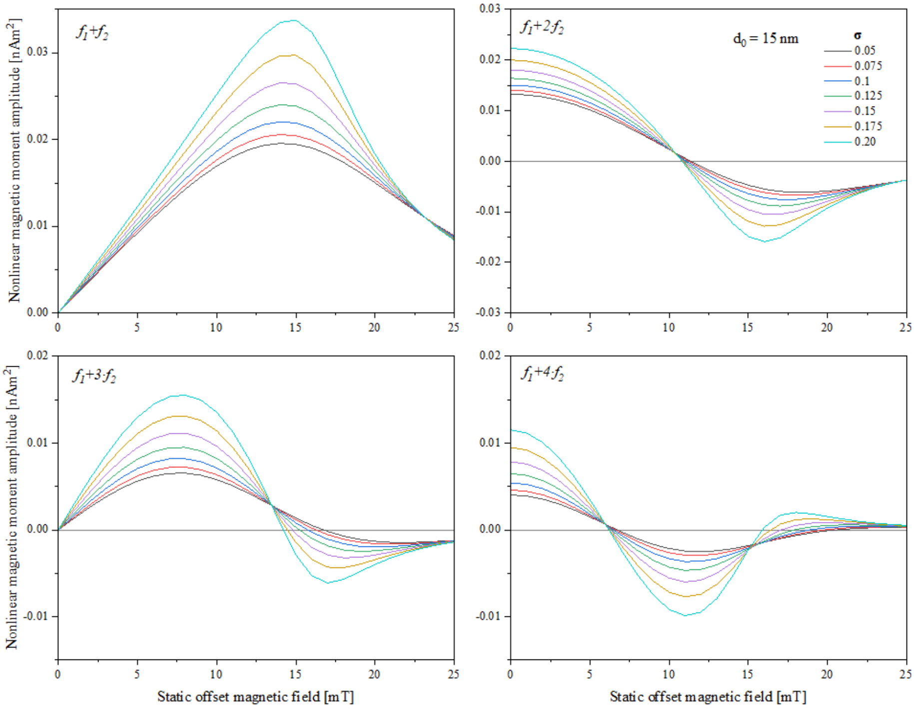

Figure 50. Simulated static offset magnetic field dependent FMMD signal of the first four even and odd mixing terms with an assumption of the lognormal distribution of magnetic core sizes for constant distribution median d_0 of 15 nm and varying distribution width σ in a range from 0.05 to 0.20.

5.1. Experimental results

Static offset magnetic field-dependent FMMD signals can be obtained through the experimental setups introduced in section (3.4). In this section, the measurement procedure and data analysis are discussed.

For measuring the static offset magnetic field-dependent FMMD signals, the experimental setup involving an electromagnet as an offset field generating source can be used.

A magnetic offset field scan was performed for an MNP sample prepared in an immobilized state. (for details of sample preparation, please refer to sample preparation chapter 6). The MNP used is of type SynomagD 70 nm. Static offset magnetic field-dependent FMMD signals were measured for the first four mixing harmonics.

The measurement results were treated in the complex plane, as was explained in section (3.3.2). The results of the background subtracted signals in the complex plane is presented in Figure 51a. The respective mixing harmonics are color-coded accordingly. The different data points of each color belong to different values of the static offset magnetic field. A phase angle is noticeable in all the mixing harmonics. The measured phase here is a combination of different contributions both from the measurement device and the MNPs. The details of the phase are described in the next chapter, there the contribution of each part to the measurement will become clearer. However, since we are only considering the magnitude of the measured signals at this stage, one has to further process the measured data. One can either calculate the absolute amplitude of each processed harmonic, or, in order to preserve the original shape of the signals, one can perform a so-called phase correction by projecting the measured data on to the real axis. This can be performed using the rotation matrix approach as follows.

$$\begin{bmatrix} \cos\varphi & -sin\varphi \\ sin\varphi & \cos\varphi \end{bmatrix} \cdot \begin{bmatrix} Re \\ Im \end{bmatrix} = \begin{bmatrix} Re\ cos\varphi - \ Im\ sin\varphi \\ Re\ sin\varphi + Im\ cos\varphi \end{bmatrix} \qquad \text{Eq.44}$$

$$\varphi = atan(\frac{Im}{Re}) \qquad \text{Eq.45}$$

Here, Re and Im are the real and imaginary part of the background-subtracted data, respectively. Moreover, φ is the angle that is used for the rotation. It is determined using the slope of a linear fit to the respective mixing harmonic data.

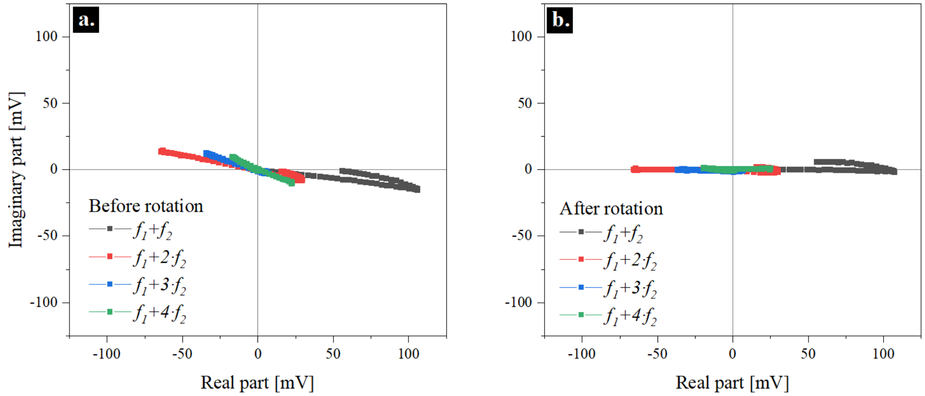

Figure 51. The complex plane plots of the first four static offset magnetic field-dependent FMMD signals. a) Before phase rotation, b) after phase rotation.

After the phase rotation (correction) depicted in Figure 51b, the amplitude of the real part of the data can be used for further analysis. Figure 52 shows the amplitude of the real part of the above-corrected data as a function of varying static offset magnetic field in the range of 0 to 24 mT with a field resolution of 0.48 mT. The mixing frequency harmonics $f_1 + f_2$, $f_1 + 2{\cdot}f_2$, $f_1 + 3{\cdot}f_2$ and $f_1 + 4{\cdot}f_2$ are presented as color-coded solid squares. The connecting line serves as a visual guide. From here one can immediately recognize the FMMD signal patterns introduced in the earlier section via the simulations. Moreover, in the measurement of this particular sample, we can clearly see the features of the magnetic offset-dependent FMMD signals in form of zero-crossings and extremums.

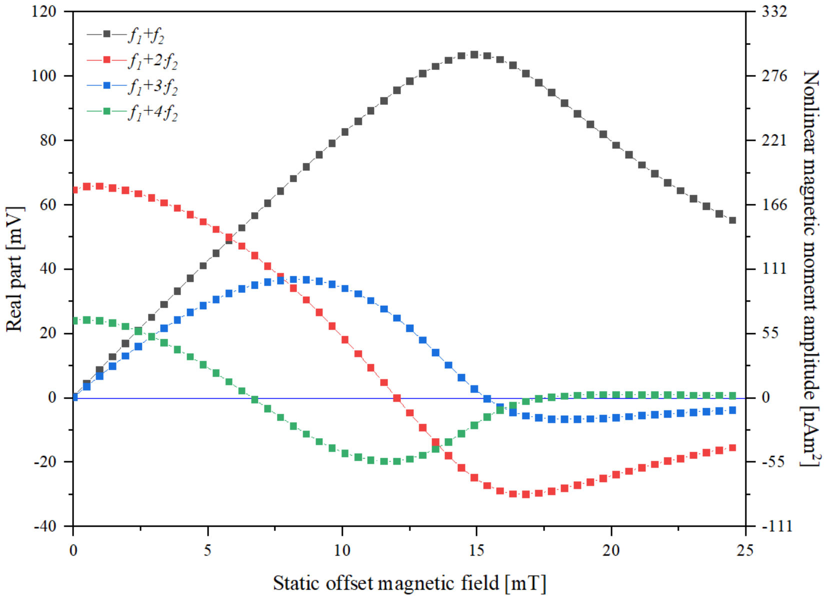

Figure 52. Amplitudes of the real parts of the measured signals after phase rotation

The amplitude of the phase-corrected signal can then be converted to the unit of the magnetic moment (nAm^2) using the calibration factor determined in section (3.6). Hence, the vertical scale at the right side of the figure shows the nonlinear magnetic moment amplitude of the sample in units of the magnetic moment.

5.2. Static offset-dependent FMMD signal evaluation

In this section, the measurement signals obtained using the EMOM module in continuous and pulsed mode are compared with the measurements taken with the PMOM module. The impact of temperature drift on measured FMMD signals is addressed in this section.

To evaluate the static offset-dependent FMMD signal, we measured a magnetic nanoparticle sample of type Synomag D 70 nm in an immobilized state. The sample was measured initially using the PMOM setup, and then the same sample was measured using the EMOM setup, both in pulsed and continuous mode.

The background signal and the signal generated due to the presence of the sample were measured at each offset field level. After measurement and background subtraction, a phase correction of the signals was performed. The temperature development and its impact on the measurement signal were assessed through a comparison of the measurement signal of the first even frequency mixing harmonic (f_1+f_2). In the case of the EMOM setup, the offset range was varied from 0 to 24 mT in steps of 1 mT, and in the case of PMOM, the full dynamic range from 2 mT to 26.5 mT (as mentioned above) was used. For comparison in Figure 53, the static offset magnetic field range is set to cover 0 to 24 mT. The measurements done with EMOM-continuous, EMOM-pulsed and PMOM are presented as solid squares in black, red, and blue, respectively, and are connected by lines as a visualization aid. The respective temperature development in the measurement head has been plotted in the same graph using solid lines with matching colors. We can see that the temperature reaches almost 75 °C at the maximum field at the end of the scan in the case of continuous mode EMOM. However, using the pulsed mode, the temperature variation is substantially reduced by ~23 °C. On the other hand, there is practically no change in temperature observed in the case of permanent magnets, as expected. The temperature fluctuates just weakly around the initial temperature of the system. This shows that the temperature increase in other modes is not due to the FMMD part of the measurement head, but it is rather the contribution of the electromagnet for offset field generation. For comparison, four different sections have been marked in the graph, labeled a. to d., to observe the trend of signal change due to the temperature drift of the system. The values are listed in Table 9.

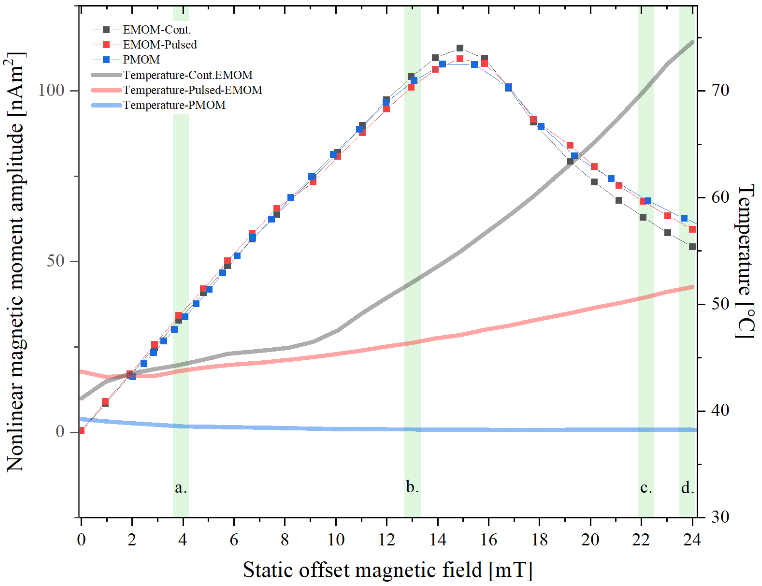

Figure 53. Nonlinear magnetic moment trace of sample Syn70 measured with PMOM setup (blue squares), and with EMOM setup in pulsed (red squares) and continuous (black squares) mode over field range of 0 to 24 mT, for mixing harmonic f_1+f_2. The temperature development in the measurement head is plotted for each case as faded solid lines with matching colors.

A detailed analysis of the origin of the temperature dependence of FMMD signals is beyond the scope of this thesis. However, one issue needs to be briefly addressed. We compare the pulsed and continuous modes of EMOM since the static offset magnetic field is the same in both cases. We observe that in the region where the temperatures of both modes start to deviate but are still very close to each other, the absolute variation in the measured amplitude is ~1.3 nAm^2. The variations in regions b, c, and d reach 3, 4.5, and 5 nAm^2, respectively. On the other hand, the temperature variations are minimal in the PMOM setup. Comparing the EMOM-pulsed and PMOM in the same regions, we see a maximum absolute deviation of less than 3 nAm^2. It needs to be taken into account that the setups do not yield the exact same magnetic fields and that the highest deviations are observed at the points where the static magnetic offset fields are slightly different.

Table 9. Temperatures and nonlinear magnetic moment amplitudes recorded in the three measurement modes at different offset field regions, as marked in Figure 53.

Region	**Temperature [°C]**			**Nonlinear magnetic moment amplitude [nAm^2]**		
	EMOM-Pulsed	**EMOM-Cont.**	**PMOM**	**EMOM-Pulsed**	**EMOM-Cont.**	**PMOM**
a	43.75	44.31	39.00	34.16	32.84	33.73
b	46.37	52.10	38.60	101.03	104.07	103.03
c	50.62	69.90	38.25	67.56	62.97	67.83
d	51.60	74.56	38.50	59.41	54.33	62.714

For further comparison, we use the measured data. Figure 54 shows the traces of the first four frequency mixing harmonics (f_1+f_2, $f_1+2{\cdot}f_2$, $f_1+3{\cdot}f_2$, and $f_1+4{\cdot}f_2$) for the measurement sequences of the pulsed-EMOM setup and the PMOM setup. The solid squares indicate the measurements performed using the pulsed-EMOM setup, and the solid red circles show the measurements performed using the PMOM setup.

For comparison, the corresponding field data of PMOM was extracted by doing a spline fit and calculating the total mean percentage error to the EMOM-Pulsed data. One can see that both measurements are in good agreement which each other, with a mean percentage error of 4.5 %.

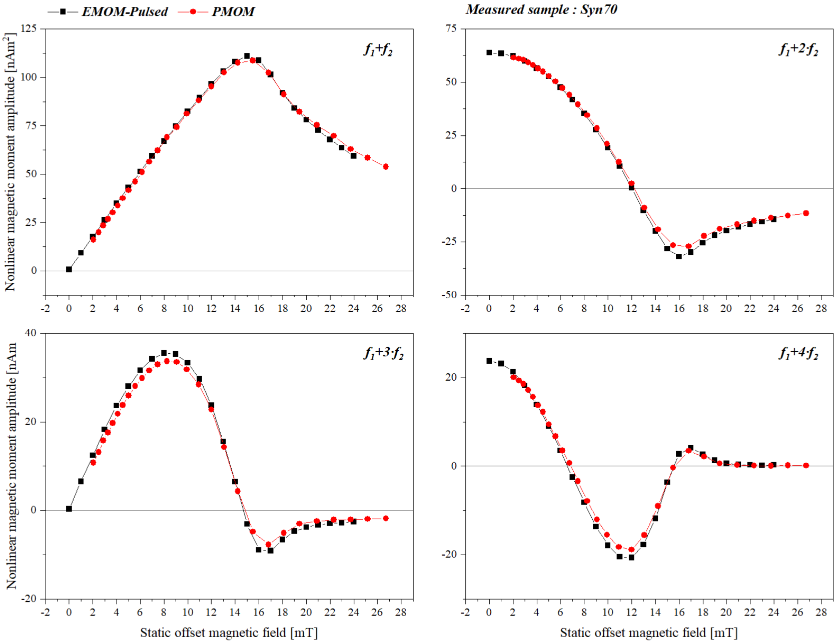

Figure 54. Nonlinear magnetic moment trace of sample Syn70 measured with EMOM-Pulsed setup (black squares) over a field range of 0 to 24 mT and the PMOM setup (red circles) over a field range of 2 to 26.5 mT, for mixing harmonics f_1+f_2, $f_1+2{\cdot}f_2$, $f_1+3{\cdot}f_2$ and $f_1+4{\cdot}f_2$.

A good way to compare the measurement signals obtained from these two systems with each other is to compare the location of the features of the FMMD signals (i.e. the extremums and zero-crossings). The locations of the extremums of the measured sample with two systems are presented in Table 10. If we consider the electromagnet setup as a reference, we can see that the feature locations measured by the permanent magnet show a deviation of less than 1.5 %. The observed deviations are in the acceptable range, however, the reason behind these small deviations could be due to small differences in the excitation field amplitudes of the two systems, and the different system temperatures at which the sample was measured.

Table 10. Comparison between the locations of the characteristic features of the sample Syn70 measured with EMOM and PMOM setup.

Mixing term	**Feature**	**Syn70-EMOM feature location [mT]**	**Syn70-PMOM feature location [mT]**	**Difference [%]**
f_1+f_2	Maximum	15.06	14.95	0.73
$f_1+2\cdot f_2$	Zero	12.03	12.2	1.41
	Minimum	16.13	16.36	1.42
$f_1+3\cdot f_2$	Maximum	8.35	8.41	0.71
	Zero	14.60	14.83	1.5
	Minimum	16.56	16.80	1.4
$f_1+4\cdot f_2$	1st Zero	6.57	6.65	1.2
	Minimum	11.54	11.52	0.17
	2nd Zero	15.57	15.63	0.38
	Maximum	16.99	17.11	0.70

5.3. Amplitude of the excitation signals

The characterizing parameters of the excitation magnetic fields can be described by their frequency, amplitude, and phase. In the experiments involved in the scope of this thesis, a fixed frequency is used, as described in chapter 3. The phases of the excitation signals are described in the next chapter. In this section, we briefly report on the effect of amplitudes of the excitation fields on the measurement signals.

From the theory, we know that the driving field brings the magnetization of the particles to the nonlinear regime, and the excitation field B_1 probes the magnetization. Initially, we look at the amplitude of the B_1. To investigate, measurements were performed using the Syn70 immobilized sample. The amplitude of B_2 was set to its highest value (16.4 mT), and the amplitude of B_1 was varied in 8 steps from 1.6 to 0.36 mT, and for each variation, static offset magnetic field scans were performed. The results are presented in Figure 55.

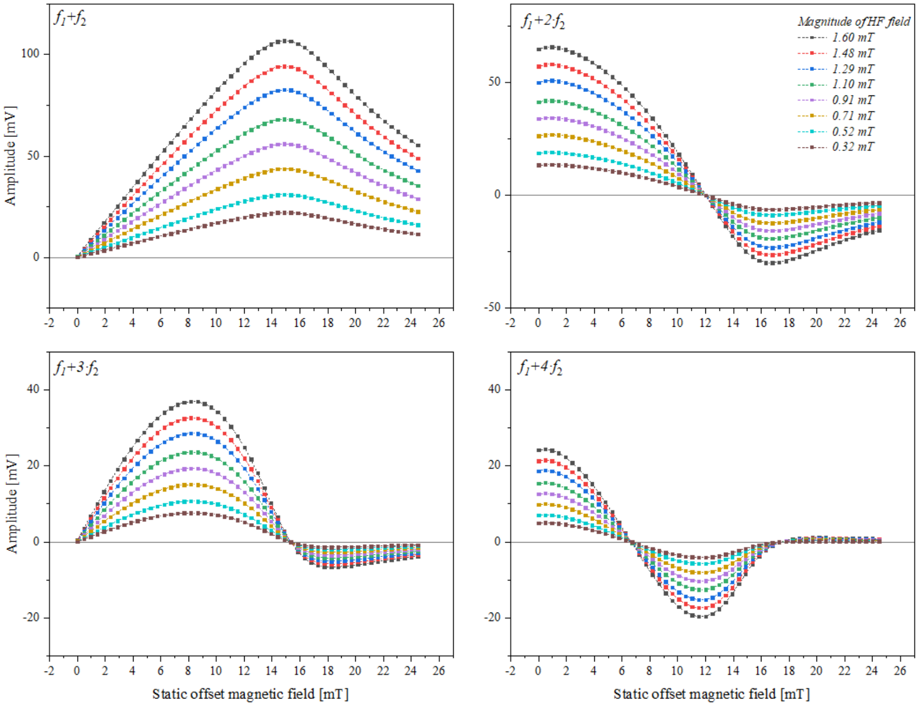

Figure 55. Static offset magnetic field trace of sample Syn70 for the varying magnitude of B_1 field. Different fields are color coded.

The analysis of the results suggests that amplitude variation of the B_1 field scales the amplitude of the measured signals, whereas the feature locations don't change. With our system, to measure a high amplitude response with good SNR, it is useful to set it to the highest value of 1.6 mT. However, when performing measurements of very highly concentrated samples, or changing to the resonance frequency of the detection coil, the measured signal may exceed the ADC range. So in these cases, the amplitude of this excitation field can be reduced.

Furthermore, to investigate the effect of the B_2 variation, a series of measurements were done where the amplitude of B_2 was varied, and for each variation, offset field scans were conducted. Figure 56 shows the static offset magnetic field traces of the mixing harmonics for variation of the B_2 amplitude which are color-coded.

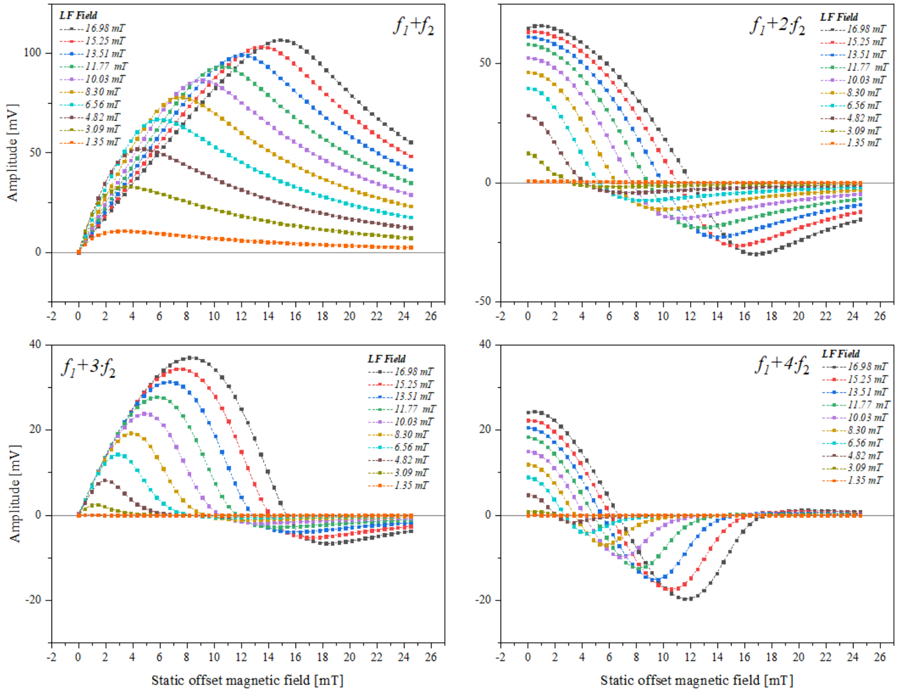

Figure 56. Static offset magnetic field trace of sample Syn70 for the varying magnitude of B_2 field. Different fields are color coded.

By reducing the amplitude of the driving field, different locations of the nonlinearity are probed. Hence, by analyzing the measurements, we can see that by reducing the amplitude of the driving field, the features of the FMMD signals linearly shift towards lower static offset fields (see Figure 57). Features for every mixing harmonic were extracted by fitting the specific region with an appropriate function. The extraction was done for every field scan. In Figure 57, a), b), c) and d), the extracted features of the mixing frequency signals f_1+f_2, $f_1+2{\cdot}f_2$, $f_1+3{\cdot}f_2$, $f_1+4{\cdot}f_2$, respectively, are shown. As it is also visible in the earlier figure at the lowest B_2 value, the determination of the features becomes problematic due to lower amplitude responses. The extracted patterns have been fitted with a linear function and exhibited a very good fit quality with $R^2 > 0.98$.

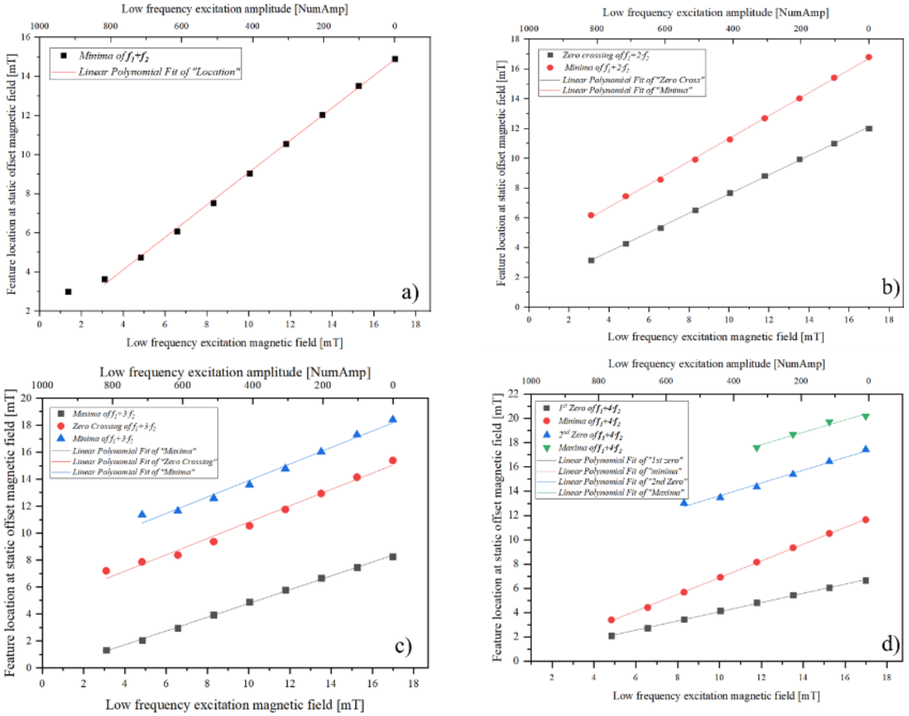

Figure 57. Dependency of the feature locations of FMMD signal on the amplitude of the B_2..

We can conclude that the amplitude of B_1 scales with the amplitude responses obtained in the measurements, and does not change the locations of the features. This is important when measuring a sample that has a high concentration and yields a high magnetic response. The obtained value will be out of the measurement limit of the ADC. Hence, the magnitude of B_1 can be adjusted for such measurements without influencing the feature locations. On the other hand, we have seen that by varying the amplitude of B_2, not only the amplitude response is reduced, but we are probing different regions of the magnetization curve. The location of the features (Extremums and Zero-crossings) would shift to the lower offset levels. This information can be utilized in the future to optimize the excitation fields for different particle types as well as reducing the power consumption of the magnetic reader.

5.4. Offset-dependent FMMD signals of MNPs in different states

The sample of magnetic nanoparticles can be prepared in different media. For example, as seen earlier, samples can be prepared by mixing the magnetic particles in aqueous solutions or fluids with different viscosities. Investigation of particle response signals in different viscosities is important since it can be applied to complex fluids such as blood. Moreover, when the magnetic immunoassay samples are prepared, the immobilization matrix (PE filter) is wet. Hence, the difference between wet and dry filters needs to be investigated in order to study the effects involved. In the liquid suspension, both the Néel and Brownian relaxation contribute to the response of the MNPs. However, in the immobilized state, the Brownian relaxation is suppressed, and the signal comes from the Néel relaxation mechanism.

For assessment between the immobilized and liquid-suspended particles, two types of samples were prepared, measured and analyzed. The MNPs under investigation were of type Nanomag-D spio 100 nm (ND100) and Perimag 130 nm. The specification of the particles according to the manufacturer are presented in Table 11.

Table 11. Specification of the MNPs stock solutions used in the experiments.

Particle Type	**Hydrodynamic size d_H [nm]**	**Stock concentration [mg/ml]**	**Coating**
Perimag	130	25	Dextran
Nanomag-D-spio	100	5	Dextran

Triplicate samples were prepared from each state. Comparison between the samples at each state was performed by evaluating the normalized FMMD signals. The normalization was done by dividing each mixing harmonic by its maximum value. Hence the variation due to amplitude differences are normalized, thus the specific features and patterns can be studied. Figure 58 shows the normalized FMMD signals for the first four frequency mixing harmonics of the particle type Perimag 130 nm (Peri130) for the two states liquid and immobilized. The liquid suspension state is depicted as solid black squares and the immobilized state in solid red circles. The difference among the signal patterns of the two states is more pronounced in the mixing harmonic f_1+f_2. Qualitatively, if we divide the measured signal into three regions, named as (Increasing, Peak and Decreasing), we can see that in the case of this particular MNP type, the initial phase of the measurement of the immobilized state is characterized by a linear increasing pattern whereas the measurement for the suspension state shows a curvature. The suspension state shows a narrower peak then the immobilized state, and a slight peak shift towards the lower static magnetic offset fields is observed in the case of the immobilized state measurement. In the final decreasing region, the suspension shows a more curved trajectory than the immobilized state. Further comparison was done by obtaining the FWHM of both signals which yielded for the immobilized state a value of 12.78 and for the suspension a value of 9.41.

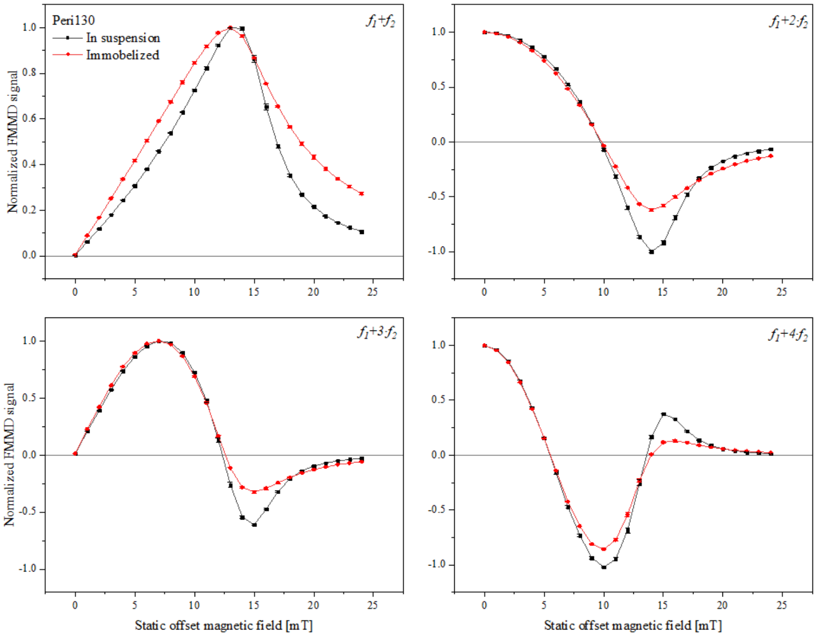

Figure 58. Normalized FMMD signals for the first four frequency mixing harmonics of the particle type Perimag 130 nm (Peri130) for the liquid suspension and immobilized state.

In the case of the other measured mixing frequency harmonics, we can see that patterns for both states closely follow each other, up to a certain static offset magnetic field level, after which the deviations between the pattern of both signals increase. The critical static offset magnetic field level for measurement harmonic signals $f_1+2\cdot f_2$, $f_1+3\cdot f_2$ and $f_1+4\cdot f_2$ is ~ 10, 12 and 6 mT, respectively. Moreover, analyzing the tail ends of the harmonics $f_1+2\cdot f_2$ and $f_1+3\cdot f_2$, we see that the suspension state crosses over the immobilized state measurement due to the faster growth rate after the occurrence of the local extremum. It is essential to note that further theoretical and experimental studies are required to elaborate on the origin of the difference between the observed shapes of the traces. However, when the particle type is known, the observed difference in the trends of the two signals can be used phenomenologically to distinguish between the two states.

Chapter 6

6. Phase of the FMMD signal

In FMMD technology, the two alternating excitation fields operate at different frequencies. In our design, the excitation signals are generated through DDS chips explained in (3.1.1). In theory, it is assumed that both excitation fields are synchronous and there is no time delay between them. However, in experimental setups, one must verify that, and adjust the phase of the excitation fields in such a way that minimal asynchronicity is achieved. It should be noted that it does not suffice to adjust the phases of the DDS chips to 0 for both high and low-frequency excitation signals since both amplification branches for providing the coil currents exhibit different phase shifts. One has to make sure that the coil currents at high and low frequencies are both starting with phase zero. Moreover, some of the contributing factors to the final measured phase of the signals are listed in the diagram presented in Figure 59, classifying them into three main categories of excitation field phase, demodulation phase and MNP response phase. Apart from the phase shift coming from the MNPs, the contributions of excitation and demodulation chains need to be characterized so that phase shift due to the particles' presence can be deduced. For example, the frequency-dependent phase shift of the excitation fields and its effect on the measured signals needs to be studied.

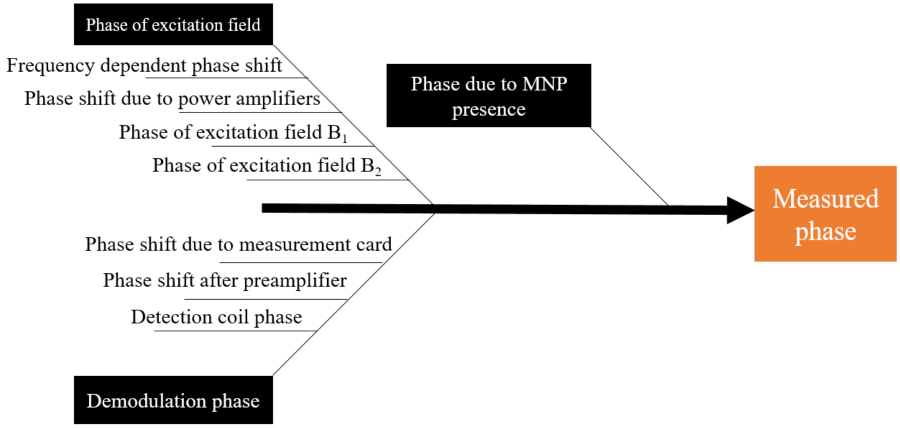

Figure 59. Contributing factors to the measured phase of FMMD signal, classified into three main categories of excitation field phase, demodulation phase and MNP response phase.

In this section, we examine the consequence of such asynchronism, initially through simulations, highlight the important behaviors of the signals and finally assess the simulation results through experimental verification. Moreover, at the end of this section, our protocol developed for the calibration of the excitation fields is presented.

6.1. Simulation of offset-dependent FMMD signals with varying excitation phases

Offset-dependent frequency mixing magnetic detection signals can be simulated using equations (38 and 39) for each mixing harmonic.

Moreover, each of the excitation fields can be described through:

$$HF_{Field} = B_1(2\pi f_1 t + \varphi_1) \qquad \text{Eq.46}$$

$$LF_{Field} = B_2(2\pi f_2 t + \varphi_2) \qquad \text{Eq.47}$$

where φ_1 and φ_2 are the phases of the excitation fields.

In this simulation, we will observe the behavior of the two symmetric harmonics (i.e. $f_1 \pm n \cdot f_2$, $n \in \mathbb{N}$), through variation of the excitation field's phase. Initially, the signals are visualized in a 2-dimensional complex plane using the in-phase and quadrature (i.e. out-of-phase) components, and later for better understanding, a 3-dimensional visualization of the offset-dependent signals is provided.

It is clear that according to equations (38 and 39), the adjacent mixing harmonics have a 90° phase difference from each other, due to the alternating *sin* and *cos* multiplication. Hence, when we set both of the excitation phases to 0°, the in-phase component (real part) of the even mixing harmonics (f_1+f_2 and $f_1+3 \cdot f_2$) will be minimum and the quadrature component (imaginary part) will be at its maximum. In the case of the odd mixing harmonics ($f_1+2{\cdot}f_2$ and $f_1+4{\cdot}f_2$), the amplitude of the in-phase component will be at its maximum and the amplitude of the quadrature component will be at its minimum. This can be seen in Figure 60, here the first 4 positive and negative symmetrical frequency mixing harmonics have been simulated, with all the excitation and demodulation phases set to 0°, over a varying offset range from 0 to 24 mT. Zero phase means that both of the excitation frequencies are initially synchronous.

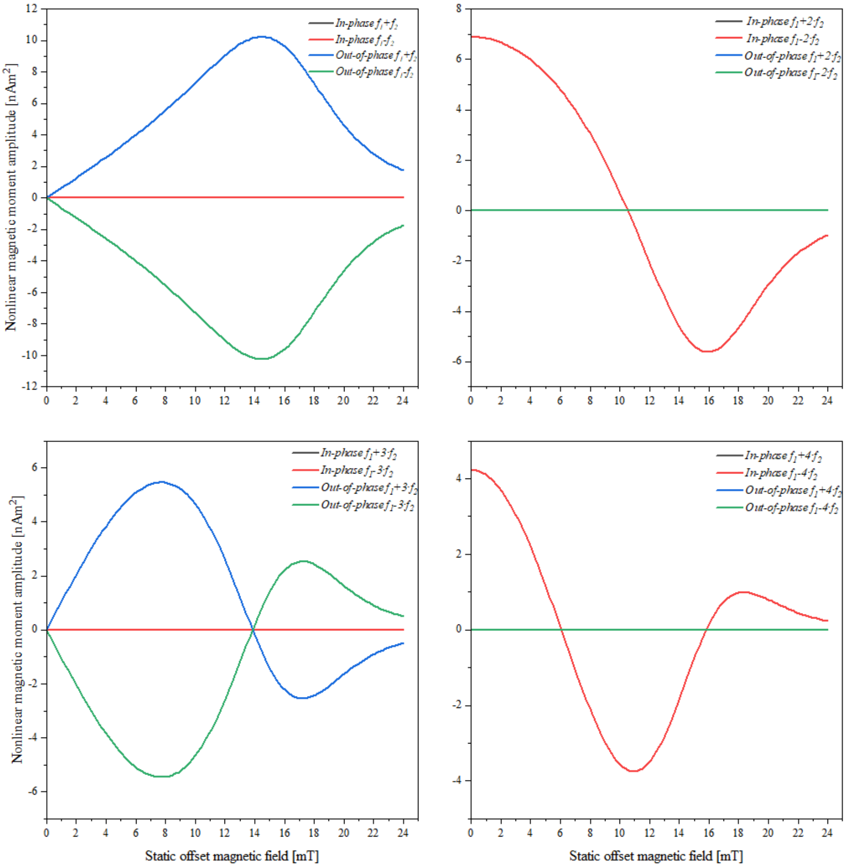

Figure 60. Simulation of in-phase and quadrature components of the offset-dependent FMMD signal assuming synchronous excitation fields.

It can be seen that the positive and negative even symmetric frequency mixing harmonics, exhibit a phase shift 180° apart from each other. On the other hand, the negative and positive odd symmetric harmonics are superimposed on each other.

6.2. Consequence of excitation phase desynchronization

In the development of the experimental setup of FMMD technology, as explained in the earlier chapter 3, two excitation signal generation sources are utilized. These two sources can either be laboratory signal generators synchronized with the same time base or in the case of a single on-board hand-held device, direct digital synthesis chips are used. One has to take into account that since we are using two frequencies that are far apart from each other, frequency-dependent phase shifts may arise which will result in asynchronism between the low-frequency and high-frequency excitation fields. In this section, we initially examine the consequence of this desynchronization through simulation and further verify it in the experimental setup.

In the simulations, the impact of the low-frequency excitation field phase was investigated by varying the phase of the B_2 field from 0 to 350° while the phase of the high-frequency excitation field (B_1) and the demodulation phase was kept constant at 0°. To investigate the effect of the high-frequency excitation phase on the measurement signal, the B_2 phase was varied in the same range while the two others were kept constant at 0°.

An intuitive approach to tracking the changes and effects of these phase variations is to observe both the simulated and measured signals in a complex plane. The results of low-frequency phase variation on simulated signals are presented in Figure 61 in 4 individual graphs. Figure 61 a) to d) show the changes of $f_1 \pm f_2$, $f_1 \pm 2 \cdot f_2$, $f_1 \pm 3 \cdot f_2$, and $f_1 \pm 4 \cdot f_2$, respectively, in a complex plane while varying the phase of the low-frequency excitation field φ_2.

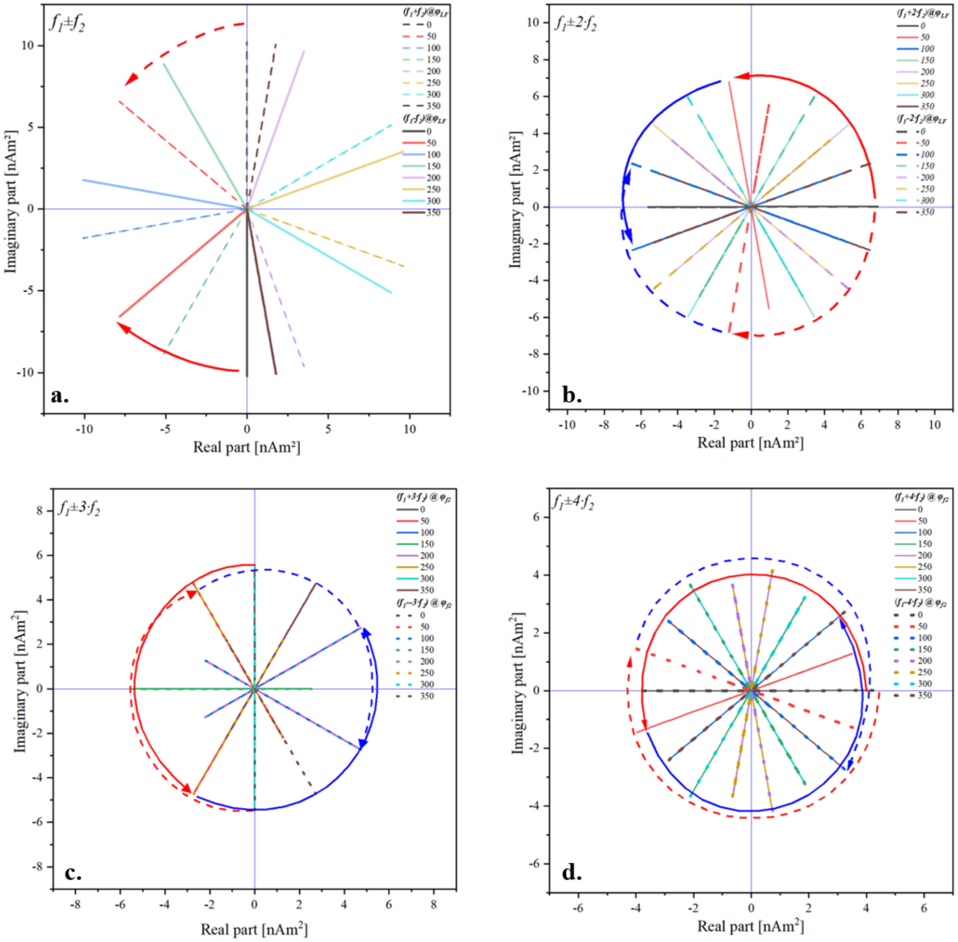

Figure 61. Effect of low-frequency excitation field phase variation on the symmetrical frequency mixing harmonics. depicted in a complex plane. a) $f_1 \pm f_2$, b) $f_1 \pm 2{\cdot}f_2$, c) $f_1 \pm 3{\cdot}f_2$ and d) $f_1 \pm 4{\cdot}f_2$.

The positive harmonics are plotted as solid lines, and the negative harmonics as dotted lines. We can see that the angle between the two symmetric mixing harmonic changes as a function of the low-frequency excitation phase.

For better understanding and visualization, the first two shifting stages of the mixing frequency harmonics in the presented plots are tracked with solid and dashed curved arrows, using red color for the first shift (0 to 50°) and blue color for the second shift (50 to 100°). In the case of the mixing harmonics $f_1 \pm f_2$, we observe that by increasing the φ_2 value, the angles between the two symmetric harmonics change from their initial value which was 180°. By tracking the transition, we see that in the first step where $\varphi_2 = 50°$, the transition causes an acute angle of 80° between the two harmonics. This transition is seen in figure a, as the black dashed line representing the $f_1 + f_2$ harmonic is rotated to its new position indicated by the red dashed line in the 2nd quadrant, and its trajectory is highlighted by the red dashed arrow. The transition of its counterpart f_1-f_2 can also be seen as the black solid line progresses to the red solid line in the 3rd quadrant. On the second transition, where $\varphi_2 = 100°$, we see that the f_1-f_2 harmonic moves to the 2nd quadrant, and the f_1+f_2 signal moves to the 3rd quadrant. The pattern follows as the φ_2 value increases. In a 360° variation of φ_2, each harmonic of $f_1 \pm f_2$ makes a full cycle and returns back to its initial position. The situation intensifies in the case of $f_1 \pm 2 \cdot f_2$. Initially, as depicted in Figure 60, both of the harmonics are superimposed on each other, and in Figure 61b, we can see that at the first step of the phase change they move away from each other and create an obtuse angle of 160°. This change is twice the value of the $f_1 \pm f_2$ component. By tracking the changes, we see that for variation of 360°, the mixing harmonics $f_1 \pm f_2$ make 2 complete cycles. In the case of $f_1 \pm 2 \cdot f_2$, the zero crossing can also be seen as the line passes through the origin of the graph. A similar pattern is also observable in the case of $f_1 \pm 3 \cdot f_2$ and $f_1 \pm 4 \cdot f_2$, moreover, they make 3 and 4 full cycles, respectively, upon 360° variation of the low-frequency phase φ_2.

A plot of the angle between the two symmetrical harmonics as a function of the φ_2 shift yields the triangular pattern depicted in Figure 62.

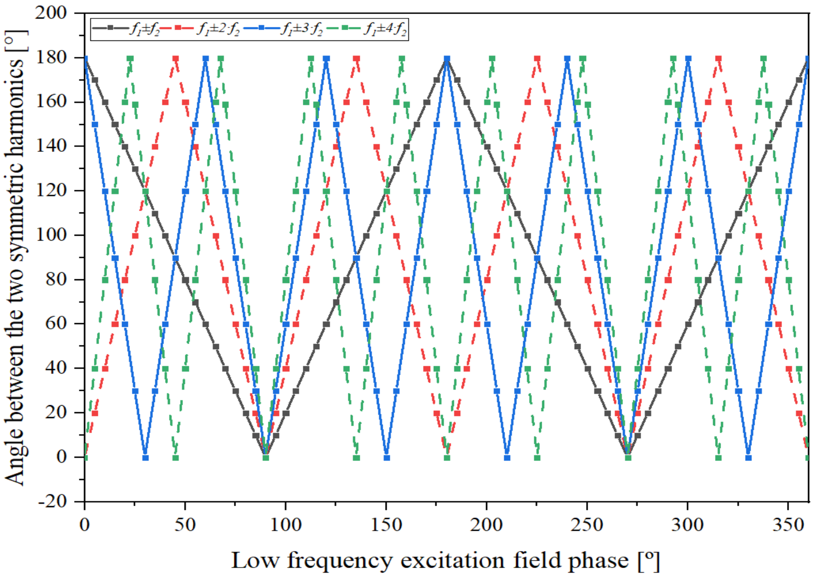

Figure 62. Angle between the two symmetrical harmonics plotted against the phase variation of the low-frequency excitation field for mixing harmonics $f_1 \pm f_2$ (black), $f_1 \pm 2 \cdot f_2$ (red), $f_1 \pm 3 \cdot f_2$ (blue), and $f_1 \pm 4 \cdot f_2$ (green)

In this figure, the angle between the two symmetrical harmonics is plotted against the phase of the low-frequency excitation signal (φ_2). The connecting lines are plotted to serve as a visual aid. The angle values are wrapped between 0 to 180 °. The angle between $f_1 \pm f_2$ is plotted in black, $f_1 \pm 2 \cdot f_2$ is plotted in red, $f_1 \pm 3 \cdot f_2$ is plotted in blue and $f_1 \pm 4 \cdot f_2$ is plotted in green. By analyzing the resultant pattern, we can see that the corresponding mixing frequency harmonics make 1, 2, 3, and 4 cycles around the complex plane upon the 360° phase variation correlating to the integer number n multiple of f_2 in $f_1 \pm n \cdot f_2$. Moreover, there are two points where all the mixing harmonics overlap each other and the angle between the two symmetric harmonics equals 0, that is when $\varphi_2 = 90$ or 270º. Identification and selection of these points would be favorable in the experimental measurements since the phase changes in all of the measured frequency mixing harmonics would start from the same reference point.

The next parameter in line is the impact of the high-frequency excitation field phase φ_1 on the demodulated frequency mixing signals. To assess this, the φ_1 parameter in the simulation was varied from 0 to 360° in steps of 50º while keeping the low-frequency excitation field phase and the demodulation phase constant at 0. The results of the simulation are depicted in Figure 63.

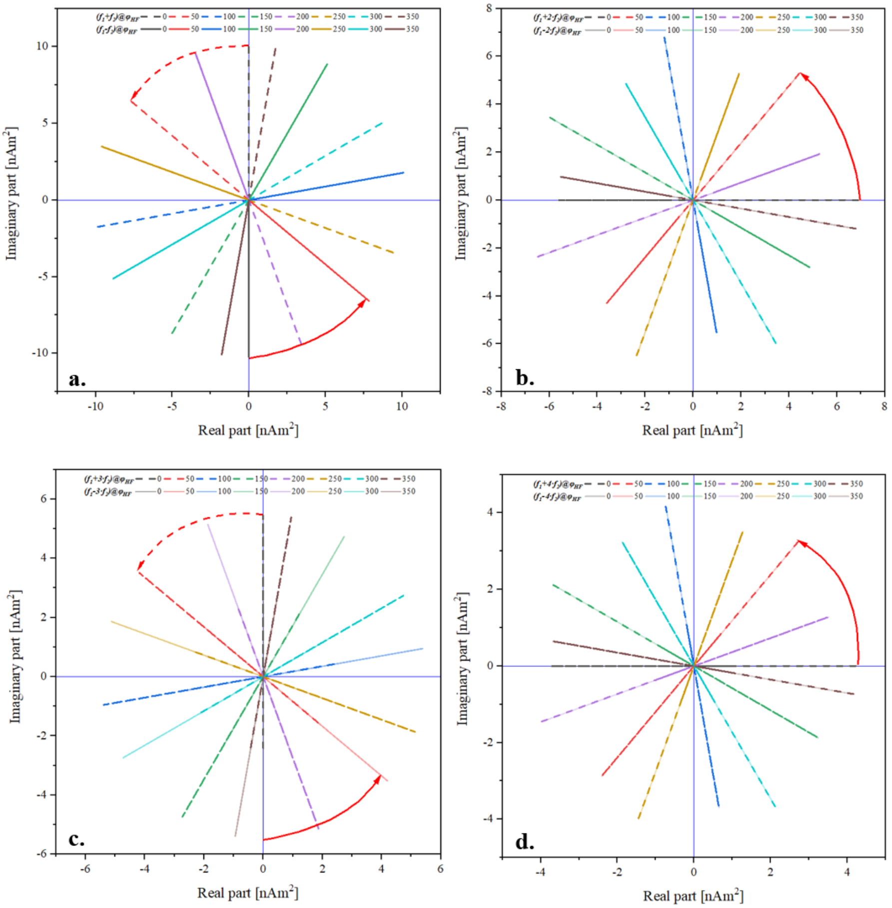

Figure 63. The variations of the mixing harmonics $f_1 \pm f_2$ to $f_1 \pm 4 \cdot f_2$ up on changing the phase of the high-frequency excitation field. a) $f_1 \pm f_2$, b) $f_1 \pm 2 \cdot f_2$, c) $f_1 \pm 3 \cdot f_2$ and d) $f_1 \pm 4 \cdot f_2$.

The variations of the mixing harmonics $f_1 \pm f_2$ to $f_1 \pm 4 \cdot f_2$ are shown in Figure 63 a to d. The positive harmonic is presented using a solid line type, and the negative harmonic with a dashed line type. The color, however, represents the different phases. Here we see that by varying the high-frequency excitation field phase φ_1, both symmetrical harmonics rotate in the complex plane, respectively, with the same angle of rotation, and the angle between the two components does not change. This is also true for changing the demodulation phase.

The change in the phase of the excitation signals directly impacts the synchronicity of the excitation fields. The simulations offer a better understanding of how the FMMD signals behave with respect to such synchronicity. Additionally, developments of the mentioned mixing harmonics through variation of the excitation magnetic field phases are shown in 3D graphs (Figure 64) for better understanding and visualization.

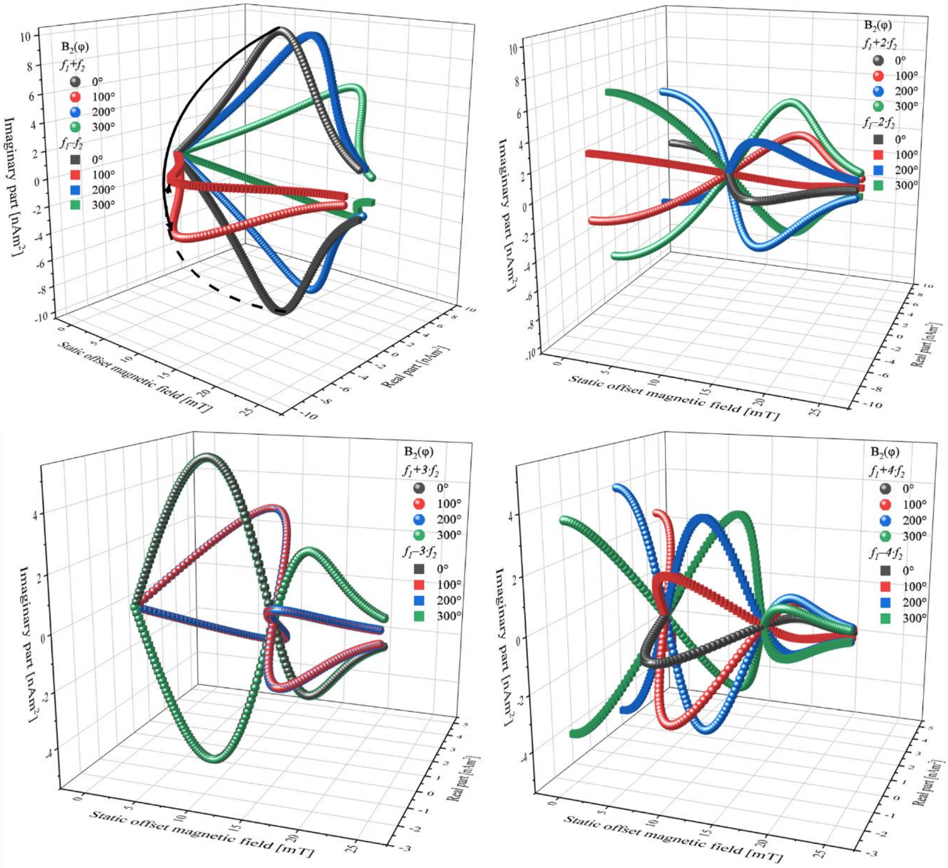

Figure 64. 3D visualization of the offset-dependent FMMD harmonics, with a variation of the phase of the excitation field B_2.

Moreover, considering the presented simulation results to measure the phase of the sample, characterization and calibration of the FMMD device with respect to the phases of the excitation signals are required. In the next section, initially, the experimental verification of the presented simulations will be given, furthermore, a phase characterization protocol is discussed to calibrate the measurement device.

6.3. Experimental verification and phase characterization of the excitation fields

The previous section highlighted the effects and the consequences of asynchronism between the excitation phases using numerical simulation and experimental verification of the effects. Moreover, the determination of the particle contribution to the measured phase of the FMMD signal is required. This section aims to measure and characterize the magnetic reader system with respect to the excitation and demodulation phase and to provide a calibration protocol.

As mentioned earlier in the instrumentation section, DDS chips are utilized as a source of excitation and demodulating reference signal generation.

To characterize the phase of the magnetic reader, the phase of the excitation signal needs to be evaluated at each stage of the excitation chain (generation, amplification and resulting magnetic field). Moreover, frequency-dependent phase shifts of the generated signals need to be also measured and evaluated.

The question is how to achieve synchronicity. The results of the asynchronism come from the fact that the phase of the excitation signals synthesized by the DDS chips is frequency-dependent. That means that when having two signals with frequencies apart from each other, the starting points of these two signals are different.

To evaluate this hypothesis, we look at the phase of the measured synthesized signal at varying frequencies while having a constant phase setting. The particular DDS we used has a 12-bit phase register. The phase can be changed by uploading a so-called phase number from (0 to 4095). The signal phase shift is then given by

$$\frac{2\,\pi}{4096} \cdot PhaseNumber \qquad \text{Eq.48}$$

To assess the frequency-dependent phase shift of the DDS, the synthesized signal was recorded using the measurement card NI USB-6251. The frequency was swept from 60 to 41000 Hz. The synthesized signal can be tracked in the complex plane depicted in Figure 65 (a), and the frequency-dependent phase plot is depicted in (b). From the results, we can deduce that we have a linear frequency-dependent phase shift of 45° from the starting frequency of 62.967 Hz which is the driving component f_2 to the excitation frequency of 40.5 kHz. This implies that when using the frequencies far apart from each other, the starting points differ, hence resulting in an asynchronism. Thus, one has to consider these phase shifts when adjusting the phase of the generated fields. In our case, the magnetic reader will be operated only at pre-determined frequencies. Therefore, creating a lookup table/graph for selecting the appropriate phases is a convenient way. This table can be generated by setting the desired frequency and performing a so-called phase sweep by varying the PhaseNumber. The measurement was done for frequencies f_2 = 62.957 Hz and f_1 = 40.5 kHz by varying the PhaseNumber from 0 to 4050 in 81 steps, as presented in Figure 66. In the figure, the change in the signal is shown in the complex plane. We can see that by changing the phase of the signal the vector representation rotates in a counterclockwise (CCW) manner. In both cases, as expected, a circular pattern is obtained.

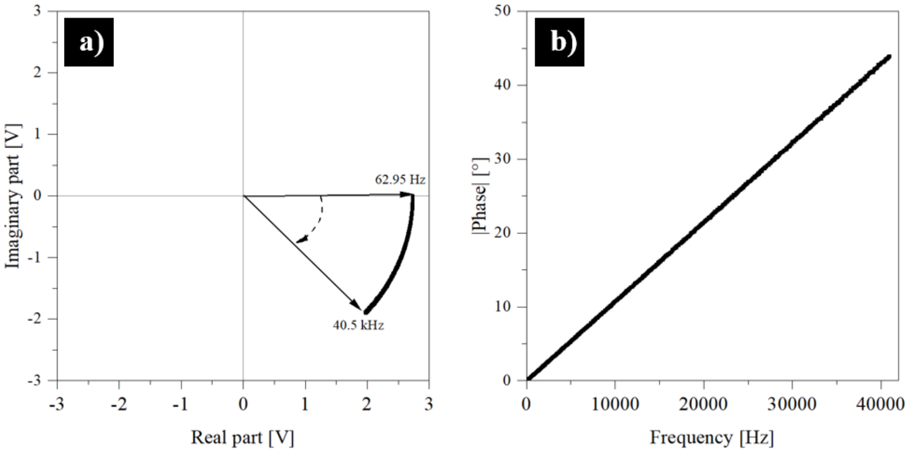

Figure 65 Frequency dependent phase shift of the synthesized signal using DDS chip plotted in the complex plane (A) and shown as a function of frequency in (B).

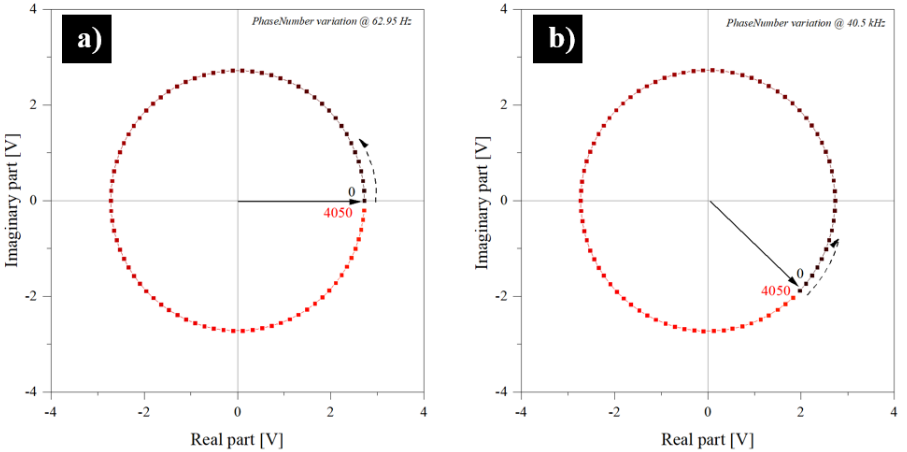

Figure 66. Phase sweep of each excitation signal a) Phase sweep at 62.0 Hz and b) Phase sweep at 40.5 kHz

In the next step, the signal after each stage in the excitation chain is recorded using the same method, while the phase number associated to the particular DDS source is varied. This is done to determine the status of the signal phase and its drifts after each stage. Finally, the most important part of the characterization is determining the phase of the generated magnetic field in the coils. The phase of the generated magnetic field follows the phase of the current. In the case of the low-frequency magnetic field (B_2), it is possible to determine the amplitude and phase of the field through measurement using a Hall sensor. But in the case of the high-frequency magnetic field (B_1), measurement with the Hall sensor is not possible because of its limited bandwidth, therefore the induction coil method is utilized in that case.

Faraday's law of induction states that the induced voltage in the coil has a 90° phase shift with respect to the magnetic field. Both components of the generated magnetic fields were measured using the test coil (introduced in 3.6). The phases of the excitation signals were varied as previously mentioned. Figure 67 shows the results of the measured induced voltages of the high-frequency field (V_1) and of the low-frequency magnetic field (V_2). The phase variation of the induced voltage (V_1) is depicted as a gradient color pallet, starting from black solid squares at PhaseNumber 0, progressing in the CCW direction, and ending with red solid squares at phase number 4000. The measurements of induced voltage V_2 at the low-frequency magnetic field have been magnified 30-fold to be in the same range as V_1 for better visualization and comparison. It has been depicted using solid circles, and the progress of the phase rotation is shown in a color gradient from black to green, starting from PhaseNumber 0 given in black color to phase number 4000 shown in green. The starting points for both V_1 and V_2 are shown using black arrows. The 90° shift representing the magnetic fields is calculated and shown using cross marks and dashed arrows with respective red and blue colors for B_1 and B_2 fields.

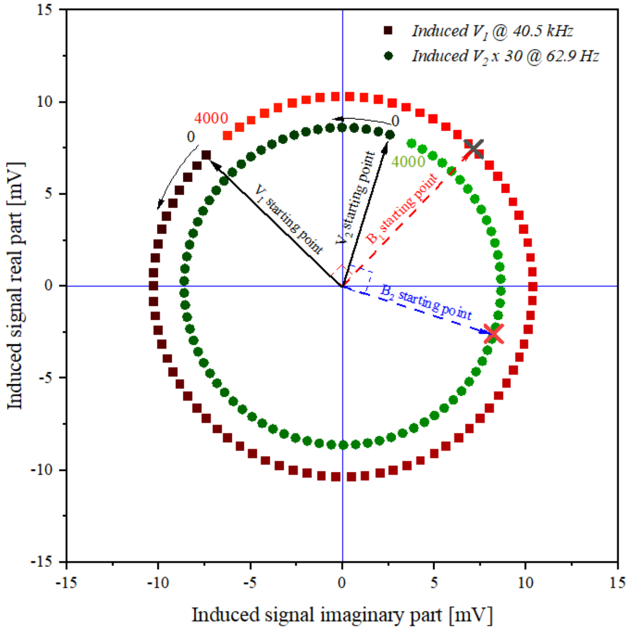

Figure 67. Look-up graph of the phase sweeps for determination of the Excitation field's phases.

Here we see that the starting point of the low-frequency excitation DDS signal at 62.957 Hz has an angle of 343 ° (-17°) and the starting point of the high frequency at 40.5 kHz has an angle of 46 °. We have to set the phase number of each DDS so that both of them are aligned parallel to each other. From the graph, we can select the Phase number combination which makes this possible. In this case, for the low-frequency signal, PhaseNumber 200, and for the high-frequency signal, PhaseNumber 2300 was selected.

Another contribution to the measured phase is the phase of the detection chain. In case of the digital demodulation, it includes the phase of the detection coil and pre-amplification stage. The frequency-dependent phase of the detection coil and the pre-amplifiers was evaluated using a synthetic signal generated by the Lock-in amplifier SR830 from Stanford Research and supplied using the test coil. The test coil was placed inside the measurement head while both excitation fields were switched off. The frequency of the signal was varied from 11 to 65 kHz. The amplitude and the phase response of the detection module are presented in Figure 68. In the figure, the amplitude response is depicted in black, and the phase response is depicted in red. The resonance peak is due to the capacitance in parallel to the detection coil, and the corresponding phase shift is seen. The current working range with the fixed high-frequency excitation has been highlighted using the thick green line.

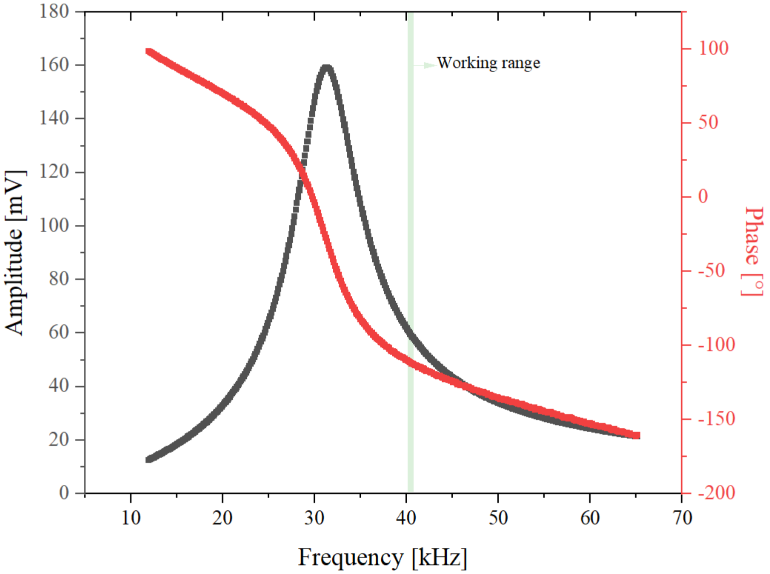

Figure 68. Frequency-dependent phase and amplitude response of the detection coil

As per the characterization results of the excitation and detection chain of the system, one has to choose proper phase settings for the excitation fields. In the previous section, it was shown using numerical simulations that a variation of the phase of the low-frequency excitation field (B_2) will change the angle between the two symmetric harmonics, whereas a variation of the phase of the high-excitation field (B_1) or of the demodulation phase only rotates all the harmonics in the complex plane.

In the next step, the experimental verification of the effects predicted by the simulation will be presented.

The static offset magnetic field-dependent FMMD signals were measured for variation of the phase of B_2. Figure 69 A and B show the experimental measurements for the first two mixing frequency harmonics $f_1 \pm f_2$ and $f_1 \pm 2 \cdot f_2$ in a 3D plot complex plane with a varying magnetic field. The positive components have been depicted as solid cubes, and the negative components as spheres. The PhaseNumber variation is shown as gradient color and transparency change. By tracking the PhaseNumbers, starting at 0 with pale red spheres and cubes, and moving on to phase number 400 equivalent to ~35°, we observe that the two symmetrical harmonics rotate, and the angle between them reduces.

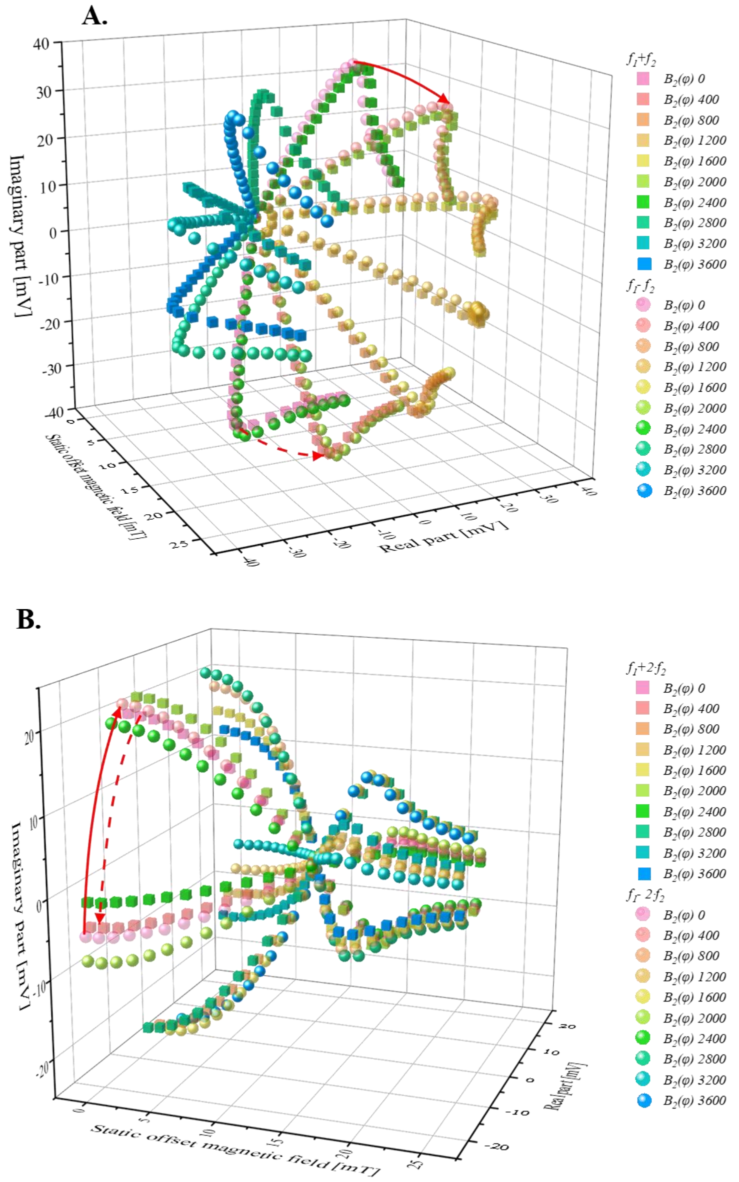

Figure 69. Experimental recordings of the first two mixing frequency harmonics A) $f_1 \pm f_2$ and B) $f_1 \pm 2{\cdot}f_2$ in 3D complex plane plot with varying magnetic field for the varying phase of the B_2 (low-frequency) field.

In $f_1 \pm f_2$ we obtain one full cycle by varying the $B_2(\varphi)$ from 0 to 360° and in the case of $f_1 \pm 2{\cdot}f_2$, two full cycles are obtained. The variation of the angles between the harmonics deduced through the experimental results for the first four symmetrical mixing harmonics has been overlaid on the theoretical values presented earlier, and plotted in Figure 70. The angles are wrapped to show the variation between 0 and 180°. This validates the relationship between the variation of the $B_2(\varphi)$ and the angle between the two symmetric harmonics. Furthermore, it can be seen in the graph that there are two locations where the angle between the harmonics is minimum, meaning that both harmonics overlap. The locations are highlighted using green rectangles. This means that if one selects either one of these two locations with such a setting of $B_1(\varphi)$, the harmonics are projected onto the real axis of the complex plane for a reference sample that exhibits no additional phase shift. With that setting, the measured phase change of other samples could be directly taken as a measure for their sample-induced phase shift. This will reduce signal post-processing steps.

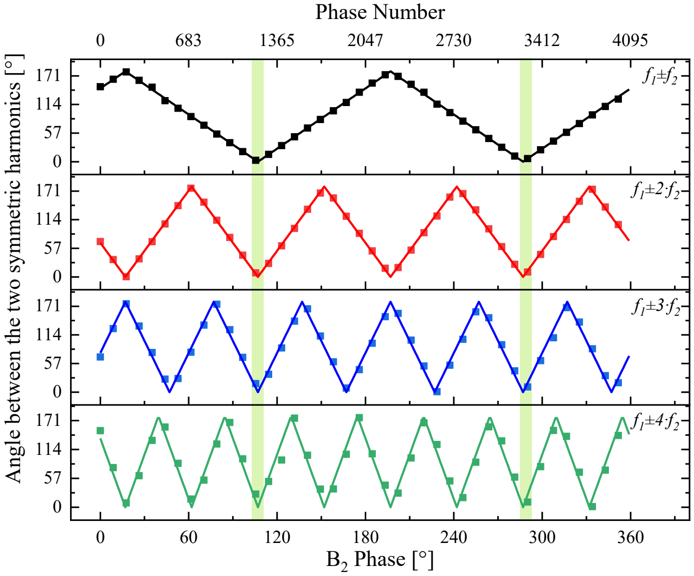

Figure 70. Overlap of the angle between the harmonics obtained from the experimental measurements (symbols) and the simulation (solid lines).

The offset scan measurements performed with two different phase settings are shown in Figure 71. The plot in (a) shows the results of having the phase settings in such a way that the excitation fields are synchronous. We can see the alignment of the harmonics, as predicted by the simulation. The odd harmonics have an angle of close to 180° between each other and the even harmonics are overlapping with each other. Each harmonic has a 90° angle with the next one, which is described by sin and cos functions according to the basic FMMD equations. On the other hand, (b) shows the results with phase settings chosen as (B_1: 3200 and B_2: 3285). We can see that all the harmonics are rotated in such a way that they have been projected on the real axis. The angle between the harmonics has been minimized. As mentioned earlier, the advantage of this setting is that we can use the background-subtracted intensity of the real part of the measured harmonics as the nonlinear amplitude response of the measured sample containing the MNPs. The phase response can be calculated, and the phase shift of different particles with respect to a selected reference particle can also be deduced and analyzed.

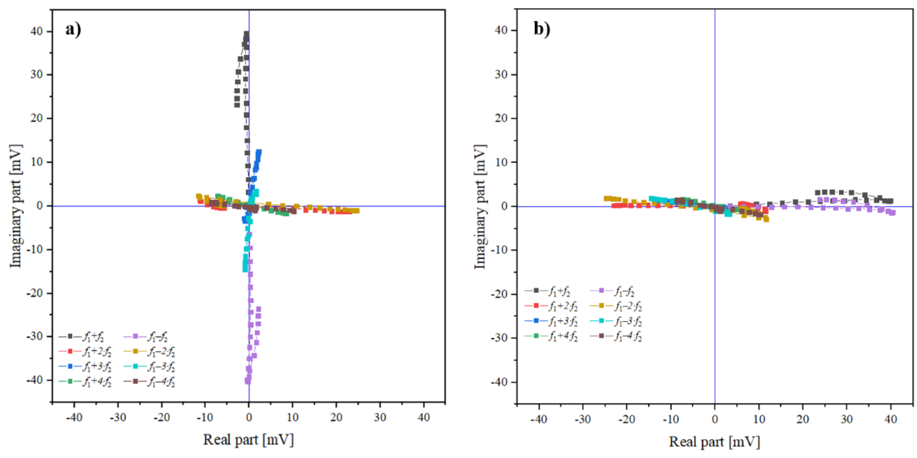

Figure 71. Measurement of Syn70 sample using two phase settings for the B_2 excitation field. In a) the fields are synchronous and in b), the phase setting is selected in such a way that the harmonics have the smallest angle between each other.

Chapter 7

7. Multiplex detection of MNP using offset-dependent FMMD signal

In the last decade, there has been a growing interest in the field of multiplex detection, which is the ability to detect more than one analyte within a single sample. This is helpful for example in the case of magnetic immunosensing [62] or even magnetic particle imaging [113]. The consequence of multiplex detection is that reduced amounts of samples and reagents are needed, leading to lower financial expenditures. Different approaches have been reported in the literature, for example, lateral flow biosensors were used for multiple analyte detection through fluorescent and colorimetric methods for the detection of viruses [15], bacteria [16], and antibodies [17]. In [114], a magnetic relaxation switch approach was used for the detection of multiple analytes. Moreover, multiplex detection of proteins was performed using GMR sensors [35].

Furthermore, susceptibility-based measurement techniques have also been able to simultaneously detect different magnetic nanoparticles and beads. For example, the simultaneous detection of small-size particles was completed using the AC susceptometry technique [115–117]. On the other hand, the frequency mixing magnetic detection approach has also yielded promising results in terms of multiplex detection; for instance, it was shown that multiplex detection can be performed by spatial separation using 3D-printed modular immunofiltration columns [52]. Using the amplitude and the phase of the mixing harmonics, one can differentiate among different types of magnetic beads [51,118–120]. These publications emphasize the fact that the phase response of the magnetic nanoparticles is type-specific and can be utilized for multiplex detection.

According to Lenglet [121] different types of magnetic particles can be distinguished based on the offset field dependence of their frequency mixing responses. This method has been demonstrated to be applicable for multiparametric detection [122]. The mixing ratio of two types of magnetic particles with different hydrodynamic diameters has been determined from the ratio of the fifth to third harmonic response amplitude [115]. The differentiation is based on the particles' different structural magnetic properties [123]. Another approach to particle distinction is based on their differences in Brownian relaxation times, which enables discrimination based on two-frequency measurements [124] or multichannel image reconstruction [125,126].

The impact of varying MNP core size on the static offset field-dependent FMMD signals was addressed in earlier chapters. This is beneficial for multiplex detection, since for example two or three bead types with different core size distributions can be identified through this technique. In this chapter, we will investigate and report on the further developments on the possibility of identification of different bead types, initially within a binary particle mixture, and then a ternary particle mixture. Our approach utilizes a static magnetic offset field, and we present a novel technique for calculating the percentages of the constituents.

The chapter is partly based on the original publication by the author [106].

7.1. Used Magnetic beads

In this study, we have used several types of commercial magnetic beads ranging from 50 nm to 1 µm hydrodynamic diameter, procured from micromod Partikeltechnologie GmbH, Rostock Germany. The selected beads for this experiment are listed in Table 12. The mentioned parameters and surface functionalization have been taken from the datasheet provided by the manufacturer.

Table 12 List of the MNPs used in the experiments

Type	Hydrodynamic size d_H [nm]	Stock concentration [mg/mL]	Surface
SynomagD	50	25	Dextran
SynomagD	70	5	Streptavidin
Perimag	130	5	Streptavidin
NanomagCLD	300	10	Streptavidin
Nanomag CLD/SynomagD	1000	10	Streptavidin
SynomagD	1000	10	Streptavidin

7.2. Instrumentation and measurement procedure.

The mixture samples were measured by the stable tabletop static offset magnetic field FMMD setup described in section 3.4.1 and shown in Figure 30. The measurement device was warmed up until the temperature and the measurement signal were stabilized. The scanning procedure then commenced in an automatized fashion. Initially, the background signal was measured for three and a half minutes while the sample was kept outside the measurement head. Then the sample was placed into the measurement position using the servo, as explained in the experimental setup section. The sample was measured for three and a half minutes and then pushed out. The static magnetic offset field was then changed to the next value and the same procedure was repeated until the final step of the magnetic field strength was reached. Post-processing of the measured data was done using the procedure explained in (Chapter 5).

7.3. Quadratic programming optimization

Finding the linear combination of single particle reference measurements that minimizes the quadratic deviation to the mixture measurement allows for the determination of the contributing amount of beads in a two-bead mixture measurement. (For a binary mixture, the individual measurements Ref_A and Ref_B of both particle types A and B are multiplied with coefficients x_A and x_B and added. The set of coefficients that minimizes the quadratic deviation between the mixture measurement and the approximation $x_A \cdot Ref_A + x_B \cdot Ref_B$ is determined.) Therefore, the magnetic beads' nonlinear magnetic moment response to a varying static offset magnetic field is utilized for this.
The particle type that was measured is represented by the index i. The measured reference signal values, are referred to as $Ref_{i,j}$, and the static magnetic offset field B_j at which measurement data M_j are being obtained is represented by the index j in these values. It turns out that using data from all of the first four mixing frequency harmonics at the same time, $f_1 + n \cdot f_2$ (n = 1, 2, 3, 4), improves the parameter estimation greatly, compared to using data from just one harmonic. The index j enumerates through all measurement data points. In our example, it simply stretches progressively over the four frequency mixing harmonics, counting along the B_0-axis of $f_1 + f_2$, then along the B_0-axis of $f_1 + 2 \cdot f_2$, and finally ending at the maximum field value of $f_1 + 4 \cdot f_2$.

To simplify the approach, we can assume to disregard the particle-particle interaction when relatively small concentrations of MNPs are in solution [30,127]. Assuming that each particle contributes independently to the total observed signal, the total signal may therefore be calculated as a linear combination of the signals of all the particles in the sample. Consequently, a weighted sum can be used to represent the whole reference measured signal Ref_j at a static field value B_j.

$$Ref_j = \sum_i x_i \cdot Ref_{i,j} \qquad \text{Eq.49}$$

The sum is over the reference signals of different particles type i with weights x_i. The amounts of x_i from type i particles are the unknowns to be calculated, representing the contribution of each particle type to the overall signal.

The sum S of the square residuals between the measurement and the reference should be reduced for the optimization phase. i.e.

$$S = \sum_j \left[M_j - \left(\sum_i x_i \cdot Ref_{i,j} \right) \right]^2 \rightarrow min. \qquad \text{Eq.50}$$

The following quadratic form can be minimized by multiplying out S:

$$S = \sum_j \left(\sum_i x_i \cdot Ref_{i,j} \right) \cdot \left(\sum_k x_k \cdot Ref_{k,j} \right) - 2 \cdot \sum_j M_j \cdot \left(\sum_i x_i \cdot Ref_{i,j} \right) + \sum_j M_j^2 \rightarrow min. \qquad \text{Eq.51}$$

This can be rewritten in the standard form used in so-called quadratic programming (QP) [43],

$$S = 2\left(\frac{1}{2}\,\vec{x}^T \cdot Q \cdot \vec{x} + \vec{c}^T \cdot \vec{x}\right) + \sum_j M_j^2 \rightarrow min. \qquad \text{Eq.52}$$

with a symmetric $n \times n$, positive definite matrix Q (n is the number of reference measurement curves, enumerated by index $i = 1, \dots ,n$)

$$Q = \begin{bmatrix} \sum_j Ref_{1,j}^2 & \sum_j Ref_{1,j} \cdot Ref_{2,j} & \cdots & \sum_j Ref_{1,j} \cdot Ref_{n,j} \\ \sum_j Ref_{1,j} \cdot Ref_{2,j} & \sum_j Ref_{2,j}^2 & \cdots & \sum_j Ref_{2,j} \cdot Ref_{n,j} \\ \dots & \dots & \dots & \dots \\ \sum_j Ref_{1,j} \cdot Ref_{n,j} & \sum_j Ref_{2,j} \cdot Ref_{n,j} & \cdots & \sum_j Ref_{n,j}^2 \end{bmatrix}. \qquad \text{Eq.53}$$

and an n-dimensional vector

$$\vec{c}^T = \left[-\sum_j M_j \cdot Ref_{1,j} \quad -\sum_j M_j \cdot Ref_{2,j} \quad \cdots \quad -\sum_j M_j \cdot Ref_{n,j} \right]. \qquad \text{Eq.54}$$

Equation (52)'s parenthesized term is expressed in the QP's standard form, which is for a quadratic optimization problem with linear constraints. For typical QP algorithms, the matrix Q and vector c of equations (53) and (54) can be utilized directly as input parameters. We carried out the optimization numerically using what is known as the active set algorithm [128].

7.4. Sample preparation

Since this study is directed towards the behavior of magnetic beads, we abstained from the use of any biological capturing entity, as it is typically used in magnetic immunoassays. Hence, the samples involved in this study were prepared using the sample preparation strategies introduced in chapter 4, namely liquid suspension preparation and immobilization on the Abicap filter.

In the case of the binary mixture samples, mixtures of two different bead types were prepared with volume ratios of 0%: 100%, 25%: 75%, 50%: 50%, 75%: 25% and 100%:0%, always maintaining a total of 10 µL of bead solution, diluted in 100 µL of distilled water.

7.5. Binary mixture (Duplex)

Utilizing signatures of the beads on the mixing frequency features, five samples were prepared using two types of beads. The bead types selected for this experiment are 1 µm Nanomag/SynomagCLD, henceforth named A, and 1 µm SynomagD, named B. They are good candidates since they exhibit features that are much apart from each other. They are also quite intriguing because they have the same hydrodynamic diameter. The particle A and B reference samples were labeled A and B, respectively, and the combination samples were labeled Mix1 to Mix3, the contents of which are shown in Table 13.

Table 13 . Amount of the bead types used for the preparation of the reference samples (A and B) and the mixture samples Mix1 to Mix3. Bead type A resembles 1 µm Nanomag/SynomagCLD, and bead type B resembles 1 µm SynomagD.

		Mixture Samples				
		A [µL]	Mix1 [µL]	Mix2 [µL]	Mix3 [µL]	B [µL]
Bead Type	A	10	7.5	5	2.5	0
	B	0	2.5	5	7.5	10

The traces of the nonlinear magnetic moment response of the binary mixture samples and the reference samples are shown in Figure 72. The dominance of bead type B, which has a stronger response and thus a higher amplitude, is also seen in the prevalence of feature sites. The QP algorithm was used to determine the contributions from measurements of the mixture samples. The optimization results are also shown in Figure 72.

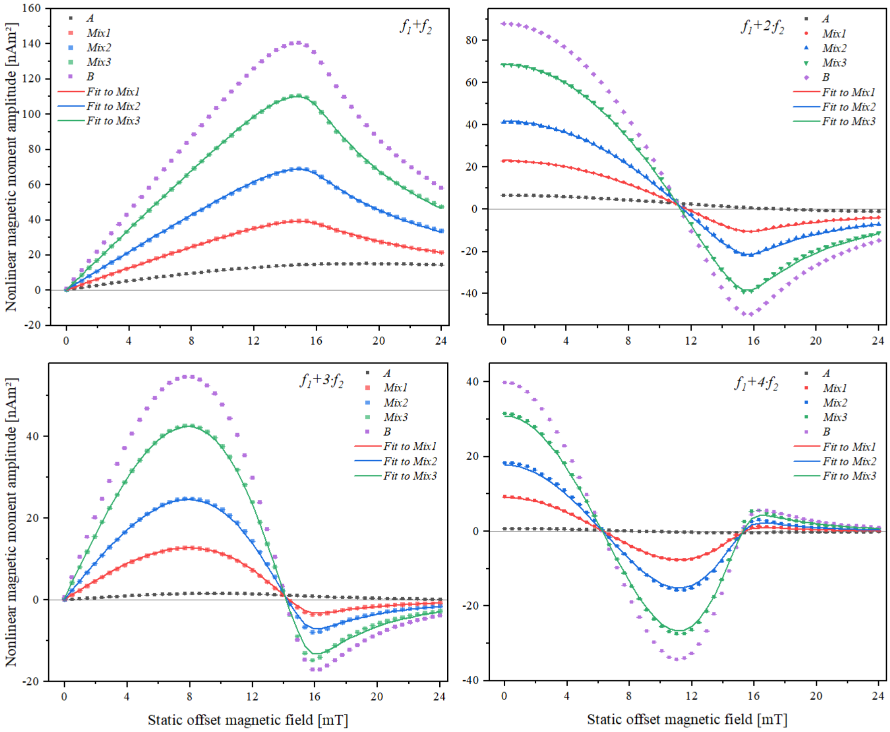

Figure 72. Nonlinear magnetic moment traces (mean and standard deviation within point size) of samples made from a mixture of two different types of magnetic beads over and static magnetic offset field range of 0 to 24 mT, for mixing frequencies $f_1 + f_2$, $f_1 + 2\cdot f_2$, $f_1 + 3\cdot f_2$ and $f_1 + 4\cdot f_2$. A and B represent the sample containing pure bead A and pure bead B, respectively. Samples Mix1 to Mix3 contain different ratios of the two beads, they have been analyzed using the QP algorithm for the determination of the contributions.

Contributions of each pure sample (A and B) to the signal obtained from the mixed samples were then calculated using the quadratic programming approach interpolation mentioned in section 8.3. The results are given in form of a percentage of the reference measurements in a bar chart representation in Figure 73 together with the expected ratios.

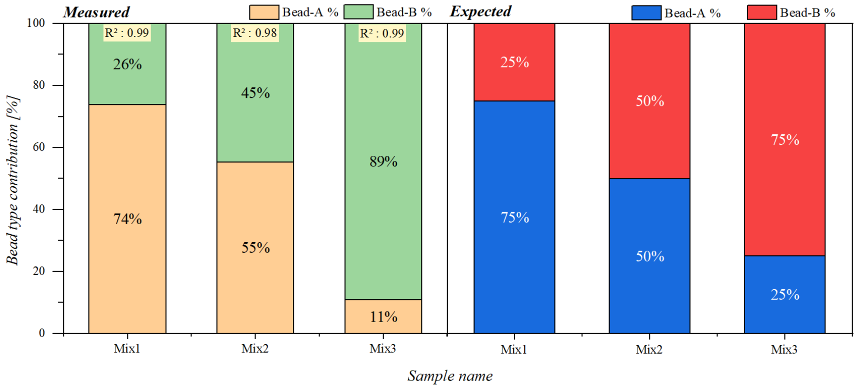

Figure 73. Bead type contributions for mixture samples containing beads A and B. The left chart presents the determined percentage of contributions from each reference bead type to the measured mixed samples. The right chart presents the expected contribution percentages of each bead type to the mixed samples.

We can see that although the amplitudes of the two reference measurements (A and B) are very much apart from each other, the calculated contributions do follow the prepared ratio patterns with a minimum deviation of 1% in the case of Mix1 and a maximum deviation of 14% in case of Mix3.

To further investigate the effect of magnetic response in the mixture samples which also have been reported in [30] with respect to the phase of the frequency mixing signal, the particle type yielding a stronger response can be diluted. The amplitude was adjusted by diluting the 1 m SynomagD (B) bead solution to 7% of its original concentration, which resulted in a lower amplitude response. A new set of samples were prepared using the same ratios expressed in Table 13, but with diluted stock. The samples containing pure bead type were labeled as A* and B* and the mixture samples were labeled as Mix1*, Mix2* and Mix3*, respectively.

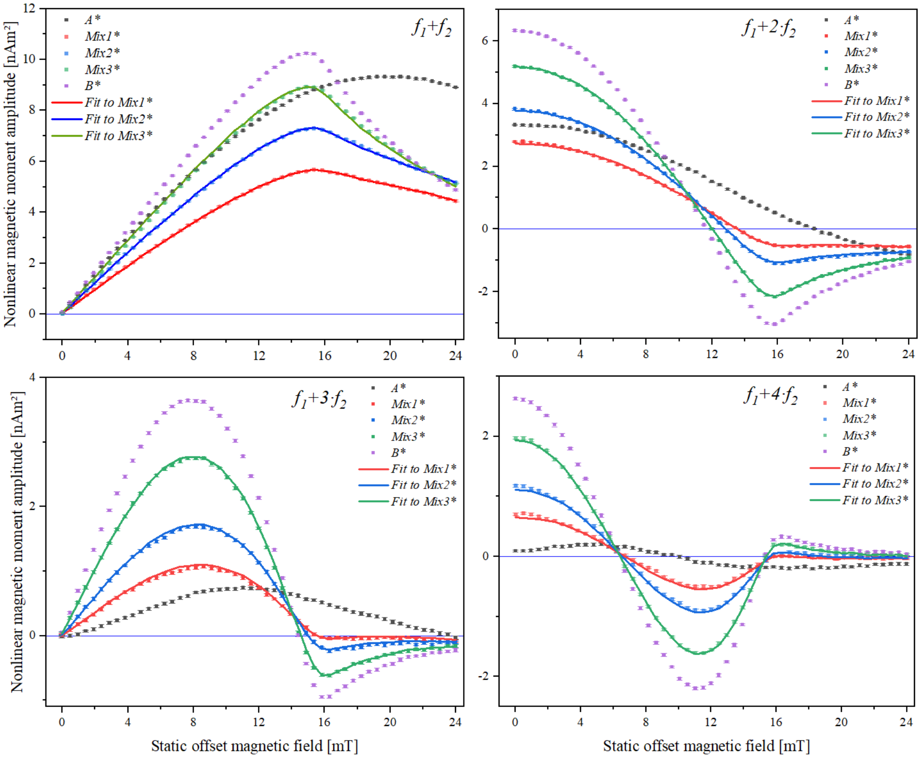

Figure 74. Nonlinear magnetic moment trace (mean and standard deviation within point size) of samples made from a mixture of two different types 1µm Nanomag/SynomagCLD (A) and 1 µm SynomagD (B*) diluted to 7% of its original concentration. The responses of the mixture samples of the two bead types (Mix1* to Mix3*), prepared according to the ratios specified in Table 13, at mixing frequencies $f_1 + f_2$, $f_1 + 2{\cdot}f_2$, $f_1 + 3{\cdot}f_2$ and $f_1 + 4{\cdot}f_2$ were recorded over a static magnetic offset field range from 0 to 24 mT. The response of the mixture samples have been analyzed using the QP algorithm for the determination of the contributions.*

Figure 74 shows the magnetic field scan of the diluted set. When investigating the features of the mixing frequency signals, we can see that although bead type B* is still highly affecting the location of the features, they become distinguishable due to the reduced strength of the signal from particle B. The locations of the features were determined using a quadratic fit for minima and maxima and a linear fit for the zero-crossings. The results are listed in Table 14.

By looking at the maxima of the mixing frequency signal $f_1 + f_2$ for the two reference samples, we observe a deviation of 5.19 mT, and looking at mixture samples, we can see that Mix3* which contains more amount of B* bead type has its feature occurring closer to that of B*. Furthermore, looking at the features of $f_1 + 2{\cdot}f_2$, in the case of sample A*, the zero-crossing occurs at 18.73 mT and has a deviation of 6.59 mT from B*. However, the minima of A* stays undetermined since it occurs at higher magnetic fields beyond our scan range. Comparing the two reference samples A* and B*, we see that their features occur within a relative standard deviation of at least 21.23% in the case of $f_1 + f_2$ maxima and at most 36.38% in the case of $f_1 + 4{\cdot}f_2$ 1st zero-crossing. However, there are some regions where the feature remains undetermined because of the limited static magnetic offset field scan range. On the other hand, if we look at the feature separation between the sample Mix3* and B*, we observe that the deviation gap is closing in such a way that we observe the maximum deviation of the 1st zero-crossing of $f_1 + 4{\cdot}f_2$ and minimum deviation on 2nd zero crossing of the same harmonic.

Table 14. Location of the characteristic features of samples reference samples A and B* and the mixture samples Mix-1* to Mix-3*, some of the parameters remain undetermined due to limited achievable static magnetic field, they are marked with "--".*

Mixing term	Bead sample	A*	Mix1*	Mix2*	Mix3*	B*
$f_1 + f_2$	Maximum [mT]	19.87	15.60	15.22	14.92	14.68
$f_1 + 2{\cdot}f_2$	Zero [mT]	18.73	14.03	13.30	12.48	12.15
	Minimum [mT]	--	17.47	16.99	16.29	16.21
$f_1 + 3{\cdot}f_2$	Maximum [mT]	11.02	8.27	8.10	7.79	7.78
	Zero [mT]	23.65	15.59	15.10	14.49	14.40
	Minimum [mT]	--	--	16.55	16.18	16.17
$f_1 + 4{\cdot}f_2$	1st Zero [mT]	9.82	6.86	6.57	6.42	5.76
	Minimum [mT]	17.39	11.47	11.43	11.20	11.18
	2nd Zero [mT]	--	15.78	15.69	15.40	16.38
	Maximum [mT]	--	--	17.05	16.38	16.57

The interpolation results in the case of these set of samples can be seen in Figure 75. They do follow the expected pattern upon which the samples were prepared, but with a maximum deviation of 13.4% in Mix1* sample.

The deviation occurring in both diluted and undiluted mixture series can be due to the reason that the bead type 1 µm SynomagD (B and B*) is dominating in the measured signals.

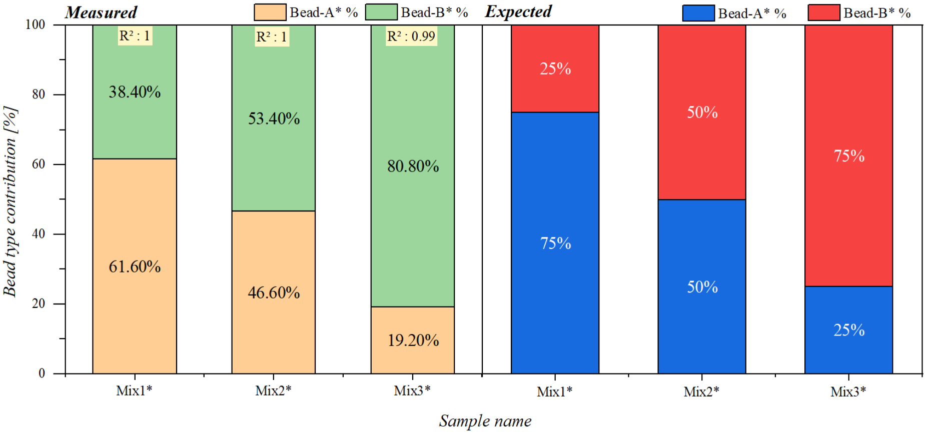

Figure 75. Bead type contributions for mixture samples containing beads A and B*. The left chart presents the determined percentage of contributions from each reference bead type to the measured mixed samples. The right chart presents the expected contribution percentages of each bead type to the mixed samples.*

7.6. Ternary mixture

After a successful analysis of the binary mixture of two different constituents, the next step is to try mixtures of three different types of particles at different mixing ratios. For this case of ternary mixtures, particle types Nanomag CLD 1 µm, Nanomag D Spio 20 nm and Perimag 130 nm according to Table 15 were used with volume ratios of 0%:0%:100%, 0%:100%:0%, 100%:0%:0% as reference samples and 25%:25%:50%, 25%:50%:25%, 50%:25%:25% as mixture samples, always maintaining the total of 10µL of bead dilution, diluted in 150 µL of distilled water.

All the ternary mixtures were measured in a liquid state.

The same approach as for the binary mixture determination was used. The trace of the nonlinear magnetic moment response of the ternary mixture samples and the respective reference samples are given in the appendix (5). The determination results for the ternary particle mixture set can be seen in Figure 76. They do follow the expected pattern upon which the samples were prepared, however, in this case, we can see that the deviations in mixtures 1 and 3 are below 10 % but the deviation from expectation in the case of mixture two is greater than 10 %. The argument of dominating signal as observed previously is again valid.

Table 15. Location of the characteristic features of samples reference samples A, B and C in used in ternary mixture samples and the mixture samples Mix 1 to Mix-3, some of the parameters remain undetermined due to limited achievable static magnetic field, they are marked with "--".

Mixing term	**Bead sample**	**A**	**B**	**C**	**Mix1***	**Mix2***	**Mix3***
$f_1 + f_2$	Maximum [mT]	19.87	14.39	14.94	14.97	14.74	14.43
$f_1 + 2 \cdot f_2$	Zero [mT]	18.73	11.13	10.79	11.10	10.91	10.94
	Minimum [mT]	--	16.12	15.75	15.71	15.64	15.41
$f_1 + 3 \cdot f_2$	Maximum [mT]	11.02	7.76	7.91	8.02	8.02	7.95
	Zero [mT]	23.65	14.50	13.65	13.82	13.68	13.65
	Minimum [mT]	--	17.31	16.25	16.20	16.24	16.05
$f_1 + 4 \cdot f_2$	1st Zero [mT]	9.82	6.21	6.08	6.15	6.14	6.12
	Minimum [mT]	17.39	11.09	11.15	11.20	11.09	10.97
	2nd Zero [mT]	--	16.13	14.97	15.01	14.95	14.92
	Maximum [mT]	--	18.43	16.66	16.63	16.62	16.59

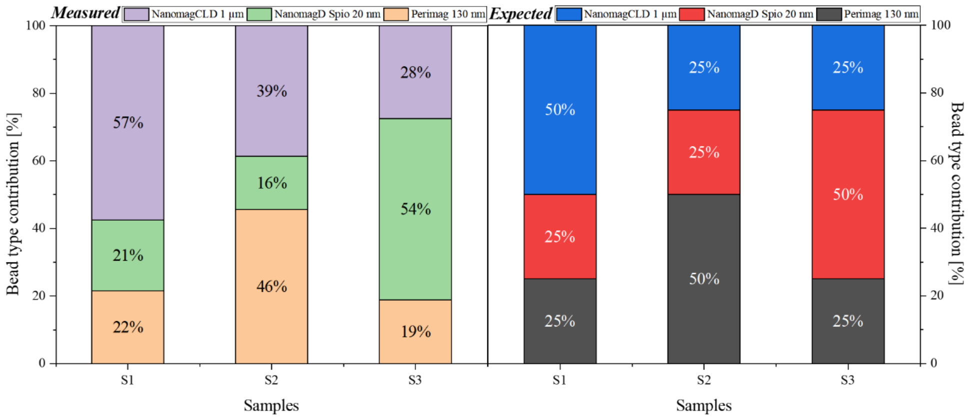

Figure 76. Bead type contributions for mixture samples containing three bead types. The left chart presents the determined percentage of contributions from each reference bead type to the measured mixed samples. The right chart presents the expected contribution percentages of each bead type to the mixed samples

7.7. Conclusion and outlook

Characterization of different types of magnetic beads by means of frequency mixing magnetic detection using a static magnetic offset scanning technique reveals that the locations of features occurring in the frequency mixing signals, i.e. the extremes and zeros of different frequency mixing components, vary depending on the type of magnetic beads. Furthermore, it has been shown that the location of these features is independent of the amount of magnetic beads in the sample, which makes them good type identifiers. By investigating the effect of mixing two bead types in a sample, it can be seen that the features deviate proportionally to the ratio of bead types. Utilizing the information from these features together with the amplitude response of the beads which is used for quantification, the amount of each bead type in a sample can be determined. A simple straightforward approach is quadratic programming optimization to determine the best linear combination of the measured responses of the two reference beads. The estimated contributions were assessed and presented for both non-diluted and diluted mixture samples. The results show a reasonable agreement to the initially prepared dilution with a maximum deviation of 14%. In the case of the ternary mixtures, by looking at the determined results we can see that the trend agrees to that of the expectation. However, a larger error on the determination of S2 sample is observed. Further optimization through assessment of different preparation methods has to be taken. Moreover, this approach is based upon the assumption that the bead types are not interacting with each other, and that mixtures yield a response that is a linear combination of the signals of each particle type. This assumption might not be true for very densely packed systems which might require a more complex model.

Chapter 8

8. Magnetic nanoparticles core size determination with FMMD technique

Determination of the core size and analysis of the morphology of the MNPs is routinely performed with TEM imaging technique [53,54]. With this method, one can measure the core diameter (d_c) of a few hundred to a thousand particles to obtain a discrete core size distribution [53]. As the edges of the particle core usually appear blurry in the TEM image, the choice of the threshold in automatized image processing can remarkably influence the resulting core size distribution. In addition, TEM requires costly instrumentation and a complex and destructive sample preparation technique while yielding only local information on the 2D projection of the particles [53,55].

When performing the core size distribution analysis using TEM, only a small portion of particles is routinely investigated; hence the technique provides a limited value for the size distribution of an entire sample. However, for most of the applications mentioned above, large ensembles of MNPs are employed, containing billions of particles ($\sim 10^{12} \frac{1}{mL}$). It has been shown that susceptibility measurement techniques constitute a promising tool for obtaining information on the core size distribution of the particles in a larger volume [55,129] than is usually used in TEM. Furthermore, the average (magnetic) core size can also be derived for the entire ensemble of MNPs from the magnetization curve using Chantrell fitting [95] or from XRD analysis using the Scherrer method [130].

The Frequency Mixing Magnetic Detection (FMMD) method can also be used for the analysis of the core size distribution of a larger volume of magnetic nanoparticles [127]. Furthermore, in Ref. [127] it was discussed that the magnetic particles with larger core sizes ($d_C > 20$ nm) contribute most dominantly to the FMMD signal.

In this chapter, we further analyze the core size determination of ensembles of MNPs using FMMD measurements and fitting the results with a lognormally distributed core size-dependent Langevin model in thermodynamic equilibrium which has been explained in 2.4. We elaborate on the ambiguity that occurs from evaluating the fitting findings and provide a strategy for addressing this ambiguity using the quantity of iron determined by ICP-OES.

The chapter is based on the original publication by the author [105].

8.1. Magnetic beads

Magnetic nanoparticle samples used during this study were procured from Micromod Partikeltechnologie GmbH (Rostock, Germany). We have used two different particle types with varying hydrodynamic diameters, both having a plain surface coating as listed in Table 16.

Table 16. List of magnetic MNP types used in the experiments

Type	Hydrodynamic size d_H [nm]	Stock concentration [mg/mL]	Surface
Nanomag-D spio	20	25	Dextran
SynomagD	70	25	Dextran

8.2. ICP-OES measurements

For the determination of absolute iron content, we carried out ICP-OES measurements using iCAP 7600 device. The prepared sample materials were dissolved from each container through addition of a total amount of 2 mL HCl. The sample containers were rinsed several times with Milli-Q water, and each sample was combined in a 15 mL falcon tube. Each solution was made up of a total volume of 10 mL. Finally, three parallel dilutions of each digestion solution (10-fold diluted) were prepared and analyzed.

8.3. Calculation of the iron mass

In the case of Fe_3O_4 MNP dilution, the iron mass per sample can be calculated as follows, taking into account the iron binding ratio, the density of Fe_3O_4 being 5175 kg/m^3, the weight percentage of iron in magnetite (determined from the molar masses of iron, $M_{Fe} = 55.845$ g/mol and of oxygen, $M_O = 15.999$ g/mol), and additional information on the size distribution f_L from equations (20 and 23):

$$m_{Fe} = \frac{3M_{Fe}}{3M_{Fe} + 4M_O} \cdot \rho_{Fe_3O_4} \cdot N_p \cdot \frac{\pi}{6} \cdot \int_0^\infty dd_c d_c^3 \, f_L \,(d_c, d_0, \sigma) \qquad \text{Eq.55}$$

The integral may be analytically solved using the assumption of a lognormal distribution, leading to:

$$\int_0^\infty dd_c d_c^3 \, f_L \,(d_c, d_0, \sigma) = d_0^3 \exp(\frac{9\sigma^2}{2}) \qquad \text{Eq.56}$$

8.4. Sample preparation

The samples of two different types of commercial magnetic beads of type synomag®-D with d_h of 70 nm (named *Syn70*) and Nanomag®-D SPIO with d_h of 20 nm (named *ND20*) were prepared with MNP concentration of 0.33 µg/µL using the immobilization protocol described in the sample preparation chapter.

8.5. Measurement and data processing procedure

The FMMD signals of the prepared samples were measured using the setup described in section 3.3. The measured data post-processing was done according to section 5.1. The unit conversion of the signal intensity from the measured signal amplitude in mV to the sample's nonlinear magnetic moment in nAm^2 was performed according to calibration method explained in section 3.6.

8.6. Measurement and Fit

The static offset magnetic field was varied from 0 to 24 mT in steps of 1 mT. Figure 77 shows the offset-dependent nonlinear magnetization response of the samples *Syn70* and *ND20* for the first four mixing terms $f_1 + nf_2; n = \{1,2,3,4\}$. The measurement results for these samples are depicted as solid red circles and solid black squares, respectively. In order to determine the average core size parameters, with the assumption of a lognormal distribution of the core sizes, each measurement was fitted using the model of calculating the nonlinear magnetic moments according to Eq. (38 and 39), integrated over a lognormal distribution (Eq.20) with three fitting parameters, $m(d_0,\sigma,N_p)$, through a nonlinear least square Levenberg-Marquardt optimization algorithm. Additionally, the respective fits to each measurement are also depicted as a solid line with matching colors in Figure 77. The fitted theoretical signals agree very well with the measurement data, with $R^2 > 0.99$.

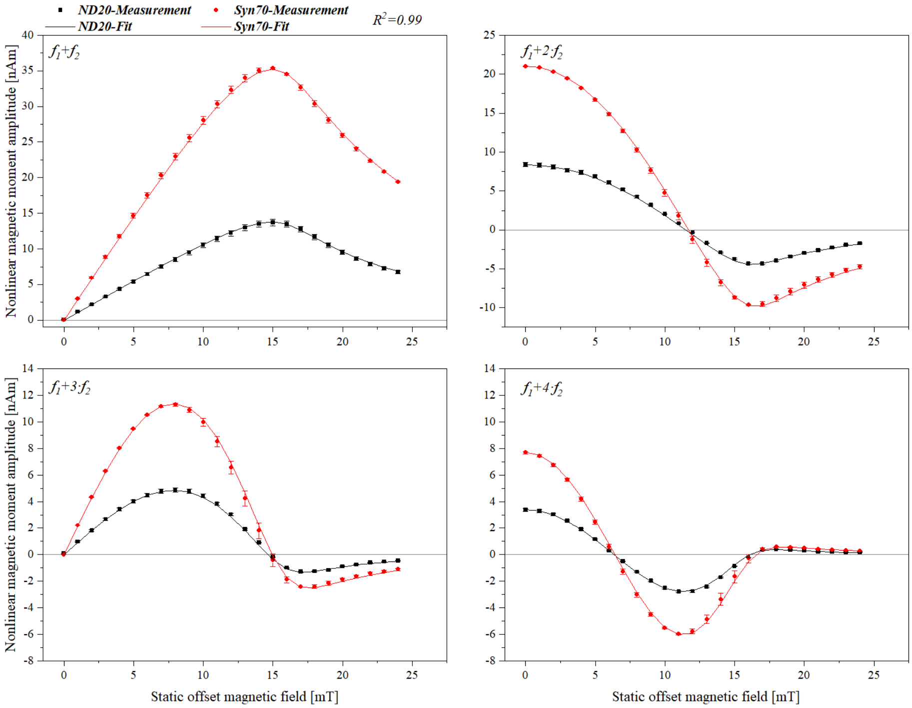

Figure 77. Measured first four nonlinear magnetic moment responses of samples Syn70 and ND20 with MNP concentration of 0.33 µg/µL at mixing frequencies $f_1 + f_2$, $f_1 + 2{\cdot}f_2$, $f_1 + 3{\cdot}f_2$ and $f_1 + 4{\cdot}f_2$ over a static magnetic offset field range from 0 to 24 mT. The red-filled circles represent the measurement data of the sample Syn70 and the solid red line represents the fitting to the respective measurement data. The black squares represent the measurement data of ND20 and the black solid line represents the fitting.

The parameters obtained from fitting to the Syn70 sample were $d_0 = 6.26$ nm, $\sigma = 0.37$ and $N_p = 4.0{\times}10^{13}$, the result of the ND20 fit was $d_0 = 5.86$ nm, $\sigma = 0.4$ and $N_p = 1.4{\times}10^{13}$.

However, it was found that the convergence of fits depended strongly on the choice of starting values. For further analysis, we, therefore, examined a wide range of median diameters d_0 between 5 nm and 18 nm, and a range of width parameters σ from 0.1 to 0.4. For fixed pairs (d_0, σ) in these ranges, we fitted just the amplitude N_p and plotted the fit quality R^2 in a contour plot as a function of d_0 and σ, see Figure 78 (a). It is clearly seen that a “ridge” of pairs (d_0, σ) yields excellent fits to the experimental data depicted in Figure 77 (a), with $R^2 > 0.99$. The “ridge top”, i.e. the σ values which give maximum R^2 for a given d_0, is marked by the solid cyan line. The lognormal core size distributions corresponding to the colored squares on that line are shown in Figure 78 (b).

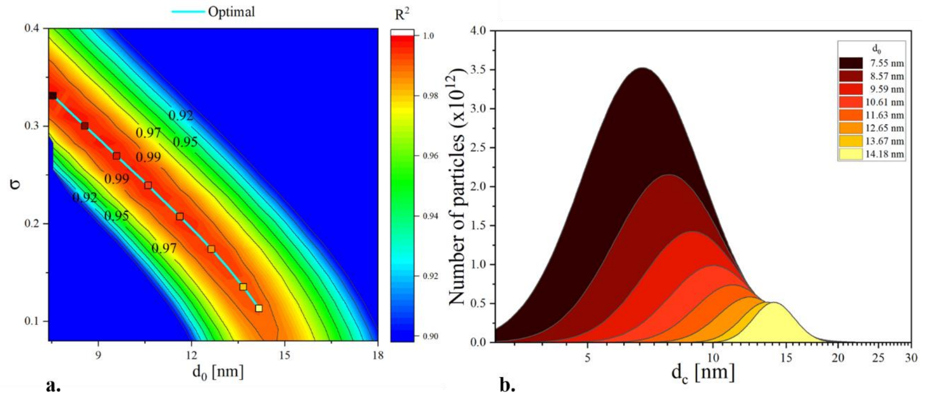

Figure 78. a) The contour plot of the R^2 values for different combinations of the parameters d_0 and σ, the optimal parameter line (with $R^2 > 0.99$) is depicted as a solid cyan line for the sample Syn70, b) The lognormal distribution of the optimal parameters which results in $R^2 > 0.99$, the legend shows different medians of the core size distributions. The corresponding (d_0,σ) combinations have been marked with respective colors on the optimal parameter line in (a).

The different lognormal core size distributions depicted in Figure 78(b) all yield simulated FMMD signals which resemble very well the measured data (with $R^2 > 0.99$). So there is an ambiguity in the core size determination of the sample from FMMD measurement, the inverse problem is ill-posed. The reason for this is that small particles have an almost negligible contribution to the signal since their signal scales with the 12th power of particle core diameter, $\propto d_c^{12}$. A wide distribution with a small median diameter (for instance the dark brown distribution for $d_0 = 7.55$ nm in Figure 78(b)) has an enormous number of small particles which practically don't contribute to the FMMD signal, but do yield a considerable contribution to the iron mass (which scales with the 3rd power of the diameter, $\propto d_c^3$). The FMMD signal is constituted only from the relatively small amount of larger particles in that distribution. In contrast, all particles of a narrow distribution with a large median diameter (for instance the bright yellow distribution for $d_0 = 14.18$ nm in Figure 78(b)) contribute strongly to the FMMD signal. Therefore, the light yellow distribution needs much less iron to produce the same FMMD signal compared to the dark brown distribution with its multitude of non-contributing small particles, as for $d_0 = 14.18$ nm, the iron is favorably arranged in larger particles. We propose to resolve this fitting ambiguity by an independent determination of the total iron content of the sample. From all the possible distributions depicted in Figure 78(b), we choose the one matching the measured amount of iron.

One can calculate the mass of iron (m_{Fe}) for all the distributions on the optimal parameter line using Eqs. (46) and (47). This was done by constraining the median core size d_0 and finding the best-fitting σ and N_p, leading to $R^2 > 0.99$. The true absolute amount of iron of the measured sample was determined by ICP-OES. Combining the FMMD measurement analysis for different distributions and the calculated iron mass, we generate a look-up graph, which relates a combination of (d_0, σ) marked with black squares uniquely to a number of particles (plotted as red squares) and thus to an iron mass (blue squares), respectively. This allows to oneuniquely select the particle size distribution for which the measured iron mass (in our case obtained from ICP-OES) equals the calculated one. Figure 79 shows the look-up graph for the *Syn70* sample, in which the measured amount of iron was (17.73 ± 0.19) μg. The point of intersection was determined through a linear interpolation between the two neighboring points. The analysis reveals the size distribution with parameters $d_0 = 10.6\ nm$, $\sigma = 0.24$ and $N_p = 5.8\cdot 10^{12}$.

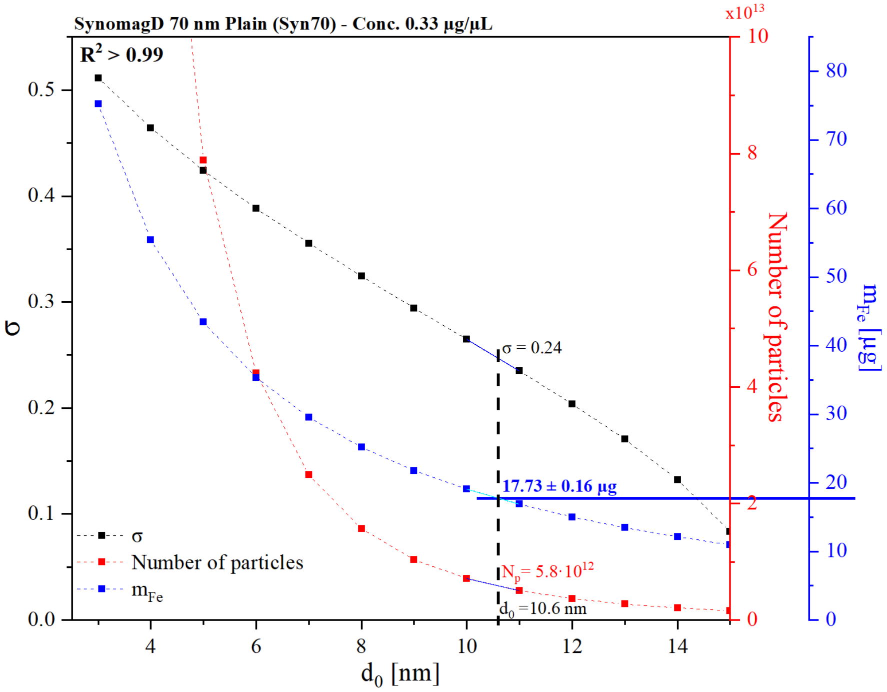

Figure 79. Look-up graph of sample Syn70, for the best combinations of the magnetic core size distribution (d_0, σ, N_P) leading to $R^2 > 0.99$. The σ values are depicted as black squares. The number of particles N_p are depicted as red squares and the calculated m_{Fe} are depicted as blue squares. The measured iron mass through ICP-OES is marked using a blue line. The intersection points are marked using a dashed line. For each parameter, the points are connected to guide the eye.

The same process was repeated to analyze the measurement of the sample *ND20* presented in Figure 80. The result of the analysis yields a $d_0 = 13.5$ nm with $\sigma = 0.16$ and $N_p = 8.4\cdot 10^{11}$. The results for both samples are listed in Table 17.

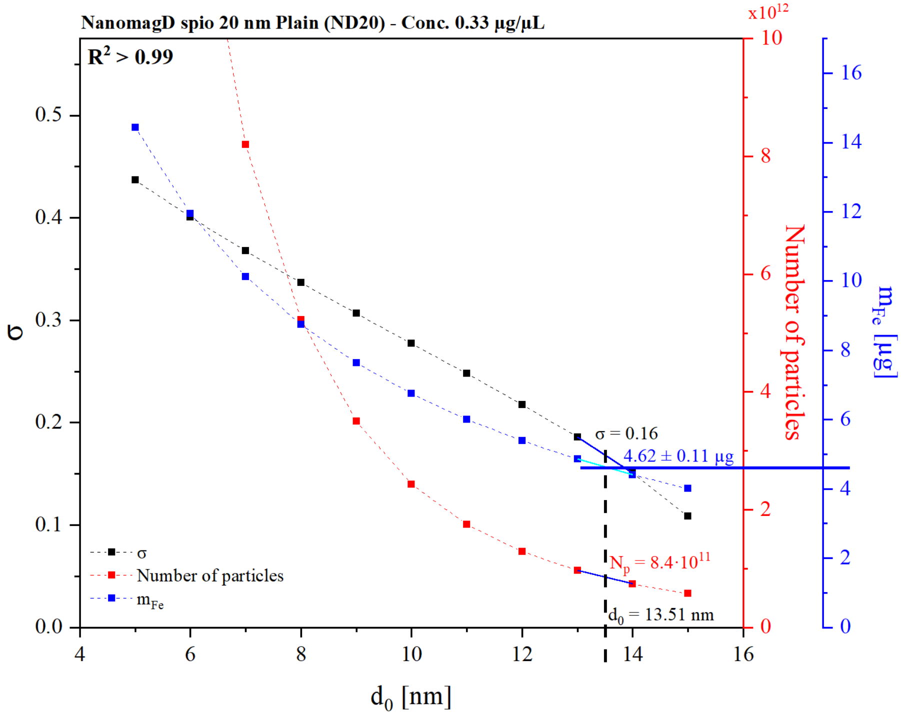

Figure 80. Look-up graph of ND20, for the best combinations of the magnetic core size distribution (d_0, σ, N_P) leading to $R^2 > 0.99$. The σ values are depicted as black squares. The number of particles N_p are depicted as red squares and the calculated m_{Fe} are depicted as blue squares. The measured amount of iron through ICP-OES is marked using a blue line. For each parameter, the points are connected for better visual aid.

Table 17. Iron mass of the samples measured with ICP-OES, and lognormal distribution parameters of the particles' core sizes obtained from this iron content.

Sample	*d_h [nm]*	*Measured m_{Fe} [µg]*	*Determined d_0 [nm]*	*Determined σ*	*Determined N_p*
Syn70	70	17.73 ± 0.19	10.6	0.24	$5.8 \cdot 10^{12}$
ND20	20	4.62 ± 0.11	13.5	0.16	$8.4 \cdot 10^{11}$

For comparison, the core sizes reported in the literature for the MNPs used here are slightly smaller. For Synomag D 70 nm particles, Ref. [131] reported an individual core size of 8.25 nm from analysis of TEM micrographs, and in the case of NanomagD SPIO 20 nm, Ref. [132] gave a core size of 11.2 nm obtained from analysis of the DC magnetization curve from a Magnetic Property Measurement System (MPMS). For both particle types, our FMMD analysis yielded approximately 2 nm larger core sizes. A possible reason for the deviations may be the fact that our FMMD analysis forces the core size distribution to be lognormal. If the particle distribution is different, for instance bimodal, the mathematical determination of iron mass would be erroneous. In addition, our theoretical description is based on the assumption that all the atoms in a particle contribute to the particle's magnetic moment, without any non-interacting amorphous boundary layer. In addition, the precision of all the different measurement techniques

TEM, MPMS and FMMD is limited. The error of each technique is at least 1 to 2 nm, so that it can be concluded that the results do agree within the error limits.

8.7. Conclusions

Offset-field-dependent FMMD measurements were performed for two different MNP types. Core size distribution analysis was performed by fitting the calculated signals from the Langevin theory with lognormally distributed core sizes to the measurements. Further analysis revealed an ambiguity in the evaluation of the fitting results, leading to a number of equally well-suited fitting results for different combinations of median size d_0, size distribution width σ and number of particles per sample N_p, all of which yielded excellent agreement with measured data. The ambiguity was successfully resolved by measuring the total iron mass of the samples using ICP-OES and translating the iron mass into a look-up graph using the parameters of the fitting function and the calculated m_{Fe}. This graph allows us to unequivocally select the one combination of (d_0, σ, N_p) with the measured amount of iron directly and reproducibly.

In future, this method should be further verified using alternative iron amount determination techniques such as photometry using a suitable iron-indicator (e.g. phenanthroline). Furthermore, improved accuracy could be achieved by including additional external parameters such as the saturation magnetization M_s of the sample which could be determined by VSM.

Overall, once this method is established, i.e. having reliable look-up-graphs for commonly used samples, a single determination of iron mass can then complete the full characterization of a unique sample (MNP ensemble) by directly yielding the underlying core-size distribution from an FMMD measurement. This would render FMMD as a highly effective MNP characterization method, as many biomedical applications of MNPs (s. section 1) are dominated by core-size effects, e.g. MPI [133,134] and MNP-mediated hyperthermia [135,136] .

Chapter 9

9. Conclusion and future directions

In the scope of this thesis, Frequency mixing magnetic detection (FMMD) technique was employed to study magnetic nanoparticles (MNPs) samples for the applications in multiplex detection in magnetic immunoassays. Furthermore, the technique was used as a characterization tool for the determination of the magnetic core size distribution of the MNP samples.

Initially, the instrumentation involved in acquiring the FMMD signals. For the hand-held measurement device, an android-based application was developed to further enhance the user device interface experience. The smartphone application allows for storing the measurement data on the cloud and lays the foundations for developing online evaluation tools. Furthermore, we provided protocols for calibration of the magnetic reader systems excitation and demodulation chain. To obtain magnetic offset-dependent FMMD signals, it is required to use a static offset magnetic field generation source. Traditionally, an electromagnet is utilized to provide this magnetic offset which comes with extensive unwanted heat generation. Reduction of the temperature influence was achieved by adopting a power management strategy by pulsing the current supplied to the coil using the 70 % duty cycle. This resulted in a 30% reduction in the temperature at the highest field. Moreover, a new version of a measurement head was discussed which used a pair of permanent ring magnets as its static offset magnetic field generation source. The FMMD signals were measured with both PMOM and EMOM setups, yielding a good agreement with a deviation of 4.5 %. In the future, a Hall sensor should be integrated into the measurement head to read for reading out the magnetic field values. The position of the sensor needs to be optimized and the correlation to the magnetic field at the sample position needs to be determined. Furthermore, the PMOM device needs to be motorized for automatic and precise variation of the permanent ring magnet distances.

Using the digital demodulation scheme, deeper phase analysis of the FMMD signals was conducted. The study revealed the impact of the phase of excitation fields on the measured complex mixing frequency harmonics. Variation of the phase of the low-frequency excitation magnetic field will change the angle between the two symmetric harmonics in the complex domain, whereas a change in the phase of the high-frequency excitation field will just rotate both symmetric harmonics in the complex plane. The effect was initially studied using simulations and later verified using experimental data.

To utilize MNPs in multiplex detection, we used offset-dependent FMMD signals. Characterization of different commercially available MNPs revealed that the features of the FMMD signals vary for different particle types. In binary and ternary mixtures of different MNP types, it can be seen that both the amplitude response and the feature locations change. A straightforward approach was used to determine the best linear combination of the reference samples through a quadratic programming optimization algorithm. The results show a reasonable agreement to the expected values with a maximum deviation of 14%. In future, optimization needs to be carried out to reduce the errors in the preparation of the samples which may also arise from the interaction of different particle types. The method needs to be tested with actual immunoassay samples.

The lognormal distribution of MNPs was used to develop an inverse problem for the determination of the core size distribution of MNPs. The ambiguity in the analysis was addressed leading to a number of equally well-suited fitting results for different combinations of median size (d_0), size distribution width σ and number of particles per sample N_p, all of which yielded excellent agreement with measured data. The ambiguity was resolved using an external parameter, in this case total iron mass in the samples determined through ICP-OES measurements. As a result, a look-up table graph can be generated allowing us to unequivocally choose the best combination of (d_0, σ, N_p). Analysis for two different particle types was performed, the results of which were within the reported range in the literature. In future, this method needs to be further verified using different iron determination techniques. Further precision improvement could be achieved by incorporating additional material information such as saturation magnetization M_s which can be determined using VSM.

As a general outlook of the FMMD instrumentation, flow-through measurements would be advantageous for sequential multi-sample handling and also for online monitoring of MNP synthesis. For this, a double-entry measurement head was developed the related figure is presented in Appendix (6). Initial characterization and signal assessment was performed and presented in Appendix (7). Further experiments must be done for optimization and application-based experiments using this measurement head.

Moreover, an extension of the FMMD theory using Debye relaxation was explored. The Debye relation theory involves the relaxation mechanism in MNPs. Evaluation of the measured signals with FMMD-Debye extension would reveal more information about the hydrodynamic size and binding state of the MNPs.

In this thesis, we used a parallel static offset magnetic field which is oriented in parallel to the AC excitation fields. The static field can also be applied perpendicular to the AC field. A theoretical formalism for calculating the relaxation times in perpendicular magnetic fields is available at [137,138]. In order to explore this effect experimentally, a new static magnetic offset coil system was developed, based on a Helmholtz coil arrangement to apply the static field perpendicular to the alternating excitation fields. The measurement head system is presented in Appendix (8). The determination of the coil factor and the characterization of its field profile are presented in appendix (9). Further experiments and simulations of the FMMD signals are required to utilize this measurement head.

Bibliography

1. Wang, X.; Hu, L. Review—Enzymatic Strips for Detection of Serum Total Cholesterol with Point-of-Care Testing (POCT) Devices: Current Status and Future Prospect. *J. Electrochem. Soc.* **2020**, *167*, 037535, doi:10.1149/1945-7111/ab64bb.
2. Boyd, M.; Woolley, T. Point of Care Testing. *Surgery (Oxford)* **2016**, *34*, 91–93, doi:10.1016/j.mpsur.2015.11.004.
3. Hutton, J.; Doyle, J.; Zordan, R.; Weiland, T.; Cocco, A.; Howell, J.; Iser, S.; Snell, J.; Fry, S.; New, K.; et al. Point-of-Care Hepatitis C Virus Testing and Linkage to Treatment in an Australian Inner-City Emergency Department. *International Journal of Drug Policy* **2019**, *72*, 84–90, doi:10.1016/j.drugpo.2019.06.021.
4. Gomes, H.I.A.S.; Sales, M.G.F. Development of Paper-Based Color Test-Strip for Drug Detection in Aquatic Environment: Application to Oxytetracycline. *Biosensors and Bioelectronics* **2015**, *65*, 54–61, doi:10.1016/j.bios.2014.10.006.
5. Gunda, N.S.K.; Gautam, S.H.; Mitra, S.K. Artificial Intelligence Based Mobile Application for Water Quality Monitoring. *J. Electrochem. Soc.* **2019**, *166*, B3031–B3035, doi:10.1149/2.0081909jes.
6. Gao, H.; Wen, L.; Tian, J.; Wu, Y.; Liu, F.; Lin, Y.; Hua, W.; Wu, G. A Portable Electrochemical Immunosensor for Highly Sensitive Point-of-Care Testing of Genetically Modified Crops. *Biosensors and Bioelectronics* **2019**, *142*, 111504, doi:10.1016/j.bios.2019.111504.
7. Kuswandi, B.; Gani, A.A.; Ahmad, M. Immuno Strip Test for Detection of Pork Adulteration in Cooked Meatballs. *Food Bioscience* **2017**, *19*, 1–6, doi:10.1016/j.fbio.2017.05.001.
8. Yang, J.; Wang, K.; Xu, H.; Yan, W.; Jin, Q.; Cui, D. Detection Platforms for Point-of-Care Testing Based on Colorimetric, Luminescent and Magnetic Assays: A Review. *Talanta* **2019**, *202*, 96–110, doi:10.1016/j.talanta.2019.04.054.
9. Carrio, A.; Sampedro, C.; Sanchez-Lopez, J.L.; Pimienta, M.; Campoy, P. Automated Low-Cost Smartphone-Based Lateral Flow Saliva Test Reader for Drugs-of-Abuse Detection. *Sensors* **2015**, *15*, 29569–29593, doi:10.3390/s151129569.
10. Murshed, M.F.; Aslam, Z.; Lewis, R.; Chow, C.; Wang, D.; Drikas, M.; van Leeuwen, J. Changes in the Quality of River Water before, during and after a Major Flood Event Associated with a La Niña Cycle and Treatment for Drinking Purposes. *Journal of Environmental Sciences* **2014**, *26*, 1985–1993, doi:10.1016/j.jes.2014.08.001.
11. St-Louis, P. Status of Point-of-Care Testing: Promise, Realities, and Possibilities. *Clinical Biochemistry* **2000**, *33*, 427–440, doi:10.1016/S0009-9120(00)00138-7.
12. Alhajj, M.; Farhana, A. Enzyme Linked Immunosorbent Assay. In *StatPearls*; StatPearls Publishing: Treasure Island (FL), 2022.
13. Spadaro, D.; Meloni, G.R.; Siciliano, I.; Prencipe, S.; Gullino, M.L. HPLC-MS/MS Method for the Detection of Selected Toxic Metabolites Produced by Penicillium Spp. in Nuts. *Toxins* **2020**, *12*, 307, doi:10.3390/toxins12050307.
14. Luppa, P.B.; Müller, C.; Schlichtiger, A.; Schlebusch, H. Point-of-Care Testing (POCT): Current Techniques and Future Perspectives. *TrAC Trends in Analytical Chemistry* **2011**, *30*, 887–898, doi:10.1016/j.trac.2011.01.019.

15. Xu, Y.; Liu, Y.; Wu, Y.; Xia, X.; Liao, Y.; Li, Q. Fluorescent Probe-Based Lateral Flow Assay for Multiplex Nucleic Acid Detection. *Anal. Chem.* **2014**, *86*, 5611–5614, doi:10.1021/ac5010458.
16. Tian, L.; Sato, T.; Niwa, K.; Kawase, M.; Tanner, A.C.R.; Takahashi, N. Rapid and Sensitive PCR-Dipstick DNA Chromatography for Multiplex Analysis of the Oral Microbiota. *BioMed Research International* **2014**, *2014*, e180323, doi:10.1155/2014/180323.
17. Panfilova, E.; Shirokov, A.; Khlebtsov, B.; Matora, L.; Khlebtsov, N. Multiplexed Dot Immunoassay Using Ag Nanocubes, Au/Ag Alloy Nanoparticles, and Au/Ag Nanocages. *Nano Res.* **2012**, *5*, 124–134, doi:10.1007/s12274-012-0193-6.
18. Caspani, S.; Magalhães, R.; Araújo, J.P.; Sousa, C.T. Magnetic Nanomaterials as Contrast Agents for MRI. *Materials (Basel)* **2020**, *13*, 2586, doi:10.3390/ma13112586.
19. Shokrollahi, H. Contrast Agents for MRI. *Materials Science and Engineering: C* **2013**, *33*, 4485–4497, doi:10.1016/j.msec.2013.07.012.
20. *Magnetic Particle Imaging: A Novel SPIO Nanoparticle Imaging Technique*; Buzug, T.M., Borgert, J., Eds.; Springer proceedings in physics; Springer: Heidelberg, 2012; ISBN 978-3-642-24132-1.
21. Mattern, A.; Sandig, R.; Joos, A.; Löwa, N.; Kosch, O.; Weidner, A.; Wells, J.; Wiekhorst, F.; Dutz, S. Magnetic Nanoparticle-Gel Materials for Development of MPI and MRI Phantoms. *International Journal on Magnetic Particle Imaging* **2018**, *4*, doi:10.18416/IJMPI.2018.1811001.
22. Le, T.-A.; Zhang, X.; Hoshiar, A.K.; Yoon, J. Real-Time Two-Dimensional Magnetic Particle Imaging for Electromagnetic Navigation in Targeted Drug Delivery. *Sensors* **2017**, *17*, 2050, doi:10.3390/s17092050.
23. Guo, R.; Wang, S.; Huang, F.; Chen, Q.; Li, Y.; Liao, M.; Lin, J. Rapid Detection of Salmonella Typhimurium Using Magnetic Nanoparticle Immunoseparation, Nanocluster Signal Amplification and Smartphone Image Analysis. *Sensors and Actuators B: Chemical* **2019**, *284*, 134–139, doi:10.1016/j.snb.2018.12.110.
24. Schwaminger, S.P.; Fraga-García, P.; Eigenfeld, M.; Becker, T.M.; Berensmeier, S. Magnetic Separation in Bioprocessing Beyond the Analytical Scale: From Biotechnology to the Food Industry. *Frontiers in Bioengineering and Biotechnology* **2019**, *7*.
25. Thomas, J.A.; Schnell, F.; Kaveh-Baghbaderani, Y.; Berensmeier, S.; Schwaminger, S.P. Immunomagnetic Separation of Microorganisms with Iron Oxide Nanoparticles. *Chemosensors* **2020**, *8*, 17, doi:10.3390/chemosensors8010017.
26. Öztürk Er, E.; Dalgıç Bozyiğit, G.; Büyükpınar, Ç.; Bakırdere, S. Magnetic Nanoparticles Based Solid Phase Extraction Methods for the Determination of Trace Elements. *Critical Reviews in Analytical Chemistry* **2022**, *52*, 231–249, doi:10.1080/10408347.2020.1797465.
27. Hedayatnasab, Z.; Abnisa, F.; Daud, W.M.A.W. Review on Magnetic Nanoparticles for Magnetic Nanofluid Hyperthermia Application. *Materials & Design* **2017**, *123*, 174–196, doi:10.1016/j.matdes.2017.03.036.
28. Engelmann, U.M.; Roeth, A.A.; Eberbeck, D.; Buhl, E.M.; Neumann, U.P.; Schmitz-Rode, T.; Slabu, I. Combining Bulk Temperature and Nanoheating Enables Advanced Magnetic Fluid Hyperthermia Efficacy on Pancreatic Tumor Cells. *Sci Rep* **2018**, *8*, 13210, doi:10.1038/s41598-018-31553-9.
29. Fabris, F.; Lima, E.; De Biasi, E.; Troiani, H.E.; Vásquez Mansilla, M.; Torres, T.E.; Fernández Pacheco, R.; Ibarra, M.R.; Goya, G.F.; Zysler, R.D.; et al. Controlling the Dominant Magnetic Relaxation Mechanisms for Magnetic Hyperthermia in

Bimagnetic Core–Shell Nanoparticles. *Nanoscale* **2019**, *11*, 3164–3172, doi:10.1039/C8NR07834C.

30. Engelmann, U.M.; Fitter, J.L.; Baumann, M. Assessing Magnetic Fluid Hyperthermia : Magnetic Relaxation Simulation, Modeling of Nanoparticle Uptake inside Pancreatic Tumor Cells and in Vitro Efficacy, Infinite Science Publishing, 2019.
31. Rytov, R.A.; Bautin, V.A.; Usov, N.A. Towards Optimal Thermal Distribution in Magnetic Hyperthermia. *Sci Rep* **2022**, *12*, 3023, doi:10.1038/s41598-022-07062-1.
32. Rösch, E.L.; Zhong, J.; Lak, A.; Liu, Z.; Etzkorn, M.; Schilling, M.; Ludwig, F.; Viereck, T.; Lalkens, B. Point-of-Need Detection of Pathogen-Specific Nucleic Acid Targets Using Magnetic Particle Spectroscopy. *Biosensors and Bioelectronics* **2021**, *192*, 113536, doi:10.1016/j.bios.2021.113536.
33. Gaster, R.S.; Xu, L.; Han, S.-J.; Wilson, R.J.; Hall, D.A.; Osterfeld, S.J.; Yu, H.; Wang, S.X. Quantification of Protein Interactions and Solution Transport Using High-Density GMR Sensor Arrays. *Nature Nanotech* **2011**, *6*, 314–320, doi:10.1038/nnano.2011.45.
34. Chung, H.J.; Castro, C.M.; Im, H.; Lee, H.; Weissleder, R. A Magneto-DNA Nanoparticle System for Rapid Detection and Phenotyping of Bacteria. *Nature Nanotech* **2013**, *8*, 369–375, doi:10.1038/nnano.2013.70.
35. Osterfeld, S.J.; Yu, H.; Gaster, R.S.; Caramuta, S.; Xu, L.; Han, S.-J.; Hall, D.A.; Wilson, R.J.; Sun, S.; White, R.L.; et al. Multiplex Protein Assays Based on Real-Time Magnetic Nanotag Sensing. *PNAS* **2008**, *105*, 20637–20640, doi:10.1073/pnas.0810822105.
36. Wu, K.; Tonini, D.; Liang, S.; Saha, R.; Chugh, V.K.; Wang, J.-P. Giant Magnetoresistance Biosensors in Biomedical Applications. *ACS Appl. Mater. Interfaces* **2022**, *14*, 9945–9969, doi:10.1021/acsami.1c20141.
37. Shen, W.; Schrag, B.D.; Carter, M.J.; Xie, J.; Xu, C.; Sun, S.; Xiao, G. Detection of DNA Labeled with Magnetic Nanoparticles Using MgO-Based Magnetic Tunnel Junction Sensors. *Journal of Applied Physics* **2008**, *103*, 07A306, doi:10.1063/1.2832880.
38. Ludwig, F.; Mäuselein, S.; Heim, E.; Schilling, M. Magnetorelaxometry of Magnetic Nanoparticles in Magnetically Unshielded Environment Utilizing a Differential Fluxgate Arrangement. *Review of Scientific Instruments* **2005**, *76*, 106102, doi:10.1063/1.2069776.
39. Lee, H.; Sun, E.; Ham, D.; Weissleder, R. Chip–NMR Biosensor for Detection and Molecular Analysis of Cells. *Nat Med* **2008**, *14*, 869–874, doi:10.1038/nm.1711.
40. Kotitz, R.; Matz, H.; Trahms, L.; Koch, H.; Weitschies, W.; Rheinlander, T.; Semmler, W.; Bunte, T. SQUID Based Remanence Measurements for Immunoassays. *IEEE Trans. Appl. Supercond.* **1997**, *7*, 3678–3681, doi:10.1109/77.622216.
41. Astalan, A.P.; Ahrentorp, F.; Johansson, C.; Larsson, K.; Krozer, A. Biomolecular Reactions Studied Using Changes in Brownian Rotation Dynamics of Magnetic Particles. *Biosensors and Bioelectronics* **2004**, *19*, 945–951, doi:10.1016/j.bios.2003.09.005.
42. Krause, H.-J.; Wolters, N.; Zhang, Y.; Offenhäusser, A.; Miethe, P.; Meyer, M.H.F.; Hartmann, M.; Keusgen, M. Magnetic Particle Detection by Frequency Mixing for Immunoassay Applications. *Journal of Magnetism and Magnetic Materials* **2007**, *311*, 436–444, doi:10.1016/j.jmmm.2006.10.1164.

43. Pietschmann, J.; Spiegel, H.; Krause, H.-J.; Schillberg, S.; Schröper, F. Sensitive Aflatoxin B1 Detection Using Nanoparticle-Based Competitive Magnetic Immunodetection. *Toxins* **2020**, *12*, 337, doi:10.3390/toxins12050337.
44. Pietschmann, J.; Dittmann, D.; Spiegel, H.; Krause, H.-J.; Schröper, F. A Novel Method for Antibiotic Detection in Milk Based on Competitive Magnetic Immunodetection. *Foods* **2020**, *9*, 1773, doi:10.3390/foods9121773.
45. Achtsnicht, S.; Neuendorf, C.; Faßbender, T.; Nölke, G.; Offenhäusser, A.; Krause, H.-J.; Schröper, F. Sensitive and Rapid Detection of Cholera Toxin Subunit B Using Magnetic Frequency Mixing Detection. *PLOS ONE* **2019**, *14*, e0219356, doi:10.1371/journal.pone.0219356.
46. Meyer, M.H.F.; Krause, H.-J.; Hartmann, M.; Miethe, P.; Oster, J.; Keusgen, M. Francisella Tularensis Detection Using Magnetic Labels and a Magnetic Biosensor Based on Frequency Mixing. *Journal of Magnetism and Magnetic Materials* **2007**, *311*, 259–263, doi:10.1016/j.jmmm.2006.10.1175.
47. Meyer, M.H.F.; Hartmann, M.; Krause, H.-J.; Blankenstein, G.; Mueller-Chorus, B.; Oster, J.; Miethe, P.; Keusgen, M. CRP Determination Based on a Novel Magnetic Biosensor. *Biosensors and Bioelectronics* **2007**, *22*, 973–979, doi:10.1016/j.bios.2006.04.001.
48. Rettcher, S.; Jungk, F.; Kühn, C.; Krause, H.-J.; Nölke, G.; Commandeur, U.; Fischer, R.; Schillberg, S.; Schröper, F. Simple and Portable Magnetic Immunoassay for Rapid Detection and Sensitive Quantification of Plant Viruses. *Appl. Environ. Microbiol.* **2015**, *81*, 3039–3048, doi:10.1128/AEM.03667-14.
49. Hong, H.-B. Detection of Two Different Influenza A Viruses Using a Nitrocellulose Membrane and a Magnetic Biosensor. *Journal of Immunological Methods* **2011**, 6.
50. Wu, K.; Liu, J.; Saha, R.; Su, D.; Krishna, V.D.; Cheeran, M.C.-J.; Wang, J.-P. Magnetic Particle Spectroscopy for Detection of Influenza A Virus Subtype H1N1. *ACS Appl. Mater. Interfaces* **2020**, *12*, 13686–13697, doi:10.1021/acsami.0c00815.
51. Achtsnicht, S.; Pourshahidi, A.M.; Offenhäusser, A.; Krause, H.-J. Multiplex Detection of Different Magnetic Beads Using Frequency Scanning in Magnetic Frequency Mixing Technique. *Sensors* **2019**, *19*, 2599, doi:10.3390/s19112599.
52. Achtsnicht, S.; Tödter, J.; Niehues, J.; Telöken, M.; Offenhäusser, A.; Krause, H.-J.; Schröper, F. 3D Printed Modular Immunofiltration Columns for Frequency Mixing-Based Multiplex Magnetic Immunodetection. *Sensors* **2019**, *19*, 148, doi:10.3390/s19010148.
53. Sandler, S.E.; Fellows, B.; Mefford, O.T. Best Practices for Characterization of Magnetic Nanoparticles for Biomedical Applications. *Anal. Chem.* **2019**, *91*, 14159–14169, doi:10.1021/acs.analchem.9b03518.
54. Nieciecka, D.; Rękorajska, A.; Cichy, D.; Końska, P.; Żuk, M.; Krysiński, P. Synthesis and Characterization of Magnetic Drug Carriers Modified with Tb3+ Ions. *Nanomaterials* **2022**, *12*, 795, doi:10.3390/nano12050795.
55. Ludwig, F.; Guillaume, A.; Schilling, M.; Frickel, N.; Schmidt, A.M. Determination of Core and Hydrodynamic Size Distributions of CoFe2O4 Nanoparticle Suspensions Using Ac Susceptibility Measurements. *Journal of Applied Physics* **2010**, *108*, 033918, doi:10.1063/1.3463350.
56. Krishnan, K.M. *Fundamentals and Applications of Magnetic Materials*; Oxford University Press, 2016; ISBN 978-0-19-957044-7.
57. Aharoni, A. *An Introduction to the Theory of Ferromagnetism*; 2000; ISBN 978-0-19-850809-0.
58. Gross, R.; Marx, A. *Festkörperphysik*; De Gruyter Oldenbourg, 2014; ISBN 978-3-11-035870-4.

59. Petracic, O. Superparamagnetic Nanoparticle Ensembles. *Superlattices and Microstructures* **2010**, *47*, 569–578, doi:10.1016/j.spmi.2010.01.009.
60. Huang, P.-J.; Marks, H.L.; Coté, G.L.; Kameoka, J. A Magneto-Fluidic Nanoparticle Trapping Platform for Surface-Enhanced Raman Spectroscopy. *Biomicrofluidics* **2017**, *11*, 034116, doi:10.1063/1.4985071.
61. Wells, J.; Kazakova, O.; Posth, O.; Steinhoff, U.; Petronis, S.; Bogart, L.K.; Southern, P.; Pankhurst, Q.; Johansson, C. Standardisation of Magnetic Nanoparticles in Liquid Suspension. *J. Phys. D: Appl. Phys.* **2017**, *50*, 383003, doi:10.1088/1361-6463/aa7fa5.
62. Chen, Y.-T.; Kolhatkar, A.G.; Zenasni, O.; Xu, S.; Lee, T.R. Biosensing Using Magnetic Particle Detection Techniques. *Sensors* **2017**, *17*, 2300, doi:10.3390/s17102300.
63. Laurent, S.; Forge, D.; Port, M.; Roch, A.; Robic, C.; Vander Elst, L.; Muller, R.N. Magnetic Iron Oxide Nanoparticles: Synthesis, Stabilization, Vectorization, Physicochemical Characterizations, and Biological Applications. *Chem. Rev.* **2008**, *108*, 2064–2110, doi:10.1021/cr068445e.
64. Lee, H.; Shin, T.-H.; Cheon, J.; Weissleder, R. Recent Developments in Magnetic Diagnostic Systems. *Chem. Rev.* **2015**, *115*, 10690–10724, doi:10.1021/cr500698d.
65. Colombo, S.; Lebedev, V.; Grujic, Z.D.; Dolgovskiy, V.; Weis, A. MPS and ACS with an Atomic Magnetometer. *International Journal on Magnetic Particle Imaging* **2016**, *2*.
66. Qu, H.; Caruntu, D.; Liu, H.; O'Connor, C.J. Water-Dispersible Iron Oxide Magnetic Nanoparticles with Versatile Surface Functionalities. *Langmuir* **2011**, *27*, 2271–2278, doi:10.1021/la104471r.
67. Mazur, M.; Barras, A.; Kuncser, V.; Galatanu, A.; Zaitzev, V.; Turcheniuk, K.V.; Woisel, P.; Lyskawa, J.; Laure, W.; Siriwardena, A.; et al. Iron Oxide Magnetic Nanoparticles with Versatile Surface Functions Based on Dopamine Anchors. *Nanoscale* **2013**, *5*, 2692–2702, doi:10.1039/C3NR33506B.
68. Bergemann, C.; Müller-Schulte, D.; Oster, J.; à Brassard, L.; Lübbe, A.S. Magnetic Ion-Exchange Nano- and Microparticles for Medical, Biochemical and Molecular Biological Applications. *Journal of Magnetism and Magnetic Materials* **1999**, *194*, 45–52, doi:10.1016/S0304-8853(98)00554-X.
69. Park, J.; An, K.; Hwang, Y.; Park, J.-G.; Noh, H.-J.; Kim, J.-Y.; Park, J.-H.; Hwang, N.-M.; Hyeon, T. Ultra-Large-Scale Syntheses of Monodisperse Nanocrystals. *Nature Mater* **2004**, *3*, 891–895, doi:10.1038/nmat1251.
70. Hyeon, T.; Lee, S.S.; Park, J.; Chung, Y.; Na, H.B. Synthesis of Highly Crystalline and Monodisperse Maghemite Nanocrystallites without a Size-Selection Process. *J. Am. Chem. Soc.* **2001**, *123*, 12798–12801, doi:10.1021/ja016812s.
71. Sun, S.; Zeng, H. Size-Controlled Synthesis of Magnetite Nanoparticles. *J. Am. Chem. Soc.* **2002**, *124*, 8204–8205, doi:10.1021/ja026501x.
72. Yang, G.; Park, S.-J. Conventional and Microwave Hydrothermal Synthesis and Application of Functional Materials: A Review. *Materials (Basel)* **2019**, *12*, 1177, doi:10.3390/ma12071177.
73. Wang, X.; Zhuang, J.; Peng, Q.; Li, Y. A General Strategy for Nanocrystal Synthesis. *Nature* **2005**, *437*, 121–124, doi:10.1038/nature03968.
74. Tzitzios, V.K.; Petridis, D.; Zafiropoulou, I.; Hadjipanayis, G.; Niarchos, D. Synthesis and Characterization of L10 FePt Nanoparticles from Pt–Fe3O4 Core-Shell Nanoparticles. *Journal of Magnetism and Magnetic Materials* **2005**, *294*, e95–e98, doi:10.1016/j.jmmm.2005.03.061.

75. Chow, G.M.; Kurihara, L.K.; Kemner, K.M.; Schoen, P.E.; Elam, W.T.; Ervin, A.; Keller, S.; Zhang, Y.D.; Budnick, J.; Ambrose, T. Structural, Morphological, and Magnetic Study of Nanocrystalline Cobalt-Copper Powders Synthesized by the Polyol Process. *Journal of Materials Research* **1995**, *10*, 1546–1554, doi:10.1557/JMR.1995.1546.
76. Cai, W.; Wan, J. Facile Synthesis of Superparamagnetic Magnetite Nanoparticles in Liquid Polyols. *Journal of Colloid and Interface Science* **2007**, *305*, 366–370, doi:10.1016/j.jcis.2006.10.023.
77. Joseyphus, R.J.; Kodama, D.; Matsumoto, T.; Sato, Y.; Jeyadevan, B.; Tohji, K. Role of Polyol in the Synthesis of Fe Particles. *Journal of Magnetism and Magnetic Materials* **2007**, *310*, 2393–2395, doi:10.1016/j.jmmm.2006.10.1132.
78. Dadfar, S.M.; Camozzi, D.; Darguzyte, M.; Roemhild, K.; Varvarà, P.; Metselaar, J.; Banala, S.; Straub, M.; Güvener, N.; Engelmann, U.; et al. Size-Isolation of Superparamagnetic Iron Oxide Nanoparticles Improves MRI, MPI and Hyperthermia Performance. *J Nanobiotechnol* **2020**, *18*, 22, doi:10.1186/s12951-020-0580-1.
79. Olesik, J.W. Elemental Analysis Using ICP-OES and ICP/MS. *Anal. Chem.* **1991**, *63*, 12A-21A, doi:10.1021/ac00001a711.
80. Galinetto, P.; Albini, B.; Bini, M.; Mozzati, M. Raman Spectroscopy in Zinc Ferrites Nanoparticles. In; 2018 ISBN 978-1-78923-000-0.
81. Yang, K.; Peng, H.; Wen, Y.; Li, N. Re-Examination of Characteristic FTIR Spectrum of Secondary Layer in Bilayer Oleic Acid-Coated Fe3O4 Nanoparticles. *Applied Surface Science* **2010**, *256*, 3093–3097, doi:10.1016/j.apsusc.2009.11.079.
82. Cursaru, L.M.; Piticescu, R.M.; Dragut, D.V.; Morel, R.; Thébault, C.; Carrière, M.; Joisten, H.; Dieny, B. One-Step Soft Chemical Synthesis of Magnetite Nanoparticles under Inert Gas Atmosphere. Magnetic Properties and In Vitro Study. *Nanomaterials* **2020**, *10*, 1500, doi:10.3390/nano10081500.
83. Li, L.; Li, D.; Zhang, Z. Colloidal Stability of Magnetite Nanoparticles Coated by Oleic Acid and 3-(N,N-Dimethylmyristylammonio)Propanesulfonate in Solvents. *Frontiers in Materials* **2022**, *9*.
84. Baumgartner, J.; Dey, A.; Bomans, P.H.H.; Le Coadou, C.; Fratzl, P.; Sommerdijk, N.A.J.M.; Faivre, D. Nucleation and Growth of Magnetite from Solution. *Nature Mater* **2013**, *12*, 310–314, doi:10.1038/nmat3558.
85. Hurt, D.; Li, S.; Amann, A. Versatile SQUID Susceptometer With Multiple Measurement Modes. *IEEE Transactions on Magnetics* **2013**, *49*, 3541–3544, doi:10.1109/TMAG.2013.2241029.
86. Martín, M.; Salazar, P.; Jiménez de Espinoza, C.; Lecuona, M.; Ramos, M.; Ode, J.; Alcoba, J.; Roche, R.; Villalonga, R.; Campuzano, S.; et al. Rapid Legionella Pneumophila Determination Based on a Disposable Core–Shell Fe3O4@poly(Dopamine) Magnetic Nanoparticles Immunoplatform. *Analytica Chimica Acta* **2015**, *in press*, in press.
87. Lim, J.; Yeap, S.P.; Che, H.X.; Low, S.C. Characterization of Magnetic Nanoparticle by Dynamic Light Scattering. *Nanoscale Res Lett* **2013**, *8*, 381, doi:10.1186/1556-276X-8-381.
88. Jefremovas, E.M.; Gandarias, L.; Rodrigo, I.; Marcano, L.; Grüttner, C.; García, J.Á.; Garayo, E.; Orue, I.; García-Prieto, A.; Muela, A.; et al. Nanoflowers Versus Magnetosomes: Comparison Between Two Promising Candidates for Magnetic Hyperthermia Therapy. *IEEE Access* **2021**, *9*, 99552–99561, doi:10.1109/ACCESS.2021.3096740.

89. Foner, S. Versatile and Sensitive Vibrating-Sample Magnetometer. *Review of Scientific Instruments* **1959**, *30*, 548–557, doi:10.1063/1.1716679.
90. Lopez-Dominguez, V.; Quesada, A.; Guzmán-Mínguez, J.C.; Moreno, L.; Lere, M.; Spottorno, J.; Giacomone, F.; Fernández, J.F.; Hernando, A.; García, M.A. A Simple Vibrating Sample Magnetometer for Macroscopic Samples. *Review of Scientific Instruments* **2018**, *89*, 034707, doi:10.1063/1.5017708.
91. Thanh, N.T. *Magnetic Nanoparticles From Fabrication to Clinical Applications*; Boca Raton: CRC press, 2012; ISBN 978-1-4398-6932-1.
92. Kemp, S.J.; Ferguson, R.M.; Khandhar, A.P.; Krishnan, K.M. Monodisperse Magnetite Nanoparticles with Nearly Ideal Saturation Magnetization. *RSC Adv.* **2016**, *6*, 77452–77464, doi:10.1039/C6RA12072E.
93. Bacri, J.-C.; Boué, F.; Cabuil, V.; Perzynski, R. Ionic Ferrofluids: Intraparticle and Interparticle Correlations from Small-Angle Neutron Scattering. *Colloids and Surfaces A: Physicochemical and Engineering Aspects* **1993**, *80*, 11–18, doi:10.1016/0927-7757(93)80219-5.
94. Upadhyay, R.V.; Mehta, R.V. Magnetic Properties of Ultra-Fine Particles of Mno.5Feo.5Fe204 Spinel System. *J. Phys.* **1993**, *41*, 14.
95. Chantrell, R.; Popplewell, J.; Charles, S. Measurements of Particle Size Distribution Parameters in Ferrofluids. *IEEE Transactions on Magnetics* **1978**, *14*, 975–977, doi:10.1109/TMAG.1978.1059918.
96. Sasayama, T.; Yoshida, T.; Saari, M.M.; Enpuku, K. Comparison of Volume Distribution of Magnetic Nanoparticles Obtained from M-H Curve with a Mixture of Log-Normal Distributions. *Journal of Applied Physics* **2015**, *117*, 17D155, doi:10.1063/1.4919268.
97. Biederer, S.; Knopp, T.; Sattel, T.F.; Lüdtke-Buzug, K.; Gleich, B.; Weizenecker, J.; Borgert, J.; Buzug, T.M. Magnetization Response Spectroscopy of Superparamagnetic Nanoparticles for Magnetic Particle Imaging. *J. Phys. D: Appl. Phys.* **2009**, *42*, 205007, doi:10.1088/0022-3727/42/20/205007.
98. Ludwig, F.; Wawrzik, T.; Yoshida, T.; Gehrke, N.; Briel, A.; Eberbeck, D.; Schilling, M. Optimization of Magnetic Nanoparticles for Magnetic Particle Imaging. *IEEE Transactions on Magnetics* **2012**, *48*, 3780–3783, doi:10.1109/TMAG.2012.2197601.
99. Ludwig, F.; Wawrzik, T.; Schilling, M. Characterization of Magnetic Nanoparticles for Magnetic Particle Imaging by Magnetorelaxometry, AC Susceptibility, Magnetic Particle Spectroscopy and Static Magnetization Measurements. In Proceedings of the Magnetic Particle Imaging; Buzug, T.M., Borgert, J., Eds.; Springer: Berlin, Heidelberg, 2012; pp. 35–40.
100. Yoshida, T.; Enpuku, K.; Ludwig, F.; Dieckhoff, J.; Wawrzik, T.; Lak, A.; Schilling, M. Characterization of Resovist® Nanoparticles for Magnetic Particle Imaging. In Proceedings of the Magnetic Particle Imaging; Buzug, T.M., Borgert, J., Eds.; Springer: Berlin, Heidelberg, 2012; pp. 3–7.
101. Ludwig, F.; Eberbeck, D.; Löwa, N.; Steinhoff, U.; Wawrzik, T.; Schilling, M.; Trahms, L. Characterization of Magnetic Nanoparticle Systems with Respect to Their Magnetic Particle Imaging Performance. *Biomedizinische Technik/Biomedical Engineering* **2013**, *58*, 535–545, doi:10.1515/bmt-2013-0013.
102. Ludwig, F.; Kuhlmann, C.; Wawrzik, T.; Dieckhoff, J.; Lak, A.; Kandhar, A.P.; Ferguson, R.M.; Kemp, S.J.; Krishnan, K.M. Dynamic Magnetic Properties of Optimized Magnetic Nanoparticles for Magnetic Particle Imaging. *IEEE Transactions on Magnetics* **2014**, *50*, 1–4, doi:10.1109/TMAG.2014.2329504.

103. Ludwig, F.; Remmer, H.; Kuhlmann, C.; Wawrzik, T.; Arami, H.; Ferguson, R.M.; Krishnan, K.M. Self-Consistent Magnetic Properties of Magnetite Tracers Optimized for Magnetic Particle Imaging Measured by Ac Susceptometry, Magnetorelaxometry and Magnetic Particle Spectroscopy. *Journal of Magnetism and Magnetic Materials* **2014**, *360*, 169–173, doi:10.1016/j.jmmm.2014.02.020.
104. Gehrke, N.; Heinke, D.; Eberbeck, D.; Ludwig, F.; Wawrzik, T.; Kuhlmann, C.; Briel, A. Magnetic Characterization of Clustered Core Magnetic Nanoparticles for MPI. *IEEE Transactions on Magnetics* **2015**, *51*, 1–4, doi:10.1109/TMAG.2014.2358275.
105. Pourshahidi, A.M.; Engelmann, U.M.; Offenhäusser, A.; Krause, H.J. Resolving Ambiguities in Core Size Determination of Magnetic Nanoparticles from Magnetic Frequency Mixing Data. *Journal of Magnetism and Magnetic Materials* **2022**, doi:https://doi.org/10.1016/j.jmmm.2022.169969.
106. Pourshahidi, A.M.; Achtsnicht, S.; Nambipareechee, M.M.; Offenhäusser, A.; Krause, H.-J. Multiplex Detection of Magnetic Beads Using Offset Field Dependent Frequency Mixing Magnetic Detection. *Sensors* **2021**, *21*, 5859, doi:10.3390/s21175859.
107. Achtsnicht, S.; Fitter, J.; Offenhäusser, A. Multiplex-Magnetdetektion von Superparamagnetischen Beads Zur Identifizierung von Trinkwasserkontaminationen, Dissertation, RWTH Aachen University, 2020, 2020.
108. Analog devices AD 9834 Data Sheet.
109. Cordewener, A. Android App Development for Bluetooth Remote Control of a Magnetic Reader, FH-Aachen.
110. IEEE Recommended Practices and Requirements for Harmonic Control in Electrical Power Systems. *IEEE Std 519-1992* **1993**, 1–112, doi:10.1109/IEEESTD.1993.114370.
111. Draack, S.; Viereck, T.; Kuhlmann, C.; Schilling, M.; Ludwig, F. Temperature-Dependent MPS Measurements. *International Journal on Magnetic Particle Imaging* **2017**, *3*.
112. Pourshahidi, A.M.; Achtsnicht, S.; Offenhäusser, A.; Krause, H.-J. Frequency Mixing Magnetic Detection Setup Employing Permanent Ring Magnets as a Static Offset Field Source. *Sensors* **2022**, *22*, 8776, doi:10.3390/s22228776.
113. Rezvani Jalal, N.; Mehrbod, P.; Shojaei, S.; Labouta, H.I.; Mokarram, P.; Afkhami, A.; Madrakian, T.; Los, M.J.; Schaafsma, D.; Giersig, M.; et al. Magnetic Nanomaterials in Microfluidic Sensors for Virus Detection: A Review. *ACS Appl. Nano Mater.* **2021**, *4*, 4307–4328, doi:10.1021/acsanm.1c01077.
114. Ling, Y.; Vassiliou, C.C.; Cima, M.J. Magnetic Relaxation-Based Platform for Multiplexed Assays. *Analyst* **2010**, *135*, 2360–2364, doi:10.1039/B926041M.
115. Rauwerdink, A.M.; Giustini, A.J.; Weaver, J.B. Simultaneous Quantification of Multiple Magnetic Nanoparticles. *Nanotechnology* **2010**, *21*, 455101, doi:10.1088/0957-4484/21/45/455101.
116. Rauwerdink, A.M.; Weaver, J.B. Harmonic Phase Angle as a Concentration-Independent Measure of Nanoparticle Dynamics: Harmonic Phase Angle as Measure of Nanoparticle Dynamics. *Med. Phys.* **2010**, *37*, 2587–2592, doi:10.1118/1.3426294.
117. Rauwerdink, A.M.; Weaver, J.B. Concurrent Quantification of Multiple Nanoparticle Bound States. *Medical Physics* **2011**, *38*, 1136–1140, doi:https://doi.org/10.1118/1.3549762.

118. Wu, K.; Wang, Y.; Feng, Y.; Yu, L.; Wang, J.-P. Colorize Magnetic Nanoparticles Using a Search Coil Based Testing Method. *Journal of Magnetism and Magnetic Materials* **2015**, *380*, 251–254, doi:10.1016/j.jmmm.2014.10.034.
119. Tu, L.; Wu, K.; Klein, T.; Wang, J.-P. Magnetic Nanoparticles Colourization by a Mixing-Frequency Method. *J. Phys. D: Appl. Phys.* **2014**, *47*, 155001, doi:10.1088/0022-3727/47/15/155001.
120. Wu, K.; Su, D.; Saha, R.; Liu, J.; Chugh, V.K.; Wang, J.-P. Magnetic Particle Spectroscopy: A Short Review of Applications Using Magnetic Nanoparticles. *ACS Appl. Nano Mater.* **2020**, *3*, 4972–4989, doi:10.1021/acsanm.0c00890.
121. Lenglet, L. Multiparametric Magnetic Immunoassays Utilizing Non-Linear Signatures of Magnetic Labels. *Journal of Magnetism and Magnetic Materials* **2009**, *321*, 1639–1643, doi:10.1016/j.jmmm.2009.02.104.
122. Alphandéry, E.; Lijeour, L.; Lalatonne, Y.; Motte, L. Different Signatures between Chemically and Biologically Synthesized Nanoparticles in a Magnetic Sensor: A New Technology for Multiparametric Detection., doi:10.1016/j.snb.2010.04.009.
123. Wu, K.; Liu, J.; Saha, R.; Peng, C.; Su, D.; Wang, Y.A.; Wang, J.-P. Investigation of Commercial Iron Oxide Nanoparticles: Structural and Magnetic Property Characterization. *ACS Omega* **2021**, 10.
124. Viereck, T.; Kuhlmann, C.; Draack, S.; Schilling, M.; Ludwig, F. Dual-Frequency Magnetic Particle Imaging of the Brownian Particle Contribution. *Journal of Magnetism and Magnetic Materials* **2017**, *427*, 156–161, doi:10.1016/j.jmmm.2016.11.003.
125. Shasha, C.; Teeman, E.; Krishnan, K.M.; Szwargulski, P.; Knopp, T.; Möddel, M. Discriminating Nanoparticle Core Size Using Multi-Contrast MPI. *Phys. Med. Biol.* **2019**, *64*, 074001, doi:10.1088/1361-6560/ab0fc9.
126. Möddel, M.; Meins, C.; Dieckhoff, J.; Knopp, T. Viscosity Quantification Using Multi-Contrast Magnetic Particle Imaging. *New J. Phys.* **2018**, *20*, 083001, doi:10.1088/1367-2630/aad44b.
127. Engelmann, U.M.; Shalaby, A.; Shasha, C.; Krishnan, K.M.; Krause, H.-J. Comparative Modeling of Frequency Mixing Measurements of Magnetic Nanoparticles Using Micromagnetic Simulations and Langevin Theory. *Nanomaterials* **2021**, *11*, 1257, doi:10.3390/nano11051257.
128. Murty, K.G. *Linear Complementarity, Linear and Nonlinear Programming*; Heldermann, N, 1988; ISBN 978-3-88538-403-8.
129. Ludwig, F.; Balceris, C.; Jonasson, C.; Johansson, C. Analysis of AC Susceptibility Spectra for the Characterization of Magnetic Nanoparticles. *IEEE Transactions on Magnetics* **2017**, *53*, 1–4, doi:10.1109/TMAG.2017.2693420.
130. Patterson, A.L. The Scherrer Formula for X-Ray Particle Size Determination. *Phys. Rev.* **1939**, *56*, 978–982, doi:10.1103/PhysRev.56.978.
131. Riahi, K.; Rietberg, M.T. Effect of Changing Iron Content and Excitation Frequency on Magnetic Particle Imaging Signal: A Comparative Study of Synomag® Nanoparticles. **2021**, *15*, 4.
132. Kallumadil, M.; Tada, M.; Nakagawa, T.; Abe, M.; Southern, P.; Pankhurst, Q.A. Suitability of Commercial Colloids for Magnetic Hyperthermia. *Journal of Magnetism and Magnetic Materials* **2009**, *321*, 1509–1513, doi:10.1016/j.jmmm.2009.02.075.
133. Shasha, C.; Teeman, E.; Krishnan, K.M. Nanoparticle Core Size Optimization for Magnetic Particle Imaging. *Biomed. Phys. Eng. Express* **2019**, *5*, 055010, doi:10.1088/2057-1976/ab3972.

134. Yu, E.Y.; Bishop, M.; Zheng, B.; Ferguson, R.M.; Khandhar, A.P.; Kemp, S.J.; Krishnan, K.M.; Goodwill, P.W.; Conolly, S.M. Magnetic Particle Imaging: A Novel in Vivo Imaging Platform for Cancer Detection. *Nano Lett.* **2017**, *17*, 1648–1654, doi:10.1021/acs.nanolett.6b04865.
135. Engelmann, U.M.; Shasha, C.; Teeman, E.; Slabu, I.; Krishnan, K.M. Predicting Size-Dependent Heating Efficiency of Magnetic Nanoparticles from Experiment and Stochastic Néel-Brown Langevin Simulation. *Journal of Magnetism and Magnetic Materials* **2019**, *471*, 450–456, doi:10.1016/j.jmmm.2018.09.041.
136. Lima, E.; De Biasi, E.; Mansilla, M.V.; Saleta, M.E.; Granada, M.; Troiani, H.E.; Effenberger, F.B.; Rossi, L.M.; Rechenberg, H.R.; Zysler, R.D. Heat Generation in Agglomerated Ferrite Nanoparticles in an Alternating Magnetic Field. *J. Phys. D: Appl. Phys.* **2013**, *46*, 045002, doi:10.1088/0022-3727/46/4/045002.
137. Raikher, Y.L.; Shliomis, M.I. The Effective Field Method in the Orientational Kinetics of Magnetic Fluids and Liquid Crystals. In *Advances in Chemical Physics*; Coffey, W., Ed.; John Wiley & Sons, Inc.: Hoboken, NJ, USA, 2007; pp. 595–751 ISBN 978-0-470-14146-5.
138. Coffey, W.T.; Cregg, P.J.; Kalmykov, Y.U.P. On the Theory of Debye and Néel Relaxation of Single Domain Ferromagnetic Particles. In *Advances in Chemical Physics*; Prigogine, I., Rice, S.A., Eds.; John Wiley & Sons, Inc.: Hoboken, NJ, USA, 2007; pp. 263–464 ISBN 978-0-470-14141-0.

Appendices

Appendix 1: Verification of the excitation chain

Example of the excitation signals taken from the high-frequency excitation chain. In Figure A), the cyan line shows the signal at the output of the DDS chip, and the yellow signal is behind the amplification stage. Figure B shows the signals behind the power amplifier stage. There is 180° phase difference between the two signals behind the power amplifer stage.

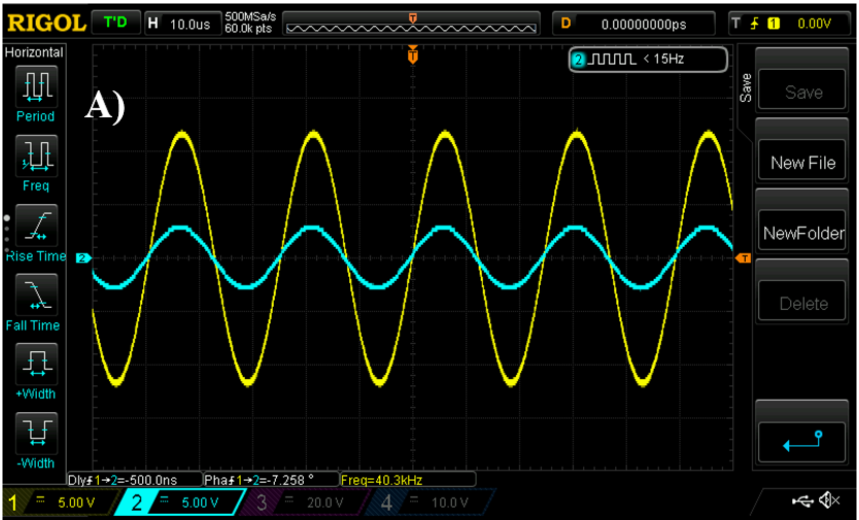

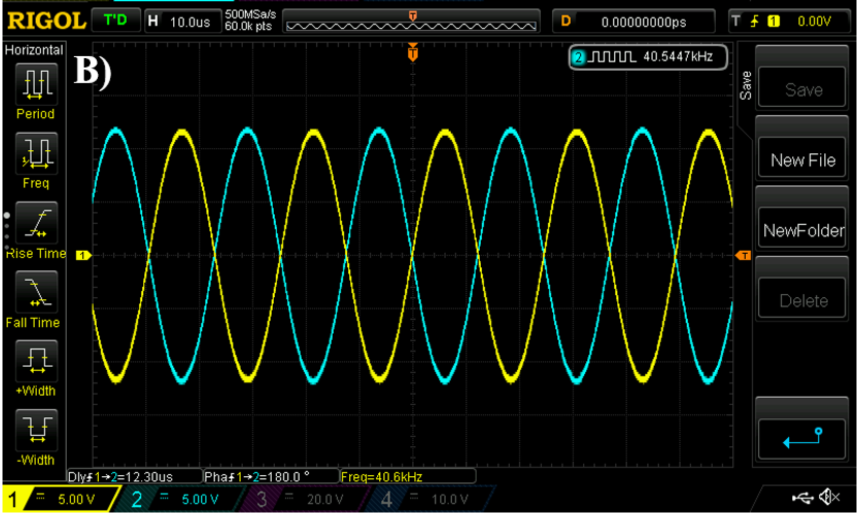

Appendix 2: Example of a deformed excitation field

Example of a deformed signal measured . If the DDS output signal is too large, the dynamic range of the amplifier is exceeded, yielding a clipped output voltage. Potentiometers behind the signal generation need to be trimmed until the signal is free of any clippings.

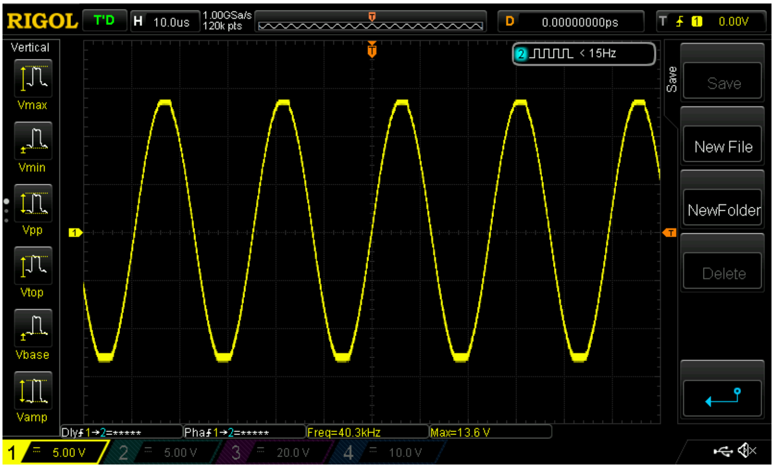

Appendix 3: Calibration of the high frequency excitation field

The magnetic field for the high-frequency excitation coil can be measured using an induction coil. Due to the limited bandwidth of the Hall probe Allegro A1324 which is used to measure the low frequency excitation field, it cannot be applied for measuring the excitation field at high frequencies > 10 kHz. A test coil should be used to measure the high frequency excitation field amplitude. According to Faraday's law, the voltage induced in the coil is proportional to the frequency. One should measure the low frequency field amplitude with both Hall probe and test coil, and measure the high frequency field amplitude with the test coil. Here, f_1 and f_2 are the high and low frequencies of the excitation fields, 40.5 kHz and 62.95 Hz, respectively. V_1 and V_2 are the measured induced voltages in the test coil at each of these frequencies. B_2 is the magnetic field of the low-frequency excitation coil, which is measured using the Hall sensor. The following relationship is used to convert the measured voltage in the induction coil to magnetic field unit [mT]:

$$B_1 = \frac{f_2 V_1}{f_1 V_2} \cdot B_2$$

Appendix 4: Connection of the ESP32 module to the magnetic reader

Esp32 Cam module connections on the magnetic reader PCB. Pins shown on the PCB plan (a) and diagram (b) will be connecting the ESP 32 to the magnetic reader.

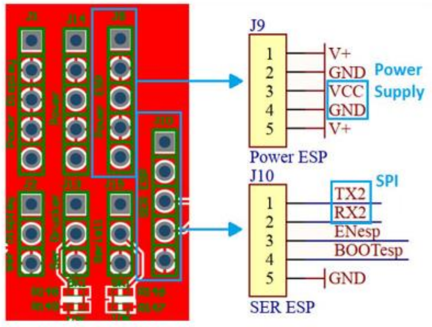

(a) (b)

Appendix 5: FMMD measurements of ternary mixtures

Offset-dependent FMMD signals of the ternary mixture samples made with different combinations of reference particle types Perimag 130 nm, NanomagD spio 20 nm and Nanomag CLD 1µm.

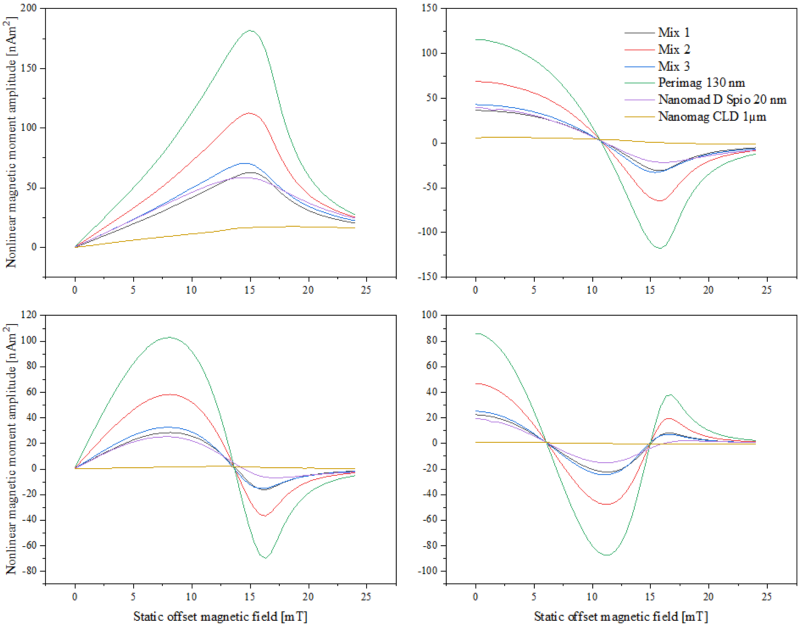

Appendix 6: FMMD double entry measurement head

a) Inside view of the double entry measurement head using two sets of excitation coils. b) 3D graphical representation of the stepper motor roller used for sample entry control in sequential measurement mode c) Excitation and detection coil configuration in double entry measurement head. d) Roller mounted on top of the measurement head.

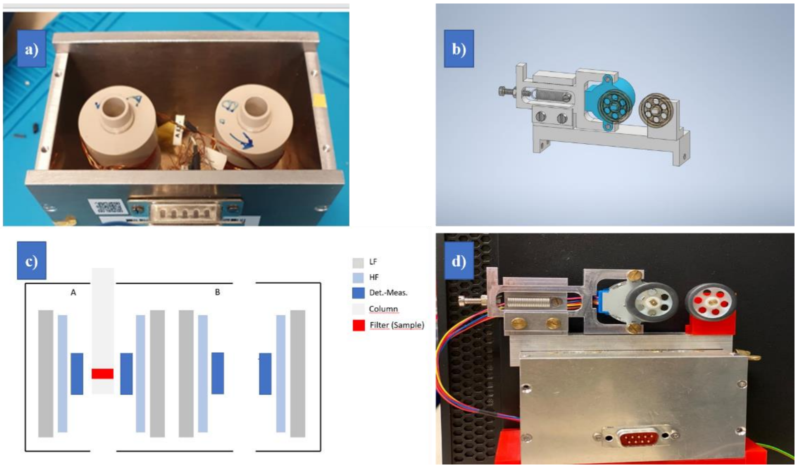

Appendix 7: FMMD measurements with double entry measurement head

Measurements of different samples using the double entry measurement head. The samples were initially measured with compartment A and then compartment B. The amplitude of the measurement signal $f_1+2{\cdot}f_2$ or HF+2·LF is presented in the figure. Different background colours indicate the measurements of different compartments.

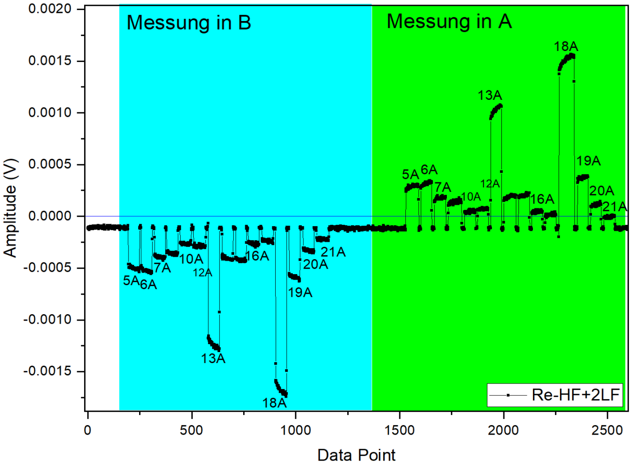

Appendix 8: Perpendicular static offset magnetic field setup

A FMMD setup with a static offset magnetic field source perpendicular to the excitation fields realized in a Helmholtz configuration. The figure a) shows the 3D construction design of the measurement head with perpendicular offset magnetic field module, with each part labelled accordingly. In b), the setups picture in frontal and side view are presented. In the frontal view, the aluminium lead has been opened to show the inside. The coil factor of the Helmholtz coil was experimentally determined as 3.66 mT/A. To monitor the temperature of the coil and record the room temperature several temperature sensors of type DS18B20 have been utilized.

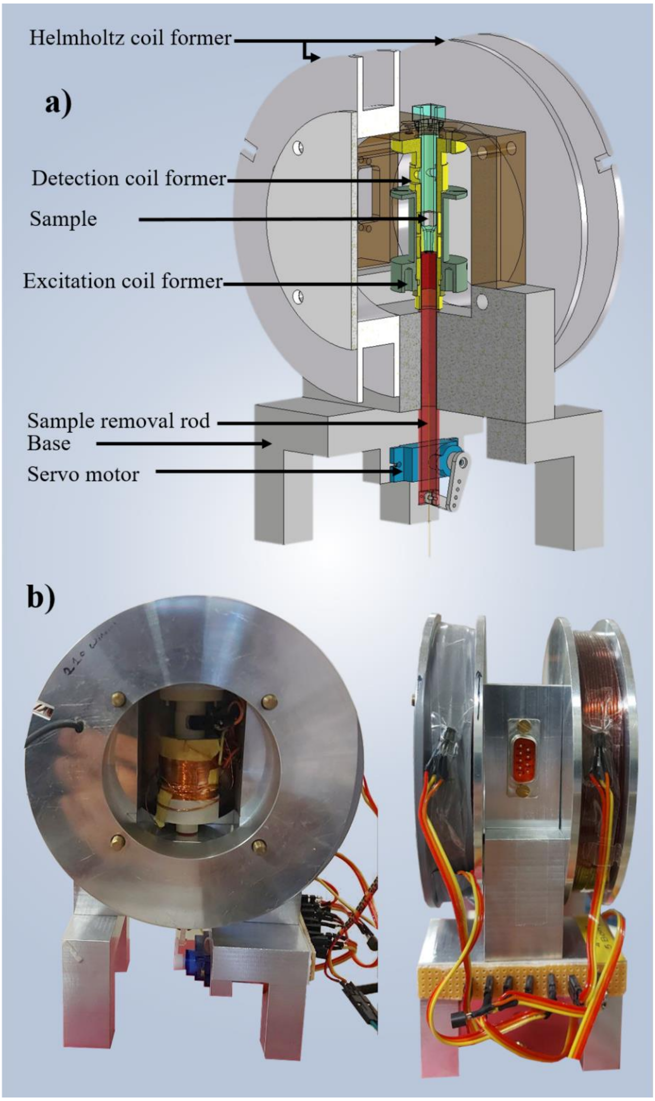

Appendix 9: Calibration of the Helmholtz coil for static offset field

The magnetic field profile of the Helmholtz coil on-axis and radial configuration was measured by supplying the coil with current $I = 0.089$ A. The Hall sensor Allegro was put coaxially into the center of the Helmholtz coil with the use of a translation stage. The current in the Helmholtz coil was measured by reading the voltage. Then the magnetic field on the axis of the Helmholtz coil was measured. The Hall sensor was moved in steps of 2 mm until the final position of 25 mm was reached. The results of the on-axis measurements are shown in figure a), they are compared with the calculated values. Figure b) shows the measured radial field profile.

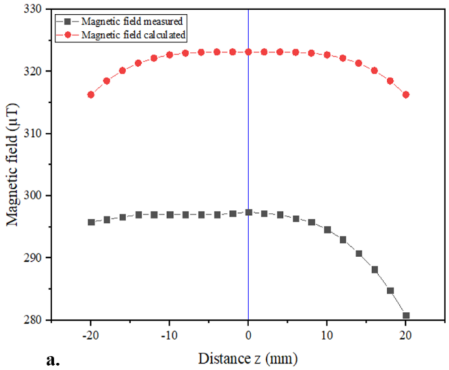

a.

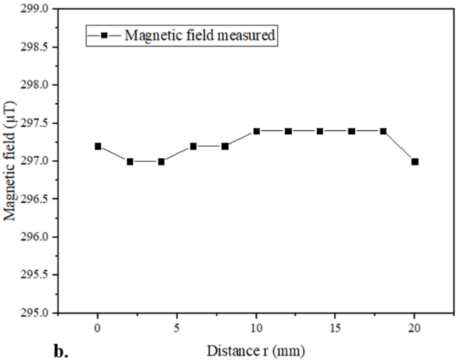

b.

List of Tables

List of Figures

List of Acronyms

Abbreviation	Definition
FMMD	Frequency Mixing Magnetic Detection
MIA	Magnetic Immunoassay
MNPs	Magnetic Nanoparticles
SP	Superparamagnetism
SPN	Superparamagnetic Nanoparticles
SPION	Superparamagnetic Iron oxide nanoparticles
MB	Magnetic beads
PEG	Polyethylene Glycol
EG	ethyl glycol
DEG	diethylene glycol
TREG	triethylene glycol
UV-vis	Ultraviolet–visible
ICP-OES	inductively coupled plasma atomic emission spectroscopy
ICP-MS	inductively coupled plasma mass spectroscopy
RS	Raman Spectroscopy
FT-IR	Fourier transform-infrared spectroscopy
TEM	Transmission electron microscopy
HRTEM	High resolution TEM
DLS	Dynamic light scattering
XRD	X-ray diffraction
VSM	Vibrating sample magnetometer
SQUID	Superconducting quantum interference devices
PDI	Polydispersity index
MPS	Magnetic particle spectroscopy
MPI	Magnetic particle imaging
FFT	Fast Fourier transform
EMOM	Electromagnetic offset module
PMOM	Permanent magnet offset module

MH	Measurement head
DDS	Direct digital synthesis
DAC	Digital to analogue converter
ADC	Analogue to digital converter
LF	Low frequency
HF	High frequency
MIA	Magnetic Immunoassay
POC	Point of care monitoring
GPS	Global Positioning System
QR	quick response
PCB	Printed circuit board
UART	universal asynchronous receiver-transmitter
RX	Recover
TX	Transmitter
DAQ	Data acquisition
TTL	Transistor-Transistor Logic
THD	Total harmonic distortion
SNR	Signal to noise ratio
LPF	Low pass filter
PVC	Polyvinyl chloride
PBS	Phosphate buffer solution
PE	Poly Ethylene
FWHM	Full with at half maximum
CCW	counter clock wise
GMR	Giant magnetoresistance
QP	Quadratic programming
MPMS	Magnetic Property Measurement System

List of publications and conference contributions

Publications

- **Pourshahidi, A.M.;** Offenhäusser, A.; Krause, H.-J. *Core size analysis of magnetic nanoparticles using frequency mixing magnetic detection with a permanent magnet as an offset source. Int J Mag Part Imag 2023, (Accepted manuscript*)
- **Pourshahidi, A.M**.; Achtsnicht, S.; Offenhäusser, A.; Krause, H.-J. *Frequency Mixing Magnetic Detection Setup Employing Permanent Ring Magnets as a Static Offset Field Source.* Sensors *2022, 22, 8776. https://doi.org/10.3390/s22228776*
- **Pourshahidi, A.M**.; Engelmann, U.M.; Offenhäusser, A.; Krause, H.-J. *Resolving ambiguities in core size determination of magnetic nanoparticles from magnetic frequency mixing data*. JMMM 2022 https://doi.org/10.1016/j.jmmm.2022.169969
- Engelmann, U.M.; **Pourshahidi, A.M**.; Shalaby, A.; Krause, H.-J. *Probing particle size dependency of frequency mixing magnetic detection with dynamic relaxation simulation*. JMMM https://doi.org/10.1016/j.jmmm.2022.169965
- **Pourshahidi, A.M**.; Achtsnicht, S.; Nambipareechee, M.M.; Offenhäusser, A.; Krause, H.-J. *Multiplex Detection of Magnetic Beads Using Offset Field Dependent Frequency Mixing Magnetic Detection*. *Sensors* 2021, *21*, 5859. https://doi.org/10.3390/s21175859
- Achtsnicht, S.; **Pourshahidi, A.M**.; Offenhäusser, A.; Krause, H.-J. *Multiplex Detection of Different Magnetic Beads Using Frequency Scanning in Magnetic Frequency Mixing Technique*. Sensors 2019, 19, 2599. https://doi.org/10.3390/s19112599

Conference contribution

- **Pourshahidi, A.M.;** Engelmann, U.M.; Offenhäusser, A.; Krause, H.-J. *Resolving ambiguities in core size determination of magnetic nanoparticles from magnetic frequency mixing data*. (Poster) at 13th International Conference on the Scientific and Clinical Applications of Magnetic Carriers.

Acknowledgements

I am very delighted to have the chance to express my gratitude, thank and acknowledge the people who supported and helped me during the completion of my thesis.

Prof. Dr. Andreas Offenhäusser, I would like to thank you for giving me the opportunity to be a part of your esteemed institute (*ICS-8/IBI-3*), and also for your support in reviewing my thesis and accepting to be my supervisor.

Prof. Dr. Hans-Joachim Krause, thank you for trusting me and accepting me as a member of your group (*Magnetic field sensors group – IBI-3*). your valuable guidance helped me all the time, your door was always open to me whenever I had a question. I have learned a lot from you both personally and professionally. Without your guidance and help none of this would have been achievable.

Special thanks to **Prof. Dr. Jörg Fitter** for reviewing my thesis and being my second referee.

Dr. Stefan Achtsnicht, thank you for supporting my work, and your valuable contribution to our joint publications and friendship.

Dr. Ulrich M. Engelmann, thank you for the fruitful discussions and contribution to our join publications. I have learned a lot from you.

Dieter Lomparski, first and foremost thank you for the design and construction of the mechanical components and your work in making the data acquisition software. Your help was vital to what has been achieved. Thank you for the memorable moments and funny discussions during the coffee breaks.

Norbert Wolters, thank you for the design and assembly of the readout electronics.

Abdalhalim Abuawad Shahin, we started our doctoral research journey together you are an amazing friend.

My peers **Max Jessing, Faranak Eivazi and Timur Bikoluv,** thank you for the fruitful discussion and for always willing to help. Moreover, thank you for making the workplace fun.

Phil Schmieder, **Jan Abresch** and the **MATSE** team for programming support.

Bachelor and Master students, **Andreas Cordewener, Taliya Karim, Emmanuelle Laure Homsi Bugueu, Yujie Huang, Maria Anugerah, Aya Midar** and **Othmane Ouaddou,** working with you has been a pleasure to me.

Former members of ICS-8 and current members of IBI-3: Thanks for creating such a professional, supportive and motivational working environment.

My Mother who always inspired me and provided me with love and support throughout my life.

Thank you All,

Ali Mohammad Pourshahidi

Schriften des Forschungszentrums Jülich
Reihe Information

Band / Volume 89
Controlling the electrical properties of oxide heterointerfaces through their interface chemistry
M.-A. Rose (2022), vi, 162 pp
ISBN: 978-3-95806-667-0

Band / Volume 90
Modeling and Suppressing Unwanted Parasitic Interactions in Superconducting Circuits
X. Xu (2022), 123, XVIII pp
ISBN: 978-3-95806-671

Band / Volume 91
Activating molecular magnetism by controlled on-surface coordinationI.
Cojocariu (2022), xi, 169 pp
ISBN: 978-3-95806-674-8

Band / Volume 92
Computational study of structural and optical properties of two-dimensional transition-metal dichalcogenides with implanted defects
S. H. Rost (2023), xviii, 198 pp
ISBN: 978-3-95806-682-3

Band / Volume 93
DC and RF characterization of bulk CMOS and FD-SOI devices at cryogenic temperatures with respect to quantum computing applications
A. Artanov (2023), xv, 80, xvii-liii pp
ISBN: 978-3-95806-687-8

Band / Volume 94
HAXPES study of interface and bulk chemistry of ferroelectric HfO_2 capacitors
T. Szyjka (2023), viii, 120 pp
ISBN: 978-3-95806-692-2

Band / Volume 95
A brain inspired sequence learning algorithm and foundations of a memristive hardware implementation
Y. Bouhadjar (2023), xii, 149 pp
ISBN: 978-3-95806-693-9

Band / Volume 96
Characterization and modeling of primate cortical anatomy and activity
A. Morales-Gregorio (2023), ca. 260 pp.
ISBN: 978-3-95806-698-4

Band / Volume 97
Hafnium oxide based memristive devices as functional elements of neuromorphic circuits
F. J. Cüppers (2023), vi, ii, 214 pp
ISBN: 978-3-95806-702-8

Band / Volume 98
Simulation and theory of large-scale cortical networks
A. van Meegen (2023), ca. 250 pp
ISBN: 978-3-95806-708-0

Band / Volume 99
Structure of two-dimensional multilayers and topological superconductors: surfactant mediated growth, intercalation, and doping
Y.-R. Lin (2023), x, 111 pp
ISBN: 978-3-95806-716-5

Band / Volume 100
Frequency mixing magnetic detection for characterization and multiplex detection of superparamagnetic nanoparticles
A. M. Pourshahidi (2023), X, 149 pp
ISBN: 978-3-95806-727-1

Weitere ***Schriften des Verlags im Forschungszentrum Jülich*** unter
http://wwwzb1.fz-juelich.de/verlagextern1/index.asp

Information
Band / Volume 100
ISBN 978-3-95806-727-1

Mitglied der Helmholtz-Gemeinschaft

JÜLICH
Forschungszentrum